

# **Topological mass of magnetic Skyrmions probed by ultrafast dynamic imaging**

**Dissertation**

zur Erlangung des Grades  
“Doktor  
der Naturwissenschaften”  
am Fachbereich 08 - Physik  
der Johannes Gutenberg-Universität  
in Mainz

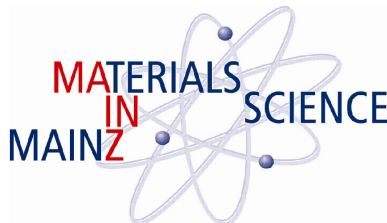
Felix Büttner  
geb. in Göttingen

Mainz, den 30. August 2013





This PhD was carried out in a joint project  
between the  
Johannes Gutenberg-Universität Mainz  
and the  
Technische Universität Berlin  
and within the  
MAINZ Graduate School of Excellence.







# Abstract

---

In this thesis, we investigate the GHz dynamics of skyrmionic spin structures by means of pump-probe dynamic imaging to determine the equation of motion that governs the behavior of these technologically relevant spin structures. To achieve this goal, we first designed and optimized a perpendicular magnetic anisotropy CoB/Pt multilayer material for low magnetic pinning, as required for ultrafast pump-probe imaging experiments. Second, we developed an integrated sample design for x-ray holography capable of tracking relative magnetic positional changes down to 3 nm spatial resolution. These advances enabled us to image the trajectory of a single magnetic Skyrmion. We find that the motion is comprised of two gyrotropic modes, one clockwise and one counterclockwise. The existence of two modes shows that Skyrmions are massive quasiparticles. From their derived frequencies we find an inertial mass for the Skyrmion which is a factor of five larger than expected based on existing models for inertia in magnetism. Our results demonstrate that the mass of Skyrmions is based on a novel mechanism emerging from their confined nature, which is a direct consequence of their topology.

# Zusammenfassung

---

In dieser Arbeit untersuchen wir mittels zeitaufgelöster Abbildungen die Gigahertz-Dynamik von magnetischen Skyrmionen, um die Bewegungsgleichungen für diese Quasiteilchen zu bestimmen. Um dieses Ziel zu erreichen haben wir zunächst ein CoB/Pt Schichtsystem entwickelt, das starke senkrechte magnetische Anisotropie mit einer besonders geringen Rauigkeit der Energielandschaft verbindet. Diese Eigenschaften sind für das repetitive dynamische Abbildungsverfahren unerlässlich. In einem zweiten Schritt haben wir das Probandesign optimiert und so weiterentwickelt, dass eine Beobachtung der Skyrmionenbewegung mit einer Auflösung von besser als 3 nm möglich wurde. Aufgrund dieser Verbesserungen ist es uns gelungen, die Trajektorie eines Skyrmionen aufzuzeichnen. Diese Bewegung ist eine Superposition von zwei Drehbewegungen, einer im Uhrzeigersinn und einer gegenläufigen. Aus der Existenz dieser zwei Moden lässt sich schließen, dass Skyrmionen träge Quasiteilchen sind, und aus den Frequenzen können wir einen Wert für die träge Masse ableiten. Es stellt sich heraus, dass die Masse von Skyrmion fünfmal größer ist als von existierenden Theorien vorhergesagt. Die Masse wird folglich durch einen neuartigen Mechanismus bestimmt, der sich aus der räumlichen Beschränkung der Skyrmionen ergibt, welche sich direkt aus der Topologie ableiten lässt.

# Contents

---

<b>Abstract</b>	<b>v</b>
<b>Zusammenfassung</b>	<b>vi</b>
<b>Preface</b>	<b>ix</b>
<b>1. Introduction</b>	<b>1</b>
1.1. Topology in physics . . . . .	1
1.2. History of Skyrmions in magnetism . . . . .	6
1.3. Magnetic field-induced domain wall motion . . . . .	9
1.4. Detection of domain wall dynamics . . . . .	14
<b>2. Experimental details</b>	<b>19</b>
2.1. Introduction . . . . .	19
2.2. Methods . . . . .	20
2.3. Sample fabrication steps . . . . .	21
2.3.1. Substrates . . . . .	21
2.3.2. Step 1: Object aperture . . . . .	23
2.3.3. Step 2: Alignment . . . . .	24
2.3.4. Step 3: Specimen . . . . .	25
2.3.5. Step 4: Excitation . . . . .	26
2.3.6. Step 5: Reference holes . . . . .	27
2.4. Performance . . . . .	27
2.5. Pump-probe setup . . . . .	29
2.6. Scanning transmission x-ray microscopy . . . . .	32
2.7. Conclusions . . . . .	34
<b>3. Material development and characterization</b>	<b>35</b>
3.1. Introduction . . . . .	35
3.2. Sample growth and material characterization . . . . .	37
3.3. Static properties of Co/Pd and Co/Pt nanostructures . . . . .	41
3.4. Static properties of CoB/Pt nanostructures . . . . .	46
3.5. Dynamic imaging in a CoB/Pt disk . . . . .	49
3.6. Conclusions . . . . .	50

---

<b>4. Topological mass of Skyrmions</b>	<b>51</b>
4.1. Introduction . . . . .	51
4.2. Experimental results . . . . .	53
4.3. Data analysis . . . . .	57
4.4. Discussion . . . . .	60
4.5. Conclusions . . . . .	61
<b>5. Open questions</b>	<b>63</b>
5.1. Field-induced domain wall motion in a multi-domain configuration	63
5.2. Composite Skyrmions: Inertia of vortex pairs and VA pairs . . . .	64
5.3. Quantitative model for the inertia of Skyrmions . . . . .	65
5.4. Current-induced Skyrmion motion . . . . .	66
5.5. Further material optimization . . . . .	68
5.6. Conclusions . . . . .	68
<b>6. Conclusions and outlook</b>	<b>69</b>
<b>A. <math>K_{\perp}</math> and <math>m_D</math> in perpendicular magnetic multilayers</b>	<b>73</b>
A.1. Calculations . . . . .	80
<b>B. Solution of the bubble equation of motion</b>	<b>82</b>
<b>Bibliography</b>	<b>94</b>
<b>Acknowledgments</b>	<b>95</b>
<b>Curriculum Vitae</b>	<b>97</b>
<b>List of publications</b>	<b>99</b>

# Preface

---

In this thesis, we investigate the dynamics of nanoscale cylindrical magnetic domains in a thin-film ferromagnet with preferred out-of-plane alignment of the magnetic moments. These cylindrical domains, traditionally called bubbles for their round shape, form the smallest domains in a two-dimensional ferromagnet. Bubbles are topologically non-trivial configurations; they belong to the topological class of Skyrmions. Historically, ferromagnetic domains are the most important medium for digital data storage, and magnetic bubbles played a major role in the research on the statics and dynamics of ferromagnetic domains and in the development of novel devices. On the applications side, bubbles were most successfully used in solid state storage devices, in which the information (the bubbles) is shifted within the material instead of the read or write head moving to the position of the information bit. Nowadays, we are still using rotating magnetic hard disks, and the search for novel concepts for magnetic solid state devices is more vivid than ever. One concept facing particular interest in this context is the racetrack memory, a magnetic wire in which domains are displaced by spin currents.

One major challenge in the realization of such a racetrack memory device is the large current density that is required to move straight domain walls. Recently, it was found that chiral Skyrmions (bubbles with an additional exchange-like interaction stabilizing their chirality) can be moved with current densities that are roughly one million times smaller than that for ordinary straight walls. To promote their application in actual devices, it would be important to investigate which parts of the extensive existing knowledge about bubbles holds for chiral Skyrmions, too.

Another important aspect for the realization of devices based on magnetic Skyrmions is that, so far, neither bubbles nor chiral Skyrmions have been investigated experimentally on the GHz time scale. Because present day devices operate at these high frequencies, studies on the high frequency behavior of magnetic Skyrmions are critical for further developments. In this work, we image the excitation and relaxation path of a bubble in a parabolic potential, and we find that the motion is determined by two eigenfrequencies in the GHz regime. We observe that the trajectory is a simultaneous superposition of both modes, pointing to the unexpected presence of inertia in such spin structures. In particular, we find that this inertial mass is larger than in any other magnetic system investigated

so far. We develop a theoretical argument to explain the presence of such a large effective mass, which is derived from the Skyrmion topology, and thus applicable to all skyrmionic spin structures. We envision that our theoretical description will stimulate the development of more detailed models for magnetic Skyrmions, and that our experimental approach can be utilized to further investigate the high frequency dynamics of Skyrmions in various situations.

This thesis is structured as follows. We start in chapter 1 with a review of the concept of topology (in particular of Skyrmions in magnetism), followed by an overview on the history of skyrmionic spin structures, a theoretical description of existing theories of inertia in magnetism, and an argument for using x-ray holography to investigate the dynamics of Skyrmions.

X-ray holography is a recent imaging technique. The present work represents the first successful dynamic imaging using x-ray holography. The development of both the sample design and a fabrication scheme as well as a working setup for pump-probe holographic imaging was a key part of this work. Chapter 2 summarizes the results of this development and provides the technical background for the experiments presented later in chapter 4.

The dynamics of topological magnetization configurations is qualitatively insensitive to material parameters. However, for experimental observation of the topology-driven dynamics, the material has to be tailored with respect to a number of essential properties. In particular, thermal-induced and hence stochastic events have to be suppressed to allow for trillion-fold repetition of the pump-probe experiment. The development of the material is outlined in chapter 3, accompanied by a detailed characterization of the optimized material system.

The most significant results of this work are presented in chapter 4. We show experimentally and by using simulations that a skyrmionic spin structure can be described by a deformable quasiparticle that follows a linear second order differential equation of motion. The second order coefficient can be interpreted as an inertial mass of the Skyrmion. We argue that the existence of this mass fundamentally originates from the topology of the system, and we so we call it a topological mass.

The results obtained in this thesis mark the start for the investigation of the high frequency dynamics of topological spin configurations. While we have found the fundamental equation of motion of magnetic Skyrmions, a large variety of open questions arise from our findings. A selection of immediate open questions and suggestions for follow-up experiments are provided in chapter 5. Chapter 6 then gives a summary of the main conclusions of this work and a more general outlook for the development of the research field.

This thesis is a cumulative dissertation. Parts of the text and some figures have been published in, or submitted to, journals with peer-reviewing. Such paragraphs and figures are marked at the end of the paragraph or the figure caption with

unique identifiers as follows:

- \* Felix Büttner, C. Moutafis, M. Schneider, B. Krüger, C. M. Günter, J. Geilhufe, C. v. Korff Schmising, J. Mohanty, B. Pfau, S. Schaffert, M. Foerster, T. Schulz, C. A. F. Vaz, J. Franken, H. J. M. Swagten, M. Kläui, and S. Eisebitt, *Topological mass of magnetic Skyrmions*, (version submitted to Science).
- † Felix Büttner, C. Moutafis, A. Bisig, P. Wohllhüter, C. M. Günther, J. Mohanty, J. Geilhufe, M. Schneider, C. v. Korff Schmising, S. Schaffert, B. Pfau, M. Hantschmann, M. Riemeier, M. Emmel, S. Finizio, G. Jakob, M. Weigand, J. Rhensius, J. H. Franken, R. Lavrijsen, H. J. M. Swagten, H. Stoll, S. Eisebitt, and M. Kläui, *Magnetic states in low pinning high anisotropy material nanostructures suitable for dynamic imaging*, Phys. Rev. B **87**, 134422 (2013)
- ‡ Felix Büttner, Michael Schneider, Christian M. Günther, C. A. F. Vaz, Bert Lägél, Dirk Berger, Sören Selve, Mathias Kläui, and Stefan Eisebitt, *Scriptable sample fabrication process for pump-probe x-ray holographic imaging*, (version submitted to Optics Express).

Small modifications, such as formatting, language improvements, and adaptations to the current context, may have been performed without further notice. The authors contributions to the publications are as follows:

All three publications have been written by F. Büttner, with comments and suggestions from all authors. The conventional Co/Pt and Co/Pd samples have been structured by J. Rhensius. The CoB/Pt samples have been prepared by F. Büttner, together with M. Schneider, C. M. Günther, C. A. F. Vaz, and B. Lägél. The imaging experiments were conceived and organized by F. Büttner and performed by F. Büttner, C. Moutafis, M. Schneider, B. Krüger, C. M. Günter, J. Geilhufe, C. v. Korff Schmising, J. Mohanty, M. Hantschmann, M. Riemeier, B. Pfau, S. Schaffert, M. Weigand, J. Rhensius, M. Foerster, T. Schulz, and S. Finizio. M. Emmel, S. Finizio, G. Jakob have measured the SQUID hysteresis loops. The data analysis and the supporting analytical calculations and micromagnetic simulations were carried out by F. Büttner and B. Krüger. F. Büttner discussed the results with C. Moutafis, B. Krüger, M. Kläui and S. Eisebitt. C. Barton and C. Morrison of the group of T. Thomson have grown the magnetic material Co/Pd<sub>50</sub>. The multilayers Co/Pt<sub>6</sub> and Co/Pd<sub>8</sub> have been sputtered by J. Rhensius and G. Heldt. The boron doped materials CoB/Pt<sub>30</sub> and CoB/Pt<sub>40</sub> have been deposited by R. Lavrijsen and J. H. Franken supervised by H. J. M. Swagten. M. Weigand and H. Stoll helped with the high frequency electronics.

# List of symbols

---

- $A$  exchange stiffness. 7, 10, 11, 39, 40, 81
- $B$  magnetic induction. 55, 58, 60, 64
- $D$  dissipation tensor, effectively a scalar throughout this thesis. 6, 15, 57, 85
- $E$  total energy. 9–11, 38
- $G$   $z$ -component of gyrocoupling vector. 6, 58, 59, 85
- $H_{\text{ext}}$  external magnetic field (amplitude). 48
- $K_{\perp}$  transverse anisotropy constant. 12, 13, 75, 76, 81
- $K_{\psi}$   $\psi$ -dependent effective anisotropy. 12
- $K_u$  uniaxial anisotropy, positive values favoring out-of-plane spin alignment. 7–11, 38, 39
- $K_{u,\text{eff}}$  effective uniaxial anisotropy, includes stray field energies. 7, 8, 11–13, 38, 39, 75, 81
- $K$  quasiparticle restoring force spring constant. 59, 60, 85
- $M_s$  saturation magnetization. 6–11, 13, 38, 39, 60, 75, 77, 79–81
- $M_z$  out-of-plane component of the local magnetization vector. 40, 48
- $M$  component of the magnetization. 75
- $M$  quasiparticle inertial mass. 51, 52, 57, 59, 85
- $N$  Skyrmion number. 2–7, 52–54, 56, 57, 59, 60, 64
- $Q$  quality factor  $Q = 2K_u/(\mu_0 M_s^2)$ . 8, 11, 12, 39, 60
- $R$  radius. 7
- $S$  surface. 10, 77, 80, 81
- $U$  magnetostatic potential. 6, 15, 57
- $V$  volume. 10, 77, 79



- 
- $W$  winding number. 3, 4
- $X$   $x$ -coordinate of a specific feature (e.g., quasiparticle center). 57–59
- $Y$   $y$ -coordinate of a specific feature (e.g., quasiparticle center). 57–59
- $\Delta_0$  domain wall width parameter of a Bloch wall ( $\psi = 0$ ). 7, 11, 13, 39, 40, 75, 76, 79–82
- $\Delta$  domain wall width parameter at variable  $\psi$ . 12, 13, 75, 77, 78, 80, 81
- $\Sigma\omega$  sum of the two eigen angular velocities of a magnetic Skyrmion. 59
- $\alpha$  Gilbert damping. 7, 9, 10, 13
- $\bar{A}$  complex amplitude of a wave / an oscillation. 57
- $\bar{R}$  position vector of a specific feature expressed as a complex number. 57–60, 85
- $\bar{\eta}$  complex damping parameter. 85
- $\bar{\omega}$  complex angular velocity  $\bar{\omega} = \omega + i/\tau$ . 85
- $\bar{r}$  2D position vector expressed as a complex number. 60
- $\chi$  standard deviation of the domain width distribution. 39, 40
- $\gamma$  electron gyromagnetic ratio. 6, 9, 10, 13
- $\hat{\sigma}$  Pauli matrix vector. 8
- $\hat{\mathbf{L}}$  angular momentum operator. 8
- $\hat{\mathbf{S}}$  spin operator. 8
- $\hat{\mathbf{p}}$  momentum operator. 8
- $\lambda$  photon wave length. 17
- $\langle R \rangle$  average radius. 59
- $\mathcal{L}$  length of a structure. 79
- $\mathcal{N}$  number of repeats. 75–81
- $\mathcal{P}$  multilayer periodicity (total thickness of a magnetic layer and a non-magnetic spacer). 75–82
- $\mathcal{T}$  thickness of a structure / a single magnetic layer in a multilayer. 6, 59, 75–77, 79–82
- $\mathcal{W}$  width of a structure. 77–79, 82, 83

- $\mu_0$  vacuum magnetic permeability. 7–11, 38, 75, 77–81
- $\omega$  angular velocity. 57–59, 85
- $\phi$  azimuthal angle. 3, 8–12
- $\psi$  spin angle perpendicular to the domain wall. x, 11–13, 75–78, 80, 81
- $\rho$  (magnetic) charge density. 10, 59, 77, 78, 80, 81
- $\sigma$  domain wall energy per unit area. 12, 13, 76–81
- $\tau$  damping time constant. 57, 58, 85
- $\theta$  polar angle. 3, 9–12, 52, 76
- $\varphi$  spin space azimuthal angle. 3, 52
- $\varsigma$  (magnetic) charge density. 79
- $\zeta$  domain wall width. 39, 40
- $d$  magnetic dipole moment. 59, 60
- $k$  photon wave number  $k = 2\pi/\lambda$ . 78, 79, 81, 82, 84
- $m_{\mathbf{D}}$  Döring domain wall mass density. 13, 75
- $n$  topological density. 2, 5
- $p$  polarity. 2–4
- $q$  photon wave vector transfer in an elastic scattering event  $q = \mathbf{k}_f - \mathbf{k}_i$ . 39
- $r$  radial coordinate. 8, 10, 79
- $t$  time. 12, 32, 36, 55–59, 85
- $w$  energy volume density. 9–12
- $x_0$  domain wall position in the 1D model (often called  $q$  in the literature). 11–13
- $x$  first real space coordinate, in films always in-plane. 2, 9, 11, 12, 54, 55, 58, 60, 64, 75–79, 81, 84
- $y$  second real space coordinate, in films always in-plane. 2, 9, 54, 55, 58, 60, 64, 75–79, 82, 83
- $z$  third real space coordinate, in films always perpendicular to the film plane. 9, 54, 55, 58, 60, 64, 75–79
- $\mathbf{G}$  gyrocoupling vector. 6, 15, 57, 85

**H** local magnetic field vector. 9, 10, 38

**M** local magnetization vector. 9, 10, 38, 75–77

**R** position vector of a specific feature (e.g., quasiparticle center). 6, 57, 58, 85

**m** unit vector along the local magnetization. 2

**r** real space coordinate vector. 9, 10, 12, 15, 76, 77, 81

# List of materials

---

Throughout this thesis, various material configurations are investigated. We will use the following abbreviations (thicknesses given in nm):

**Co/Pd<sub>50</sub>** Ta(3)/Pd(3)/[Co(0.3)/Pd(0.9)]<sub>50</sub>/Pd(1.1). ix, 37, 40–43

**Co/Pd<sub>8</sub>** Ta(1.5)/Pd(1.5)/[Co(0.3)/Pd(0.9)]<sub>8</sub>/Pd(0.9). ix, 37, 38, 41

**Co/Pt<sub>6</sub>** Pt(1.8)/[Co(0.6)/Pt(1.8)]<sub>6</sub>. ix, 37, 38, 41–45

**CoB/Pt<sub>30</sub>** Pt(2)/[Co<sub>68</sub>B<sub>32</sub>(0.4)/Pt(0.7)]<sub>30</sub>/Pt(1.3). ix, 27, 37–39, 41, 42, 53

**CoB/Pt<sub>40</sub>** Ta(2)/Pt(2)/[Co<sub>68</sub>B<sub>32</sub>(0.35)/Pt(0.7)]<sub>40</sub>/Pt(1.3). ix, 37, 38, 49

# Chapter 1

## Introduction

---

### 1.1. Topology in physics

The implications of the geometry of a system to its physical behavior have always been amongst the most fundamental principles of science and of physics in particular. The more general the characterization of a geometry associated with a particular physical law, the more relevant and applicable this law becomes. Most prominently, the symmetry of a system and its scaling behavior can imply consequences of large generality, as any law has to inherit these properties. The topology of a system is another property with equally fundamental importance. Because the topology does not change under continuous deformations, it is particularly useful for the description of deformable, confined structures. Topological structures can be found in a large variety of research areas, including electronic band structure topologies<sup>1</sup> (defined essentially by the energetic ordering of bands), real space topological configurations in condensed matter physics (such as topological configurations in magnetism,<sup>2–10</sup> Bose Einstein condensates,<sup>11,12</sup> and antiferromagnetic superconductors<sup>13</sup>), and winding quantum fields.<sup>14–16</sup> These topologies have dramatic implications, such as topologically quantized edge and surface conducting states (manifesting in the quantum Hall effect, the quantum spin Hall effect, and in topological insulators),<sup>1</sup> Berry phases and quantized emergent magnetic fields leading to a topological Hall effect in magnetic Skyrmion crystals,<sup>8,9</sup> and fermionic particle states forming in a bosonic quantum field theory.<sup>14,15</sup>

Topology is a mathematical concept to classify geometrical properties of continuous structures (where structures can be real space objects, vector fields, momentum space functions, etc.). Two structures are considered equivalent if there exists a continuous map from one to the other. There are many possible definitions of continuity inheriting from the large variety of possible complete sets of open subsets of the structure under consideration. Physical constraints, such as energy barriers or forbidden intermediate states, define allowed deformations and the set of prohibited or strongly suppressed transformations. They therefore specify meaningful topological distinctions. In physics, topologies are often classified according to homotopic transformations between spaces with Euclidian

metric and an Euclidian definition of neighborhood and open sets. A homotopy is a continuous deformation, not necessarily bijective. In contrast, homeomorphisms – defining another possible topological classification – are bijective. For instance, a line and a point are homotopically equivalent, but they are not homeomorph.

To deduce implications of the topology on the physics of a system, the choice of topological classification has to be based on physical arguments. In magnetism, the following arguments apply. First, in most magnetic systems, the magnetization profile varies on length scales much larger than crystal lattice constants due to the exchange mechanism. Hence, the associated vector field is well described in a continuum model, a prerequisite for a topological classification. Second, the exchange interaction, which scales with the gradient of the magnetization, sets an energy barrier for discontinuous deformations, justifying the concept of homotopy. And third, magneto-static interactions (anisotropy and stray fields) stabilize the boundary of the structure. Hence, homotopy transformations are allowed, provided that they do not modify the boundary of the structure. This set of allowed transformations (all others are strongly suppressed) defines topological equivalence classes.

One example of a topologically non-trivial structure in real space is the Skyrmion. Skyrmions, in general, refer to vector fields with a spherical topology, first identified by T. Skyrme in the field of nuclear physics.<sup>15</sup> By topological arguments, Skyrme could show the existence of confined fermionic particle-like solutions of a non-linear bosonic meson field theory. Specifically, he constructed a field operator that maps the three-dimensional (3D, or 3+1 to include the time dimension) domain space to the surface of a sphere.<sup>15</sup> Similarly, the macrospin in micro-magnetism is a vector in  $\mathbb{R}^3$  with constant modulus, or, equivalently, a point on the 2D surface of a sphere  $S^2$ . Of particular interest are skyrmionic spin structures in thin films (2+1 domain space), i.e., vector field  $\mathbb{R}^2 \rightarrow S^2$  that are homotopically equivalent to the identity map on a sphere  $\text{id}_{S^2}$ . In these structures, the domain space can be continuously deformed to a spherical shape such that the map to the spin space changes continuously, and that the boundary of the domain space always maps to the same spin. This homotopy between such so-called magnetic Skyrmion and the vector field of a sphere is visualized in Fig. 1.1.

The homotopy between a vector field and the identity map on a sphere is described by the topologically invariant Skyrmion number  $N$ . This counts the number of times the sphere is covered in the homotopical deformation. In two dimensions, the Skyrmion number  $N$  of a vector field  $\mathbb{R}^2 \ni (x, y) \rightarrow \mathbf{m} \in S^2$  can be calculated by  $N = (8\pi)^{-1} \int dx dy n$  with the topological density  $n = \epsilon_{\mu\nu} (\partial_\mu \mathbf{m} \times \partial_\nu \mathbf{m}) \cdot \mathbf{m}$ .<sup>17</sup> Note that the sign in this formula is not consistently defined in the literature, and the definition used here is adapted from Belavin and Polyakov (the first published application of this formula in the field of magnetism).<sup>17</sup> For our definition and axially symmetric structures with polarity  $p$  and

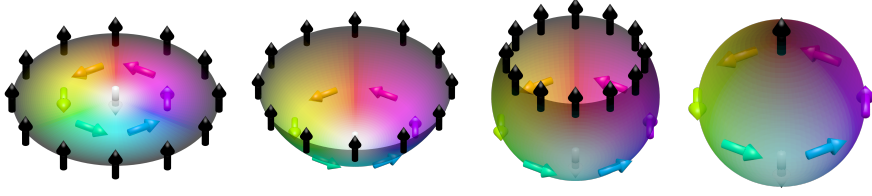


**Figure 1.1 | Homotopy between a Skyrmion in a disk and the identity map of the sphere.** The hue of the color represents the azimuthal angle of the spins, and the black / white level symbolizes the polar angle. The images show a continuous deformation of the Skyrmion (left) to a spherical shape (right). All spins of the Skyrmion boundary (black spins) are mapped to the north pole of the sphere, which is only possible because they all point in the same direction. The white spins of the inner domain are all mapped to the south pole.

winding number  $W$ , this formula can be simplified to  $N = 1/2pW$ .<sup>2</sup> The winding number itself is a topological invariant with wide applications in the field of magnetism. We will therefore give a short overview of this quantity.

The winding number  $W$  is a one-dimensional analog of the Skyrmion number, describing how often a closed, oriented path can be mapped homotopically to a circle. Historically, before the establishment of the Skyrmion topology in condensed matter physics, the product of winding number and polarity was often used to describe skyrmionic phenomena, in particular in magnetic bubble Skyrmions.<sup>18</sup> In thin film magnetism, the winding number is most conveniently calculated by expressing the 3D macrospin in spherical angles  $(\phi, \theta)$ . The winding number of a closed loop is given by the normalized difference of the azimuthal angle  $\phi_i$  of the spin at an arbitrary point of the loop and the angle  $\phi_f$  of the spin after going around the full loop once in positive orientation:  $W = (\phi_f - \phi_i)/(2\pi)$ . Naturally, the loop must not cross regions where  $\phi$  is not well defined (singularities), such as points or areas with pure out-of-plane magnetization or points where two spins are pointing head-to-head.

The winding number is a useful quantity to calculate the Skyrmion number “by hand” through the identity  $N = 1/2pW$ , because the winding number is strictly quantized and it is therefore easy to determine from a picture of the magnetization configuration. The winding number is always integer, and it has non-zero value only if the loop encloses a singularity.<sup>19</sup> An exception of this rule is given by singularities at the boundary of the domain space, where no closed loop around the singularity exists. In this special situation, a reasonable definition of the winding number is provided by mirroring the configuration on the tangent plane of the boundary, closing the loop in the mirrored image, and assigning half of the obtained winding number to the edge singularity. This procedure is well defined provided that (i) the spins at the boundary apart from the singularity are lying

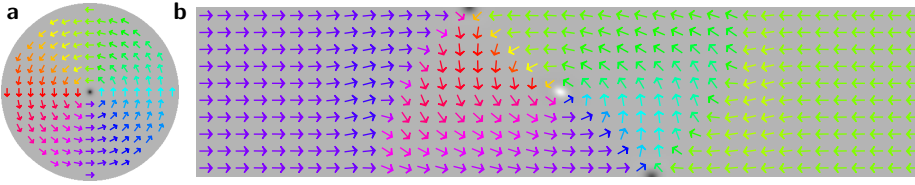


**Figure 1.2 | Vortex in a disk and vortex domain wall in a wire.** (a) Vortex state with winding number  $W = 1$ , polarity  $p = -1$ , and hence Skyrmion number  $N = -1/2$  in a disk. The gray scale visualizes the  $z$ -component of the magnetization, where gray indicates magnetization pointing in-plane and black indicates magnetization pointing down (away from the reader, negative  $z$ -direction). The arrows visualize the in-plane direction of the magnetization, and their hue symbolizes the azimuthal angle. (b) Vortex domain wall with a vortex in the center (white vortex core, pointing up) and two half antivortices at the edges (black half-antivortex core) in a wire. The vortex has a winding number of  $W = 1$ , a polarity of  $p = 1$ , and a Skyrmion number of  $N = 1/2$ . Each anti-vortex has a winding number of  $W = -1/2$ , a non-integer polarity of  $p \approx -0.8$ , and hence a Skyrmion number of  $N \approx 0.2$ . The total structure therefore has a winding number of  $W = 0$  and Skyrmion number of  $N \approx 0.9$ .

in the tangent plane, and that (ii) the boundary is flat across the singularity to ensure that the mirror plane is well defined. Under these assumptions, the winding number of edge singularities becomes half integer. However, winding topological edge defects always come in pairs, and the total winding number is integer.<sup>19</sup> In fact, as shown by Oleg Tchernyshyov and Gia-Wei Chern, any spin structure in 2D magnetic elements can be thought of as a composite of the basic bulk structures, vortex and antivortex, and their edge equivalents, half-vortex and half-antivortex.<sup>19</sup>

The winding number is an important topological invariant for the description of in-plane magnetized systems in small elements, such as domain walls in thin magnetic wires. As an example, we show two topologically distinct structures in Fig. 1.2, a vortex and a vortex domain wall. Both spin structures have the same Skyrmion number ( $N = 1/2$ ), but the vortex domain wall has, in addition to the vortex in the center, two half-antivortices at the edge of the wire. Hence, the total winding number of the vortex is  $W = 1$ , and the vortex domain wall has  $W = 0$ . The topological number reflects the fact that the vortex domain wall is locally confined to a small region within the wire, while the vortex extends over the whole element. As we will argue later in this thesis, the confinement of a spin structure leads to inertia. Indeed, inertia has been observed in vortex domain walls,<sup>20–22</sup> but not in vortices.

In contrast to the winding number, the Skyrmion number describes the full 3D topology of the spins. Hence, the Skyrmion number becomes particularly useful for systems with in-plane and out-of-plane components of the magnetization. The Skyrmion number provides direct information about the domain structure. The only way to map a planar geometry continuously to a sphere is by contracting its boundary to one single point in the sphere (defining one of the poles). Therefore, all



spins on the boundary of an  $N = 1$  configuration must have the same orientation, forming a domain. Somewhere in the interior of the configuration, a connected area exists in which the spins point anti-parallel to the outer domain (this inner domain can be as small as one point). The transition between these two domains is a smooth domain wall winding around the inner domain to ensure that the whole sphere is represented. That is, the pure fact that a spin vector field has  $N = 1$  implies the existence of the inner domain, the outer domain, and the domain wall, of which only the outer domain touches the boundary (thus confining the inner domain and the domain wall). The confined inner domain together with the domain wall are often described as a quasi-particle, the so-called Skyrmion.

The special topology of Skyrmions has direct measurable implications. Most recently, it was found that electrons moving adiabatically through a magnetic Skyrmion collect a Berry phase, and that this phase can be expressed through the Aharonov-Bohm effect caused by an “emergent” magnetic field of the Skyrmion. This emergent magnetic field is proportional to the topological density  $n$ , and the Berry phase is proportional to the integrated enclosed flux, i.e., to the Skyrmion number. The interference of different paths around the Skyrmion leads to a deflection of the overall electron propagation direction, i.e., to a transverse current. This leads to a transverse voltage, the so-called topological Hall voltage.<sup>8,9</sup>

Another interesting property of magnetic Skyrmions is their outstanding insensitivity to magnetic pinning, at least in the collective motion of densely packed Skyrmions, so called Skyrmion lattices. The torque of conduction electrons on localized spin moments (the so-called spin transfer torque, predicted by Berger and Slonczewski)<sup>23,24</sup> and, consequently, the ability to drive domain walls by transmitted electric currents, are a subject of intense research nowadays. This technology is highly interesting for memory device applications, such as the racetrack memory proposed by Parkin *et al.*<sup>25</sup> However, magnetic pinning of domain walls has been found to be significant, and no motion has been observed for regular domain walls driven with current densities smaller than  $10^{11}$  A/m<sup>2</sup>. In contrast, for Skyrmion lattices, this critical current density is five orders of magnitude smaller.<sup>9</sup> So far, no theoretical explanation of the particularly low pinning of Skyrmions has been published, and if isolated Skyrmions show the same reduction of the critical current density remains to be verified. However, the confinement of Skyrmions intuitively leads to lower pinning compared to extended domain walls. This is firstly because, for topological reasons, Skyrmions never touch the edge of the sample, reducing the sensitivity to edge roughness and thus to the main source of pinning. And second, a fully confined structure is flexible to deform and to move around obstacles (provided the obstacles are not attractive).<sup>26</sup>

A third phenomenon that is directly associated with the Skyrmionic topology is a force that acts on a moving Skyrmion, pointing perpendicular to its velocity vector. This so-called gyroforce (or Magnus force in analogy to aerodynamics)

has been derived from the fundamental LLG equation by Thiele in 1973.<sup>27</sup> The equation of motion derived by Thiele for the center  $\mathbf{R}$  of a rigid Skyrmion in steady-state motion reads

$$\mathbf{G} \times \dot{\mathbf{R}} + D \dot{\mathbf{R}} - \partial_{\mathbf{R}} U = 0. \quad (1.1)$$

where  $\mathbf{G} = (0, 0, G)$  is the gyrocoupling vector with  $G = -4\pi N \mathcal{T} M_s / \gamma$  (where  $\mathcal{T}$  is the material thickness,  $M_s$  its saturation magnetisation, and  $\gamma = 1.76 \times 10^{11}$  As/kg the gyromagnetic ratio),  $D$  is the dissipation tensor, and  $U$  is the magnetostatic potential. Most importantly, the gyrocoupling vector  $\mathbf{G}$  depends only on material properties and on the topological quantum number  $N$ , and it has later been shown that the Skyrmion topological charge  $N$  can indeed be seen as an angular momentum.<sup>28</sup> The Thiele equation has been extended by Thiaville *et al.* to include the spin transfer torque,<sup>29</sup> and small corrections have been included by Krüger to accurately describe the motion of vortices instead of rigid Skyrmions.<sup>30</sup> Recently, Makhfudz *et al.* proposed to extend the first order Thiele equation for bubble Skyrmions by a second order derivative of  $\mathbf{R}$ , thus introducing an inertial mass term.<sup>31</sup> In this thesis, we measure this inertial mass, and we argue that its origin is due to the confinement of the Skyrmion that can be attributed to its topology.

## 1.2. History of Skyrmions in magnetism

Skyrmions in magnetism have been studied for a long time. Of all magnetic Skyrmions, magnetic bubbles are best known. These circular domains in an out-of-plane magnetized medium have been studied intensely from the 1960s until the 1980s, largely motivated by the potential for application in solid state storage devices,<sup>32</sup> which eventually lead to commercial devices.<sup>33</sup> Industrial interest in bubble media was finally lost due to the increased efficiency of rotating hard disks in the 1980s, boosted by the discovery of the giant magneto-resistance in 1988,<sup>34,35</sup> and the invention of flash memories.<sup>36</sup> However, the old concept of a storage medium that is based on domains moving in a solid state device is again facing tremendous interest, manifest in research on current-induced domain wall motion<sup>37</sup> and racetrack memory devices.<sup>25</sup> Because of their high mobility at ultra-low currents, Skyrmions are promising candidates for the realization of such a device, and it might prove useful to re-use the extensive knowledge of bubble-based technology. The work of this thesis, in which we investigate for the first time the dynamics of magnetic bubbles at short (ns) time scales, might contribute to form a link between known bubble physics and state-of-the-art research on application-related domain wall physics.

The original research on bubble domains was initiated by a work of Kooy and

Enz, who found an accurate theoretical model for the energetics and the evolution of stripe domains and bubbles under the application of an external magnetic field.<sup>38</sup> This static model was a first step towards controlled bubble generation and manipulation. Subsequently, experimental progress towards operational bubble-based devices was to a large extent lead by Andrew Bobeck and his team at the Bell Laboratories.<sup>32</sup>

On the theoretical side, two milestones for the understanding of the dynamics of bubble domains have to be mentioned. First, despite some crude assumptions, the one-dimensional model, which was formulated to describe the motion of bubbles and which we will discuss in more detail below, is extremely successful in describing the straight motion of magnetic domain walls. Today, the one-dimensional model can be considered the standard model of domain wall motion. The second important theory was the introduction of the gyrocoupling vector to the equation of motion of magnetic bubbles.<sup>27</sup> This work of Thiele was initiated by the observation of the so-called skew deflections of bubbles:<sup>18</sup> It was found that the trajectory of a bubble in general does not follow the field gradient, but rather that the steady state velocity has a significant component perpendicular to the gradient. The deflection angle is different for every bubble, and it was even not predictable if the bubble would be deflected to the right or to the left from the field gradient direction. Thiele's work, which was based on the assumption of a rigid bubble, successfully relates the deflection angle  $\xi$  of a bubble of radius  $R$  to its Skyrmion number  $N$  via  $\tan(\xi) = 2N\Delta_0/(R\alpha)$  (where  $\Delta_0 = \sqrt{A/K_{u,\text{eff}}}$  is the domain wall width parameter,  $A$  is the exchange stiffness,  $K_{u,\text{eff}}$  is the effective anisotropy energy, and  $\alpha$  is the viscous damping). The reason for the large variety of different deflection angles is the possible presence of so-called vertical Bloch lines in the domain wall of a bubble. Up to 180 of these topological defects have been observed in the domain wall of a single bubble of 4  $\mu\text{m}$  diameter, resulting in Skyrmion numbers of up to  $\pm 90$ .<sup>18</sup>

Bubbles exist in materials with preferred out-of-plane alignment of the magnetic moments. This is the best environment for Skyrmionic structures. Skyrmionic vector field configuration are most likely found if some energy of the system prefers the alignment of the vectors along a fixed axis. Otherwise, at least in magnetic systems of finite extent, the spins at the boundary prefer to lie in the tangent space of the boundary. Naturally, this contradicts the parallel alignment of all spins at the boundary (as the boundary is a closed loop). For thin film systems, only the axis perpendicular to the surface conserves the symmetry, and most magnetic materials with high uniaxial anisotropy have the easy axis along the film normal, leading to the name perpendicular magnetic anisotropy (PMA). However, the alignment of magnetic moments perpendicular to the film plane is energetically unfavorable due to the magneto-static energy  $\mu_0 M_s^2/2$  (where  $M_s$  is the saturation magnetization). The energy  $K_u$  associated with the uniaxial anisotropy has

to compensate the stray field energy due to the perpendicular alignment of the magnetic moments. In first order, this competition is quantified in the quality factor  $Q = 2K_u/(\mu_0 M_s^2)$ . All materials with  $Q > 1$  are preferably magnetized perpendicular to the film plane. Materials with  $Q \ll 1$  are in-plane magnetized, and regions with out-of-plane components, such as the core of a vortex, are kept as small as possible. There is an intermediate regime  $Q \lesssim 1$  in which the spins still prefer to point out of the plane, but domains have to be formed to reduce the stray field. In particular, the magnetization is no longer uniform along the vertical direction of the film. The critical parameter for out-of-plane spin alignment is the effective anisotropy  $K_{u,\text{eff}}$ , which is the anisotropy energy minus the real stray field energy of the actual domain configuration. The parameters  $K_u$ ,  $M_s$  and  $K_{u,\text{eff}}$  can be obtained from magnetometry data such as measured by superconducting quantum interference device (SQUID) magnetometry, which we discuss in more detail in chapter 3. Historically, bubbles have been investigated in materials with large  $Q$  (up to  $Q = 25$ ) and small  $M_s$  (of the order of some kA/m),<sup>18</sup> whereas the present study is based materials with  $Q \lesssim 1$  and large  $M_s$  of the order of MA/m.

There are various possible reasons for the presence of a uniaxial magnetic anisotropy in a thin film ferromagnet, all of which are based on an anisotropy of the underlying crystal structure. The coupling between the spin system and the lattice can be either through dipolar coupling (which is weak),<sup>39</sup> or through the spin-orbit interaction (which is the most prominent mechanism for magnetic anisotropy and, besides, also the origin for most interactions of electrons with spins).<sup>40</sup> The Coulomb exchange interaction of the Heisenberg model is always isotropic (even if the exchange integral  $J$  is not<sup>39</sup>), but the spin-orbit interaction can lead to anisotropic exchange-like terms such as the Dzyaloshinskii-Moriya interaction.<sup>18</sup> The spin-orbit interaction is a relativistic effect that arises from the helicity  $\hat{\sigma} \cdot \hat{\mathbf{p}}$  off-diagonal term of the Dirac equation ( $\hat{\sigma}$  is the Pauli matrix vector and  $\hat{\mathbf{p}}$  the momentum operator) in the presence of an electro-magnetic field  $A_\mu = (\phi, \mathbf{A})$ . The spin-orbit interaction comes with the first relativistic correction to the non-relativistic limit of the Dirac equation, and introduces a term  $\hat{H}_{\text{LS}} = q\hbar/(4m^2c^2) \hat{\sigma} \cdot (\nabla\phi \times \hat{\mathbf{p}})$ , which, for central electrical potentials  $\phi = \phi(r)$ , simplifies to  $\hat{H}_{\text{LS}} = q/(2m^2c^2r)(\partial_r\phi) \hat{\mathbf{L}} \cdot \hat{\mathbf{S}}$ . Most importantly, the coupling strength between the spin  $\hat{\mathbf{S}}$  and the angular momentum  $\hat{\mathbf{L}}$  of the fermion scales with the gradient of the electric potential  $r^{-1}\partial_r\phi$ . For this reason, strong spin-orbit interaction (and hence magnetic anisotropy) is found in materials containing elements with large nuclear charge  $Z$ , such as rare earth elements or heavy transition metals. In particular, the  $4f$  electrons are affected by the spin orbit coupling, because they carry large angular momenta, and because they are highly localized due to the angular momentum energy barrier (that is, they are confined to small  $r$  and therefore feel only little core potential screening).<sup>40</sup> Even though the spin-orbit interaction is the most significant mechanism for magnetic anisotropy, it is often difficult to

quantify the contributions of all the anisotropic bonds present in a sample system. Historically, bubble materials were ferrimagnetic (materials with antiferromagnetically coupled sublattices with different saturation magnetization), with the PMA arising probably from dipolar interactions, anisotropic (Dzyaloshinskii-Moriya) exchange, and single ion magneto-crystalline anisotropy.<sup>18</sup> The origin of PMA in the Co/Pt, Co/Pd, and CoB/Pt multilayers investigated in this thesis is not much better understood; spin-orbit effects in the interface Co 3d ligand orbitals are providing a significant contribution,<sup>41</sup> but also magnetostriction (anisotropy due to crystal strain) and magneto-crystalline anisotropy are not negligible, in particular in Co/Pd multilayers<sup>42,43</sup> and in CoPd alloys.<sup>44</sup>

### 1.3. Magnetic field-induced domain wall motion

In this thesis, we will analyze the trajectory of a single bubble Skyrmion during and after its excitation with a magnetic field pulse. We will therefore briefly review the main aspects of magnetic field driven domain wall motion. The following discussion is largely inspired by the arguments given in Refs. 18 and 30, converted to SI units and adapted to the approximations valid in the present work.

The dynamics of a magnetic system, described in the micromagnetic framework, is determined by the Landau-Lifshitz-Gilbert (LLG) equation:

$$\dot{\mathbf{M}} = \gamma \mathbf{M} \times \frac{\delta E}{\delta \mathbf{M}} + \alpha \frac{\mathbf{M} \times \dot{\mathbf{M}}}{M_s}. \quad (1.2)$$

Here,  $\mathbf{M} = \mathbf{M}(\mathbf{r})$  is the magnetization vector,  $\gamma$  is the gyromagnetic ratio,  $\alpha$  is the viscous (Gilbert) damping,  $M_s = |\mathbf{M}|$  is the saturation magnetization, and  $E[\mathbf{M}] = \int dV w[\mathbf{M}]$  is the total energy functional (and not the energy density as stated in Ref. 18). The superscript dot denotes the total time derivative, and the  $\delta$  symbol the functional derivative, which can be expressed as an ordinary derivative of the energy density  $w$  via

$$\frac{\delta E}{\delta \mathbf{M}} = \frac{\partial w}{\partial \mathbf{M}} - \sum_i \frac{d}{dx_i} \frac{\partial w}{\partial (\mathbf{M}/dx_i)}. \quad (1.3)$$

The first term on the right hand side of Eq. (1.2) leads to a precession of the magnetization, whereas the second term leads to the dissipation of energy and the alignment of the moments along the effective field  $\mu_0 \mathbf{H}_e = -\delta E/\delta \mathbf{M}$ .

In the following, we will assume a preferred spin alignment along the  $z$ -direction (arising from a uniaxial anisotropy with anisotropy constant  $K_u$ ), and we will use Cartesian coordinates  $\mathbf{r} = (x, y, z)$  for the domain space and spherical coordinates  $\mathbf{M} = (M_s, \phi, \theta)$  for the magnetization space.  $M_s$  is assumed constant, and the

LLG equation can be written in terms of  $\theta$  and  $\phi$ :

$$\dot{\theta} = -(\gamma/M_s) \frac{1}{\sin(\theta)} \frac{\delta E}{\delta \phi} - \alpha \dot{\phi} \sin(\theta), \quad (1.4)$$

$$\dot{\phi} \sin(\theta) = (\gamma/M_s) \frac{\delta E}{\delta \theta} + \alpha \dot{\theta}. \quad (1.5)$$

The dynamics is driven by gradients of the total energy  $E$ . We will discuss the energetics of our ferromagnet system in terms of the energy density  $w$ , which is the relevant parameter for the local dynamics according to Eq. (1.3). In the magnetic systems investigated in this thesis, exchange energy  $w_A$ , anisotropy energy  $w_K$ , and demagnetization (stray field) energy  $w_D$  are intrinsically present. The exchange energy scales with the cosine of the angle between adjacent spins, which can be approximated in first order (small angles) by

$$w_A = A [(\partial_{\mathbf{r}} \theta)^2 + (\sin(\theta) \partial_{\mathbf{r}} \phi)^2]. \quad (1.6)$$

The uniaxial anisotropy prefers an alignment of the magnetization along the  $z$ -axis, which, for symmetry reasons, can be expressed in terms of even powers of  $\sin(\theta)$ . The leading term reads

$$w_{K_u} = K_u \sin^2(\theta). \quad (1.7)$$

The stray field (demagnetizing field)  $\mathbf{H}_D$  of a magnetic system can be obtained by the exact analogy between electrical charges  $q$  and magnetic charges  $\text{div} \mathbf{M}$  through the virtual identity  $q = -c \text{div} \mathbf{M}$  (with  $c = 1/(\mu_0 \epsilon_0)$  the speed of light in vacuum). Hence,

$$\mathbf{H}_D(\mathbf{r}) = -\frac{1}{4\pi} \partial_{\mathbf{r}} \int [\text{d}V' \rho_V(\mathbf{r}') + \text{d}S' \rho_S(\mathbf{r}')] \frac{1}{|\mathbf{r} - \mathbf{r}'|} \quad (1.8)$$

with the volume and surface charges, respectively, given by

$$\rho_V(\mathbf{r}) = -\text{div} \mathbf{M} \quad (1.9)$$

$$\rho_S(\mathbf{r}) = \mathbf{M} \cdot \mathbf{n}. \quad (1.10)$$

Here,  $\mathbf{n}$  is the surface normal vector pointing away from the magnetic material. The associated stray field energy density is given by Zeeman term

$$w_D = -\mu_0 \mathbf{H}_D \cdot \mathbf{M}/2, \quad (1.11)$$

where the factor  $1/2$  accounts for double-counting of the same magnetic moments in the factors  $\mathbf{H}_D$  and  $\mathbf{M}$ . Despite being given as a volume density, the stray field energy is highly non-local (the integrand in Eq. (1.8) decays very weakly as  $1/r$ ), resulting in tremendous difficulties in solving the equation of motion, both ana-

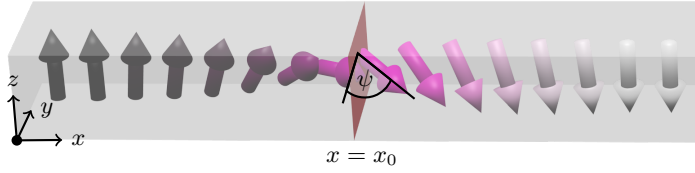


**Figure 1.3 | Profile of a domain wall.** The spins rotate from  $\theta = 0$  (left) to  $\theta = \pi$  (right). The azimuthal angle  $\phi(\mathbf{r}) = \psi$  is equal for all spins. The red plane visualizes the position taken as the domain wall location  $x = x_0$ , defined as the symmetry plane of the domain wall.

lytically as well as numerically. Common approximations found in the literature assume samples that are infinite in either one, two, or all three dimensions, and of zero extent in the remaining directions. Models for surface stray fields often assume single-domain states in 2D samples, where the stray field energy is given by  $\mu_0 M_s^2/2$ . Based on these approximations, it is often claimed that magnetic materials exhibit out-of-plane domains only if  $Q > 1$  because otherwise the stray field energy would drive the magnetic moments in-plane. However, the stray field energy of a sample that shows domains is smaller than  $\mu_0 M_s^2/2$ , and the fact that the materials investigated in this thesis are out-of-plane magnetized even though  $Q < 1$  demonstrates the need to develop suitable approximations for the specific materials and geometries used here. A precise discussion on the stray fields and minimum energy domain configurations for all possible values of  $Q$  can be found in Ref. 45. The stray field energy of the specific material used in the investigation of domain dynamics in the present work is derived in Appendix A.

We are interested in the dynamics (and hence the energetics) of domain walls. The wall dynamics investigated in the present work is observed in a thin magnetic sample, sufficiently far away from the edge of the structure. Therefore, we will assume an infinite extent in the  $x$  and  $y$  directions. Consider a domain wall, i.e., a spin system with an up-domain on the left [ $\theta(x = -\infty, y, z) = 0$ ] and a down-domain on the right [ $\theta(x = +\infty, y, z) = \pi$ ]. A first idea of the profile of a domain wall is provided by the stationary solution [ $\delta E/\delta\theta = 0$  and  $\delta E/\delta\phi = 0$ ] of Eqs. (1.4) and (1.5) in the absence of stray fields ( $w = w_A + w_{K_u}$ ):

$$\theta(x, y, z) = 2 \arctan(\exp((x - x_0)/\Delta_0)), \quad (1.12)$$

$$\phi(x, y, z) = \psi \quad (1.13)$$

where the domain wall width parameter  $\Delta_0$  is given by

$$\Delta_0 = \sqrt{A/K_u} \quad (1.14)$$

and the position of the domain wall  $x_0$  is an arbitrary parameter (not influencing the energy of the wall). This domain wall profile is visualized in Fig. 1.3.

If demagnetization energies are included, the uniaxial anisotropy is effectively reduced because surface charges are generated by magnetic moments pointing perpendicular to the surface. Furthermore, domain walls with  $\psi = 0$  (Bloch walls) become favorable due to the absence of volume charges. The surface charges can be included in the model by replacing  $K_u$  by an effective out-of-plane anisotropy  $K_{u,\text{eff}}$ , and the volume charges are accounted for by adding a  $\psi$ -dependent term to the anisotropy:

$$w_K = K_\psi \sin^2(\theta) \quad (1.15)$$

$$K_\psi = K_{u,\text{eff}} + K_\perp \sin^2(\psi) \quad (1.16)$$

The corrected domain wall profile reads

$$\theta(x, y, z) = 2 \arctan(\exp((x - x_0)/\Delta)), \quad (1.17)$$

$$\phi(x, y, z) = \psi \quad (1.18)$$

$$\Delta(\psi) = \sqrt{A/K_\psi} \quad (1.19)$$

$$\psi = 0 \quad (1.20)$$

and its energy per unit area is given by

$$\sigma_i = \int w \, dx = 4\sqrt{AK_\psi}, \quad (1.21)$$

where in the static case ( $\psi = 0$ ),  $K_\psi = K_{u,\text{eff}}$ . The parameter  $K_{u,\text{eff}}$  can be determined experimentally. The transverse anisotropy constant  $K_\perp$  can be estimated either semi-analytically by some assumptions for the 3D spin configuration (see Appendix A), or by micromagnetic simulations. For now, we will use  $K_\perp$  as a parameter that remains to be determined.

The motion of a wall of the form given in Eqs. (1.17) – (1.20) can be approximated by assuming that the shape of the wall is preserved during the motion (rigid shape) and that only the parameters  $x_0 = x_0(t)$ ,  $\psi = \psi(t)$ , and, implicitly, the domain wall width  $\Delta = \Delta(\psi(t))$ , are time-dependent (which might not be a good approximation for  $Q \lesssim 1$ ). It turns out that  $x_0$  and  $\psi$  form canonical conjugates ( $x_0$  corresponding to a generalized coordinate and  $\psi$  to its conjugated momentum), and that the model becomes one-dimensional (1D). There is also a one-to-one correspondence between the 1D variables and the magnetization angles in the LLG equation, that is,  $x_0$  corresponds to  $\theta$  and  $\psi$  corresponds to  $\phi$ . The



equations of motion are given by

$$\frac{\partial \sigma}{\partial \psi} = \frac{2M_s}{\gamma}(\dot{x}_0 - \alpha \Delta \dot{\psi}), \quad (1.22)$$

$$\frac{\partial \sigma}{\partial x_0} = -\frac{2M_s}{\gamma}(\dot{\psi} + \alpha \dot{x}_0 / \Delta). \quad (1.23)$$

Here,  $\sigma = \sigma_i + \sigma_e$  is the total domain wall energy per unit area, a sum of an intrinsic and an extrinsic contribution. The latter describes the energetics due to environmental influences (applied fields, transmitted currents, etc.). The term  $\partial_\psi \sigma$  determines the deformation of the wall (energy associated with a tilt of  $\psi$ ), whereas the term  $\partial_{x_0} \sigma$  introduces the driving force (energy gained by moving  $x_0$ ). We can use Eq. (1.21) to calculate the left hand side of Eq. (1.22), assuming that only the intrinsic energy  $\sigma_i$  depends on  $\psi$  and using that only the extrinsic energy  $\sigma_e$  depends on  $x_0$ . We arrive at

$$\dot{x}_0 = \frac{\gamma \Delta K_\perp}{M_s} \sin(2\psi) + \alpha \Delta \dot{\psi}, \quad (1.24)$$

$$\dot{\psi} = -\frac{\gamma}{2M_s} \frac{\partial \sigma_e}{\partial x_0} - \alpha \dot{x}_0 / \Delta. \quad (1.25)$$

We can now insert  $\dot{\psi}$  from Eq. (1.25) in Eq. (1.24), linearize in  $\psi$  for small angles [i.e.,  $\Delta \rightarrow \Delta_0 = \sqrt{A/K_{u,\text{eff}}}$  and  $\sin(2\psi) \rightarrow 2\psi$ ], extract  $\psi(x_0)$  by using that  $\partial_q \sigma_e$  is not a function of  $\psi$ , and insert this to Eq. (1.25) to obtain an equation for  $x_0$  alone:

$$m_D \ddot{x}_0 + b \dot{x}_0 + F = 0, \quad (1.26)$$

with the so-called Döring mass density<sup>46</sup> (domain wall mass per unit area)

$$m_D = \frac{M_s^2(1 + \alpha^2)}{K_\perp \gamma^2 \Delta_0}. \quad (1.27)$$

The other coefficients are  $b = \frac{2M_s \alpha}{\gamma \Delta_0}$  and  $F = \partial_{x_0} \sigma_e + \frac{\alpha M_s}{2K_\perp \gamma} \frac{d}{dt} \partial_{x_0} \sigma_e$ . Eq. (1.26) is the equation for the so-called domain wall oscillator. We emphasize that we used small-angle approximations for  $\psi$  to derive this formula, which is therefore only valid to describe the start of the domain wall motion or the motion at very small drive forces  $\partial_{x_0} \sigma_e$ .

The Döring mass of a straight domain wall is so far the only experimentally confirmed theory of inertia in magnetic systems, and it is an emergent phenomena because the LLG equation *a priori* does not include a second order derivative. Thus, a single spin has no inertia. We will show in this thesis that the inertia of magnetic bubbles exceeds the expected Döring mass by more than a factor of five. We will argue that this lends itself to a new concept, the topological mass.

## 1.4. Detection of domain wall dynamics

The phenomenological Landau-Lifshitz-Gilbert equation is the fundamental equation governing the dynamics of every spin systems and has been well proven for already 80 years by now. Based on this fundamental equation, one can carry out micromagnetic simulations to calculate the relaxed configurations and the dynamical response of a spin system. Such simulations have become a powerful and highly reliable tool that, to some extent, is capable of replacing experimental investigations in a number of scientific problems. However, micromagnetic simulations can be at most as accurate as the parameters of the system provided by the user. In particular for multilayer systems, magnetic properties are highly inhomogeneous, and even if we precisely knew their functional dependence on all three spatial coordinates, we would need to use tiny cells for the discrete model to account for their rapid fluctuations, leading to unacceptable computational efforts. Therefore, the investigation of emergent dynamical phenomena in large and complex spin systems is still widely carried out using experimental approaches. Here, we provide an overview of the most established experimental techniques to detect spin dynamics, of which we distinguish imaging techniques from indirect electrical measurements. We start with electrical detection schemes, also referred to by transport measurements.

An established geometry for the investigation of domain wall dynamics is the wire. The conventional approach for detecting the presence of domain walls in such a magnetic wire is to measure changes in the conductivity tensor. The longitudinal conductivity of the wire is changed if the magnetization is parallel to the current direction compared to the perpendicular orientation,<sup>37,47</sup> such that the presence of a domain wall in an in-plane magnetized wire can be detected by a change in the resistance.<sup>22</sup> This effect, which can have positive or negative sign,<sup>47,48</sup> is called anisotropic magneto-resistance (AMR). However, in out-of-plane magnetized structures such as investigated in this thesis, AMR-based measurements are much more difficult to realize: Néel walls are very narrow compared to walls in in-plane magnetized structures leading to tiny AMR signals, and Bloch walls are not detectable at all (since the all spins point perpendicular to the current). A much stronger signal is provided by the anomalous Hall effect (AHE):<sup>49</sup> A current through a perpendicularly magnetized wire leads to a transverse voltage in the direction perpendicular to the current and to the magnetization, which can be measured using transverse contacts on the wire. The signal is proportional to the integral out-of-plane component of the magnetization in the contact area. Therefore, a domain wall can be tracked in discrete steps and its average velocity can be determined provided multiple such Hall bars are present along the wire.<sup>50</sup> It is furthermore possible to study the depinning of a domain wall from the Hall probe area.<sup>51</sup> The AHE is not used in in-plane magnetized structures because it

is difficult to contact the bottom and the top of the wire (without shunting), and because the Hall voltage would be small in thin films.

A particularly large change of the resistance (giant magneto-resistance, GMR) is observed when switching one of two parallel magnetic layers that are separated by a conducting non-magnetic spacer, provided this spacer layer is thinner than the mean spin flip scattering length.<sup>34,35,52</sup> The GMR signal can be observed both for currents flowing in-plane (current in-plane, CIP) as well as for currents flowing perpendicular to the plane (current perpendicular to plane, CPP).<sup>52</sup> The relative effect can be increased further by using a tunnel barrier instead of a conducting spacer (tunnel magneto-resistance, TMR).<sup>53</sup> However, this increase of the relative signal is accompanied by a reduction of the conductivity, which sometimes becomes problematic when using very small devices. Often, one of the two layers is magnetically soft (has very low coercivity) and the other one is magnetically hard (has high coercivity, typically arising from the exchange coupling to an antiferromagnetic seed layer). In this configuration, GMR and TMR stacks (in this context also called spin valves, or magnetic tunnel junctions (MTJs) for TMR stacks) have wide applications in the detection of domains, most prominently in magnetic hard disk read heads.<sup>52</sup> GMR and TMR devices can be used to detect the position of a domain wall continuously through the potentiometer-like gradual change of the GMR as a function of domain wall position in a spin valve nanowire.<sup>54,55</sup>

The methods discussed so-far aim to obtain real-space information about the spin structure, such as the position of a domain wall. Other transport measurement techniques operate in the frequency domain. For instance, resonances in the excitation spectrum of a magnetic configuration can be determined by measuring the power required to sustain an excitation as a function of excitation parameters (such as frequency, amplitude, orientation, etc.),<sup>56</sup> or by homodyne detection.<sup>21</sup> For example, the gyrotropic motion of a vortex core has a resonance frequency that depends on the gyrovector  $\mathbf{G}$ , the dissipation  $D$ , and the potential  $U$ . That is, the resonance frequency may depend on the location of the vortex core in the magnetostatic potential, and on the direction and the amplitude of the excitation. A detailed resonance study provides, for instance, information about the potential  $U(\mathbf{r})$ ,<sup>57</sup> and knowledge about the resonances may be used to switch a vortex core with very low excitation amplitudes.<sup>58</sup>

In investigations based on transport measurements, both the sample fabrication and the measurement are automatable and scalable, and measurements can be carried out using lab-based equipment. Thus, these techniques are extremely useful for high throughput characterization, material optimization, and to address fundamental questions that require large statistics or investigations in a high dimensional parameter space. As a drawback, no detailed information about the spin structure of a traveling domain wall is obtained. This information is only accessible by direct imaging, where nanometer spatial and picosecond temporal

resolution is required to capture the details of the domain wall motion. Multiple techniques are available for magnetic imaging. We will briefly present the most established methods. More detailed reviews can be found, e.g., in Refs. 45, 59, and 60.

The first and oldest large family of instruments for magnetic domain imaging uses optical effects in the visible light regime. Historically, the first instruments for imaging magnetic domains with present-day applications are Kerr and Faraday microscopes. Both gain magnetic sensitivity from the rotation of the polarization axis of optical light when reflected by (Kerr) or transmitted through (Faraday) a magnetic layer.<sup>45</sup> A magnetic image is recorded using two polarizing filters before and after the object under investigation. Kerr microscopy provides high contrast, very quick image accumulation, and little disturbance by electromagnetic sample excitations at low cost in a table-top setup. With modern femtosecond lasers, Kerr microscopes can acquire dynamic images with unbeaten temporal resolution.<sup>61</sup> As a drawback, the spatial resolution of visible light microscopy is insufficient to resolve features on the nanometer scale.<sup>62</sup>

The second family of domain imaging systems consist of scanning probe microscopes. These instruments, in which the sample is scanned with a small (ideally atomically sharp) tip, are very compact and can be operated on a normal desk, even though high resolution imaging requires good vibrational isolation and vacuum conditions. Specific examples are magnetic force microscopes (MFM) with a magnetic tip and scanning tunneling microscopes with a spin-polarized conducting probe tip (SP-STM).<sup>63</sup> In MFM, the tip senses the local magnetization by being attracted or repelled through the interaction with the stray field of the domains, while at the same time the stray field of the tip might induce changes in the sample. In SP-STM, a tunneling current between sample and tip is recorded and related to the orientation of the local magnetization with respect to the polarization of the tip similarly to the TMR effect. These techniques provide very high spatial resolution: SP-STM and the recently demonstrated magnetic exchange force microscopy (MExFM)<sup>64</sup> have the best spatial resolution of all imaging techniques, i.e., single spin detection has been demonstrated. However, no time-resolved imaging has been reported to far, and the magnetic imaging of topographic structures is extremely difficult.

Electron microscopes form the third large family of magnetic imaging tools. Prominent members are the scanning electron microscope (SEM), the low energy electron microscope (LEEM), the transmission electron microscope (TEM), and photo emission electron microscope (PEEM). Despite the challenges arising from the interaction of the probing electrons with sample excitations (electric as well as magnetic fields), electron microscopes are well established and powerful tools for the high resolution imaging of domain dynamics,<sup>65,66</sup> and as such will be briefly discussed here.

In an SEM and in a LEEM, a special detector can be used to analyze the spin polarization of the secondary or backscattered electrons; these devices are called SEM with polarization analysis (SEMPA) and spin-polarized LEEM (SPLEEM).<sup>60</sup> The information about the polarization of surface emitted electrons can be used to deduce the magnetization orientation of the probed area, and thus obtain an image of the domain structure of the sample. Both techniques are sensitive to the magnetism in a small region near the surface of the samples.

In a TEM, high energy electrons are transmitted through very thin samples to generate an image using the wave properties of the electrons, similar to optical microscopy. Because of the short wave lengths of high energy electrons ( $\lambda = 3.7$  pm for electron energies of 100 keV), sub-atomic resolution can be achieved. Various modes are available for magnetic imaging in a TEM. In Lorentz mode, a magnetic flux inside the sample results in an Aharonov-Bohm phase for the transmitted electrons, which can be made visible by a defocussed illumination (as in traditional phase microscopy).<sup>65</sup> Classically, the phase can be understood in terms of a Lorentz force acting on the moving electrons, hence the name Lorentz TEM mode. Lorentz TEM provides nanometer spatial resolution for magnetic imaging,<sup>65</sup> which has been particularly successful in imaging the real space spin arrangement of chiral Skyrmions.<sup>7</sup> The second TEM operation mode is electron holography, which, apart from other features, provides quantitative access to the local magnetic flux.<sup>67,68</sup>

In contrast to SEM, LEEM, and TEM, the electrons in PEEM are emitted from the surface due to the photo-effect of incident x-rays, and not due to exposure with other electrons. The number of emitted electrons scales with the photon absorption cross section, and by using circularly polarized photons of a particular energy, magnetic sensitivity for the component of the magnetization parallel to the polarization vector of the light is provided by the x-ray magnetic circular dichroism (XMCD).<sup>69</sup> Most PEEMs operate at grazing incidence and are therefore sensitive to the in-plane magnetization near the sample surface. PEEMs as well as TEMs are very successfully used in the imaging of spin dynamics.<sup>59,65,66</sup> In particular, TEM was one of the first techniques to provide picosecond temporal and simultaneously sub-100 nm spatial resolution. Already in 1984, stroboscopic dynamic imaging has been performed with a temporal resolution of 200 ps,<sup>65</sup> which is sufficient for most domain wall dynamics.

The last large family of imaging tools is characterized by the use of (soft) x-rays as a probe with the XMCD effect providing magnetic contrast. Prominent members are the PEEM (which belongs also to the family of electron microscopes and as such has been discussed before), the transmission x-ray microscope (TXM),<sup>70</sup> and the scanning transmission x-ray microscope (STXM).<sup>71</sup> The latter two instruments are purely optical, and thus, compared to electron microscopes, much less affected by electro-magnetic fields in the vicinity of the sample. The TXM can be seen as an analog to the optical microscope, with enhanced resolution by using

smaller probing wave lengths. Lenses at the wavelengths of soft x-rays are realized by diffractive elements, so-called zone plates, which are difficult to fabricate and therefore very expensive. STXM requires only one lens instead of two, and furthermore can be used to image non-transparent conducting samples based on total electron yield (TEY) measurements (recording the total current required to replace emitted photo-electrons),<sup>72,73</sup> or to image thin films on fluorescent substrates.<sup>74,75</sup> STXM is one of the techniques used in this thesis, and, as such, will be presented in more detail in chapter 3. PEEM,<sup>59,66</sup> TXM,<sup>76</sup> and STXM,<sup>77</sup> are successfully used in stroboscopic dynamic imaging of domain dynamics.

The dynamic imaging of the Skyrmion dynamics observed in this thesis was made possible by a novel, unconventional technique: Fourier transform holography (FTH or x-ray holography), which offers features unmet by any of the above listed instruments. In particular, x-ray holography is intrinsically immune to drift in the experimental setup, which allows us to track features in the images (such as the center of the Skyrmions) with an unbeaten spatial resolution of better than 3 nm. X-ray holography was first successfully realized in 2004 by S. Eisebitt *et al.*,<sup>78</sup> and has seen dramatic improvements since then. As part of this work, time-resolved pump-probe x-ray holography has been developed, and the efficiency has been optimized to allow for the acquisition of movies in a reasonably short time. A detailed description of this experimental technique can be found in chapter 2.

# Chapter 2

## Sample fabrication and experimental setup for time-resolved x-ray holography

---

*Soft x-ray holography is a recently developed imaging technique with sub-50 nm spatial resolution. Key advantages of this technique are magnetic and elemental sensitivity, compatibility with imaging at free electron laser facilities, and immunity to in-situ sample excitations and sample drift, which enables the reliable detection of relative changes between two images with a precision of a few nanometers. In x-ray holography, the main part of the experimental setup is integrated in the sample, which consequently requires a large number of fabrication steps. Here we present a generic design and an automatable fabrication process for samples suitable, and optimized for, efficient high resolution x-ray holographic dynamic imaging. The high efficiency of the design facilitates the acquisition of magnetic images in a few minutes and makes fully automatic image reconstruction possible.<sup>‡</sup>*

---

### 2.1. Introduction

Soft x-ray Fourier transform holography (FTH) is a coherence-based imaging technique that, in contrast to other existing imaging tools, requires neither lenses nor other optical elements for the image acquisition.<sup>78</sup> Instead, the Fraunhofer far field scattering intensity of the sample is recorded, which is given by the amplitude squared of the Fourier transform of the sample transmission function. This transmission function can be digitally reconstructed by an inverse Fourier transform to obtain an image of the object of interest. Such a reconstruction is possible because the required phase information is encoded in the interference pattern between the beam scattered from the sample and a coherent reference beam from a point-like source.<sup>78‡</sup>

X-ray holography is the only x-ray imaging technique encoding the full complex wave field information. As such, it has a number of advantages: (i) Because no optical elements are required in the focused beam, it is suitable for fully destruc-

tive single shot imaging with a very intense photon pulse such as those provided by free electron laser sources.<sup>79</sup> (ii) In such a single shot image, time delays can be encoded, allowing for single shot femtosecond dynamic imaging,<sup>80</sup> which is the best temporal resolution reported for the dynamic imaging with sub-50 nm spatial resolution so far. As a further advantage, the imaging acquisition in such a single shot experiment does not require pump-probe reproducibility. (iii) The full wave field information enables post-process refocusing through computational wave field propagation,<sup>81</sup> reconstruction of 3D information<sup>82</sup> from a single hologram, and *a posteriori* numerical generation of various contrast mechanisms.<sup>83</sup> (iv) Any drift during the imaging results in a shift in the Fourier space scattering pattern and thus translates into a phase shift in the real space reconstruction. There is no drift of the real space information as long as the internal structure of the object is rigid. It has been demonstrated that this leads to a resolution of better than 3 nm when tracking the center of mass of specific features in a dynamic imaging experiment.<sup>84</sup> (v) The imaging is based purely on photons, and is therefore practically insensitive to electro-magnetic fields in the vicinity of the sample. This, in combination with the large space available around the sample (since no other optical elements are required), makes this technique particularly well suited for sample characterizations in extreme environments, such as simultaneous large magnetic fields and low temperatures.<sup>85</sup> However, despite all these outstanding features, FTH is still not widely used. The most significant hindrance is the complexity of the sample fabrication, which we address in this chapter.<sup>#</sup>

Despite the critical role played by the sample fabrication for x-ray holography, little details of the fabrication steps have been addressed in a systematic fashion in the literature. Also, a number of approaches such as movable masks<sup>81,86</sup> and holography with multiple objects holes<sup>87–90</sup> exist, without any reports comparing their performance. Here, we report the details of the fabrication of x-ray holography samples optimized for high performance and suitable for pump-probe magnetic imaging. Major parts of the process are generic and can be adapted for any holographic sample. We show that, to a large extent, both the sample fabrication as well as the image reconstruction are automatable and thus allow for high throughput with minimum human workload.<sup>#</sup>

## 2.2. Methods

The nanostructuring of the samples is performed by electron beam lithography (EBL) using a Vistec EBPG 5000 operating at 100 kV acceleration voltage and by focused ion beam (FIB) milling using a dual beam FEI Helios NanoLab 600, which provides a  $\text{Ga}^+$  ion beam at variable ion energies of up to 30 keV. Parts of this process have been successfully tested on a widely available Raith e\_LiNE and on a Raith PIONEER EBL system, both operated at 20 kV acceleration voltage.



Sample characterization is performed using standard scanning electron microscopy (SEM), transmission electron microscopy (TEM), and x-ray holographic imaging at the UE52-SGM beamline of BESSY II (Berlin). The FTH performance test is carried out in the single bunch mode, in which the repetition rate of the incident photon pulses is reduced to 1.25 MHz, making it most interesting for pump-probe dynamic imaging.<sup>#</sup>

## 2.3. Sample fabrication steps

X-ray holography samples consist of two parts: (i) a holographic mask with (at least) two apertures (a larger one defining the field of view, and a smaller one, ideally point-like, providing the reference beam), and (ii) the object of interest, which is positioned in close proximity in front or behind the larger aperture. The larger aperture is typically a hole in an opaque film, referred to as object hole. It is highly beneficial to integrate the object in the holographic mask, to ensure that the mask does not drift with respect to the object. The fabrication steps of such an integrated sample, which we will discuss in detail next, are schematically depicted in Fig. 2.1, and micrographs of the sample at important steps are presented in Figs. 2.2–2.4. Steps 1 (object aperture) and 5 (reference) are generic for all holography samples. Steps 2 (alignment) and 3 (specimen) show one possibility of precisely aligning a particular specimen with the field of view, and step 4 (microcoil) provides an example of integrating a pump-probe excitation setup in the sample.<sup>#</sup>

### 2.3.1. Substrates

The samples presented here are designed for imaging in the extreme ultra-violet to soft x-ray regime, i.e., for energies between 50 eV and 900 eV. The light in this energy range has wide applications in scientific research (i) because the wavelength resolution limit is in the low nanometer regime and (ii) because many important characteristic resonances of different materials in this regime provide access to a large variety of material properties (such as the local magnetization through the x-ray magnetic circular dichroism (XMCD) effect<sup>69</sup>). However, in this energy range, all materials absorb strongly, and therefore the samples have to be sufficiently thin to allow for FTH transmission-based imaging. Widely used substrates are low stress Si<sub>3</sub>N<sub>4</sub> membranes, which are commercially available and can be purchased in thicknesses ranging from some ten nanometers up to about one micrometer, with lateral diameters ranging from a few micrometers up to a few millimeters. Here we use 350 nm thick membranes of  $10 \times 10 \mu\text{m}^2$  lateral size on  $5 \times 5 \times 0.2 \text{ mm}^3$  Si frames bought from Silson Ltd.<sup>91#</sup>

The customized substrates, schematically shown in Fig. 2.1a, are prepared by

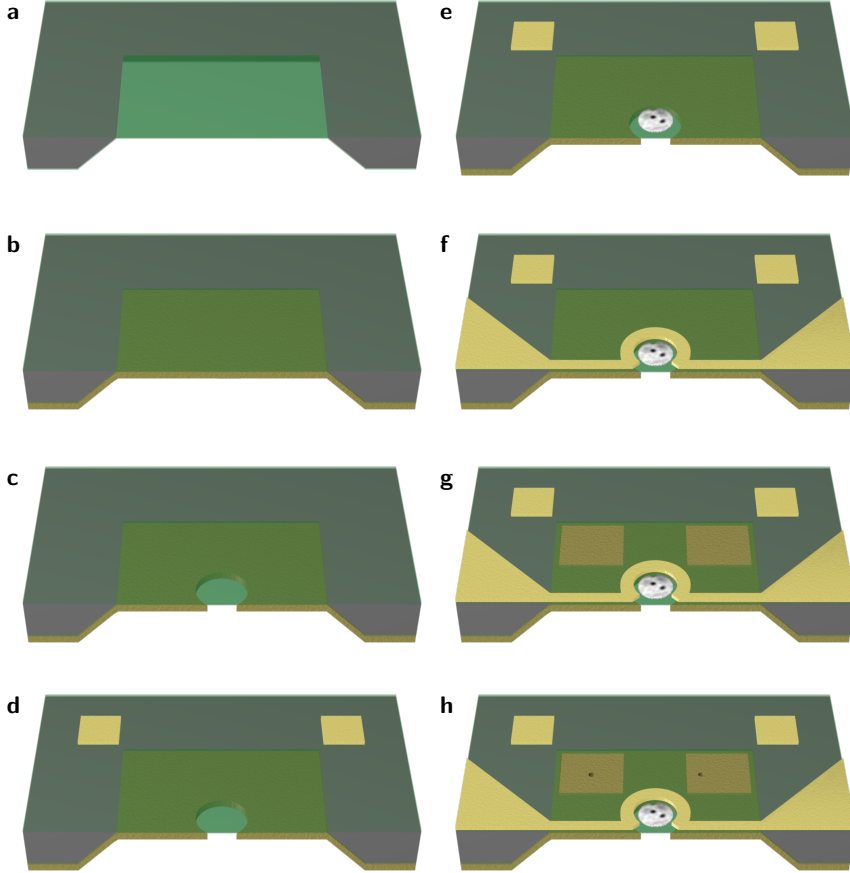


**Figure 2.1 | Sample fabrication steps for pump-probe x-ray holography.** (a) Si frame (gray) with  $\text{Si}_3\text{N}_4$  membrane (transparent green) and extra  $\text{Si}_3\text{N}_4$  coating on the back side. (b) Deposition of a Cr/Au multilayer on the back of the membrane. (c) FIB milling of an 800 nm diameter object hole in the Cr/Au film. (d) EBL definition of aligned markers on the flat membrane. (e) Preparation of a magnetic specimen (here: a disk) on the top side of the sample, aligned with respect to the center of the object hole (after film deposition, EBL etch mask fabrication, and Ar milling). (f) EBL fabrication of the microcoil around the magnetic disk. (g) Local removal of the  $\text{Si}_3\text{N}_4$  for the reference milling by FIB. (h) FIB milling of the reference holes in the Cr/Au multilayer.<sup>#</sup>

lithographically defining etch mask windows on a  $\text{Si}_3\text{N}_4$  film deposited on the back of the  $\text{Si}_3\text{N}_4/\text{Si}(001)$  samples and etching the Si through the back using a KOH solution to expose the top  $\text{Si}_3\text{N}_4$  film from the bottom.<sup>92</sup> High-ohmic Si is used to keep the electrical capacitance of the substrate at a minimum and, therefore, to permit high frequency electrical circuits on the samples. Furthermore, of the total 350 nm  $\text{Si}_3\text{N}_4$ , 200 nm are deposited on the Si wafers before the KOH etching, and the remaining 150 nm are deposited on the back side after the etching to provide a good insulation against the sample holder. The thickness of the  $\text{Si}_3\text{N}_4$  chosen corresponds to a compromise between, on the one hand, good x-ray transmission (thinner membranes) and, on the other hand, mechanical stability, tolerances in the subsequent sputter etch processes, and good electrical insulation with respect to the back side of the membrane at high frequencies (thicker membranes). The lateral dimensions were made as small as possible while still compatible with the fabrication process. This enhances the mechanical stability and helps keeping the electrical resistance of impedance-matched transmission lines on the sample low (see section 2.3.5). The outer dimensions of the Si frame warrant convenient handling of the samples throughout the whole process and, at the same time, provide economic use of the wafer substrates. Membrane substrates such as described here are available in wafers with arrays of up to several hundred single membranes, and parallel processing of a whole 4 inch wafer is possible in all subsequent steps.<sup>#</sup>

### 2.3.2. Step 1: Object aperture

To define the object aperture, the  $\text{Si}_3\text{N}_4$  membrane is first covered from the back side with a thermally evaporated  $[\text{Cr}(5)/\text{Au}(55)]_{20}$  (thicknesses given in nm) multilayer (Fig. 2.1b). This multilayer is fully opaque to the incident x-rays (transmission of less than  $10^{-6}$  for the whole given energy range; the number of repeats can be adapted for applications in a more specific energy range). The periodic interruption of the Au layers by thin Cr layers prevents the formation of large Au grains, which increases the reproducibility of the milling rates in FIB structuring. In this opaque Cr/Au multilayer thin film, a small aperture of about 800 nm diameter is milled by FIB at 8 kV acceleration voltage and 70 pA beam current, stopping at the x-ray transparent  $\text{Si}_3\text{N}_4$  (Figs. 2.1c and 2.2). The ion dose to stop at the  $\text{Si}_3\text{N}_4$  is determined by dynamically checking the milling progress using the SEM in the dual beam SEM/FIB. The low energy of the  $\text{Ga}^+$  ions reduces sub-surface damage and therefore the annealing of the Au and the formation of hard grains (and, besides, also minimizes sub-surface damage of already deposited specimen on the other side of the membrane due to the reduced ion penetration depth). Hence, the determined milling dose is applicable to all Cr/Au multilayers grown in the same batch, facilitating the automation of the object hole fabrication. Focus and stigmator adjustments are not very critical for this process. If required, the  $\text{Si}_3\text{N}_4$  layer at the object hole can be thinned in this step to improve

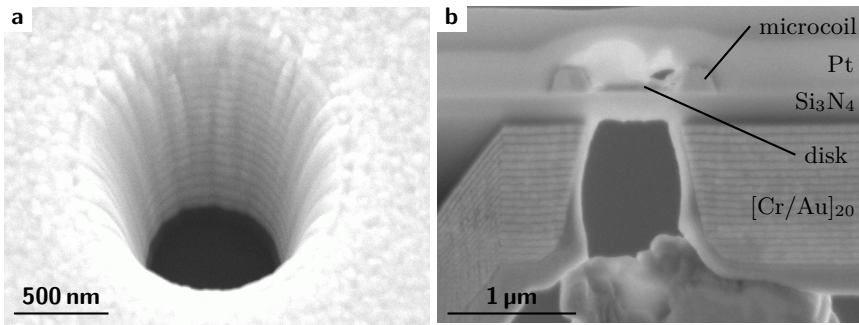


**Figure 2.2 | Scanning electron micrographs of the object hole milled into the Cr/Au layer.** (a) View under  $30^\circ$  with respect to the surface normal, showing the Cr/Au multilayer stack (Au appears bright, Cr gray, and  $\text{Si}_3\text{N}_4$  black). (b) Vertical cross section. The object hole is visible as an horizontal interruption of the periodic Cr/Au multilayers. A dust particle has fallen on the object hole before the preparation of the lamella.<sup>#</sup>

the aperture transmission. The thinning process can also be done with a high degree of reproducibility.<sup>#</sup>

The round shape of the object hole provides a scattering pattern that is most convenient for the hologram acquisition as well as for the reconstruction process. We find that for aperture diameters smaller than approximately 800 nm, holograms can be recorded without a beamstop for the direct beam, which significantly improves the image quality and enables fully automatic reconstructions. Even though multi-object holography has been successfully carried out in the past,<sup>87–90</sup> with its well known advantages, such as identical environments for all investigated specimens, we find that the signal from one object is noise for the reconstruction of the other objects and that the highest efficiency is reached when illuminating just one object aperture.<sup>#</sup>

### 2.3.3. Step 2: Alignment

After the preparation of the object aperture, Au markers are fabricated on the top side of each substrate at well-defined distances with respect to the object hole using EBL and standard lift-off techniques (Fig. 2.1d). Note that ultrasound (for instance for aiding the resist development and the lift-off process) cannot be used at any time as this would rupture the membrane. The alignment is achieved by first preparing dummy markers optically aligned with the membrane, and then measuring the coordinates of the object hole with respect to these markers using a pattern-recognition algorithm to automatically find the object holes. With the Vistec system, the alignment is reproducible and accurate to better than 20 nm despite the insulating substrates. However, it is important to keep the electron intensity at a minimum, e.g., by using a small beam current and by sufficient breaks between exposure steps. At lower electron energies, where charging becomes more

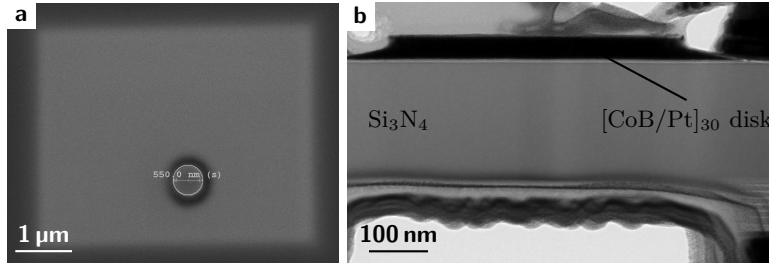


**Figure 2.3 | Magnetic disk.** (a) SEM view of the top side of the Si<sub>3</sub>N<sub>4</sub> membrane. The membrane is visible as a bright rectangle due to electron backscattering from the Au layer underneath. The object hole is visible as a dark circle around the magnetic disk. (b) TEM image of a vertical cross section, which is a zoom-in of the area shown in Fig. 2.2b.<sup>#</sup>

problematic, ESPACER<sup>TM</sup>300 conducting resist (by Showa Denko K. K.<sup>93</sup>) has proven successful in reducing charging.<sup>#</sup>

### 2.3.4. Step 3: Specimen

As an example, we discuss the fabrication process for samples used in the investigation of magnetic field-induced dynamics of magnetic domains.<sup>84</sup> The magnetic specimen is a disk-shaped element smaller than the field-of-view provided by the object aperture to ensure that the dynamics of the whole element is captured (Figs. 2.1e and 2.3). The disk is fabricated (i) by sputtering a continuous magnetic film on the flat side of the holography substrates, (ii) negative-tone EBL to produce a disk-shaped etch mask, and (iii) a subsequent neutralized Ar atom sputter-removal of the material everywhere apart from the disk. We use hydrogen silsesquioxane (HSQ) resist, enabling nanometer-resolution lithography and providing a sufficiently robust etch mask of SiO<sub>2</sub>, which is transparent to soft x-rays and does not need to be removed for imaging. It is important to protect the alignment markers throughout these steps. The means of marker protection must be adapted to the specifications of the lithography system that is employed in the succeeding steps: When using a Vistec machine, the distance of the alignment markers to the area of exposure is not critical for the alignment precision, and markers can be placed at the edge of the sample. In contrast, with the Raith systems, the alignment precision is significantly enhanced when the markers are present in the write field area, i.e., when the stage does not move after the marker detection. For this reason, we use a coarse mask, such as Kapton, to protect the markers from metal deposition when further patterning is performed with the Vistec machine, whereas lithographic lift-off masks are required when using the Raith systems. To protect the markers during the Ar milling, we expose the HSQ on top of the markers in all cases.<sup>#</sup>

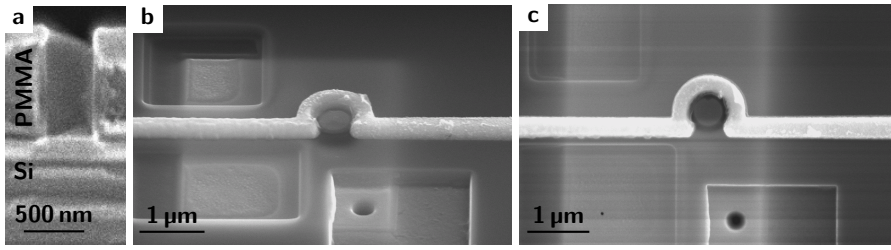


**Figure 2.4 | SEM images of the final fabrication steps.** (a) Cross section through a 330 nm wide line defining a mask in 750 nm thick PMMA for the Au microcoil deposition. The variation of the width of the line as a function of vertical position is negligible, i.e., the PMMA walls have no undercut. (b) Image of the final sample before preparation of the second reference. The sample is tilted by  $52^\circ$  with respect to the incident electron beam. The image shows the magnetic disk in the center, which is tightly surrounded by a Au microcoil. In this particular sample, three areas of  $\text{Si}_3\text{N}_4$  are removed to prepare the references where one reference has already been prepared with the cone on the top side (the side from which the image was taken). (c) Top-view of the same sample after the preparation of another reference from the bottom side.<sup>#</sup>

### 2.3.5. Step 4: Excitation

The next step is to prepare a microcoil for magnetic excitations wound tightly around the disk (Figs. 2.1f and 2.4). We use a Au wire with a cross section of  $300 \times 300 \text{ nm}^2$ , which results in a  $50 \Omega$  impedance against the Au ground on the back side of the membrane, as required for GHz microwave transmission. The wire dimensions take into account the thickness of the  $\text{Si}_3\text{N}_4$ . Outside the membrane area, the wire width is increased according to the local thickness of the Si wafer (which has a constant slope in the region that defines the membrane window), up to a width of  $170 \mu\text{m}$  on the bulk substrate. This ensures the  $50 \Omega$  impedance matching of the whole microstrip.<sup>#</sup>

The microcoil is fabricated in a lift-off process, where we use  $1 \mu\text{m}$  thick polymethylmethacrylate (PMMA) resist exposed via EBL with electron energies of 100 keV, and a 7 : 3 mixture of isopropanol and water for the development,<sup>94</sup> to achieve steep side walls in the resist (i.e., to avoid undercut), as shown in Fig. 2.4a. With such steep side walls, the position and the width of the microcoil are precisely defined and the coil can be prepared in close proximity to the magnetic disk. We note that a pre-exposure bake of the PMMA for 60 s at  $120^\circ\text{C}$  proved sufficient for our lithography, which is important for specimens that cannot withstand high temperatures. At low electron energies, optimal alignment precision requires the removal of the PMMA layer around the markers by electron exposure and development before the actual exposure of the microcoil. Furthermore, the inevitable undercut in the PMMA mask that is characteristic for low electron energies has to be considered in the exposure layout. Our specific microcoil has an inner diameter of 760 nm. It has been shown that such a coil is suitable to generate field pulses with approximately 100 ps rise time and 40 mT peak strength at its center.<sup>84#</sup>

### 2.3.6. Step 5: Reference holes

The reference holes are narrow cylinders milled through the entire material stack of  $\text{Si}_3\text{N}_4$  and  $\text{Cr}/\text{Au}$ . The  $\text{Si}_3\text{N}_4$  is removed with the FIB around each reference hole before milling to avoid problems when the ion beam hits the interface between (hard)  $\text{Si}_3\text{N}_4$  and (soft)  $\text{Au}$  (Figs. 2.1g and 2.4). The reference holes are then milled with a 30 keV  $\text{Ga}^+$  ion beam at 30 pA beam current focused to a spot size better than 20 % of the target reference hole diameter (practical value). In a first step, the  $\text{Cr}/\text{Au}$  is removed in a 500 nm wide and roughly 500 nm deep cone, and afterwards, a circular hole of the desired diameter (50 nm in our application) is milled through the remaining  $\text{Cr}/\text{Au}$  layers (Figs. 2.1h and 2.4). The usage of the highest ion energy leads to the best contrast in images taken with the ion beam, and thus allows for optimal beam adjustment and provides the smallest spot size. The cone reduces the aspect ratio of the reference tube, and allows for the sputter-removed material to leave the hole. Still, the high aspect ratio of the reference holes hinders the fabrication of holes with diameters near the spot size of the ion beam.<sup>#</sup>

## 2.4. Performance

Samples prepared according to the recipe presented before have successfully been used in a pump-probe dynamic imaging experiment published elsewhere.<sup>84</sup> Here, we discuss the efficiency of the design determined from these measurements. We obtain images of the magnetic state of our disk by x-ray holographic imaging using holograms taken with positive and with negative helicity photons at the Co  $\text{L}_3$  absorption edge (778 eV), as described in Ref. 78. Our specific magnetic material is  $\text{CoB}/\text{Pt}_{30}$ , which is optimized for pump-probe dynamic imaging,<sup>95</sup> in particular for Skyrmion dynamics.<sup>84</sup> An image of the magnetization component projected onto the photon propagation direction is reconstructed by an inverse Fourier transform of the difference of the holograms taken with positive and with negative helicity, utilizing the fact that this difference contains only the magnetic information due to the XMCD at the given photon energy. Here, our sample is mounted perpendicular to the incident beam, and we are sensitive to the thickness-integrated out-of-plane component of the magnetization. Holograms are acquired using a Princeton Instruments PI-MTE camera with  $2048 \times 2048$  pixel, operated at 1 MHz readout speed.<sup>#</sup>

The image reconstruction works reliably with a fully automatic script. This is possible because our design allows for the imaging without beamstop and therefore for an accurate automatic determination of the center of the image required by the Fourier transform. This automatic centering has not been reported for any other holographic sample design so far. Our script finds the center of the hologram

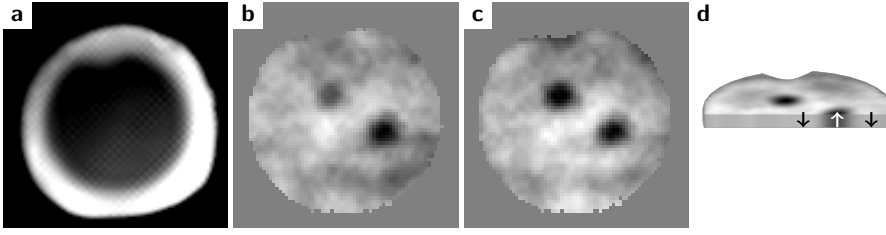


**Figure 2.5 | Holographic reconstructions of a magnetic state obtained with the presented sample design.** (a) Topography of the specimen, which is a 550 nm diameter disk with a notch at the top centered to the 800 nm diameter field of view defined by the object hole (white circle). (b) Reconstruction of the magnetic state from a difference hologram with  $6 \times 10^7$  photons per helicity, cropped to the disk area. The magnetization is pointing downwards (away from the reader) in the white regions, whereas it is pointing upwards in the black areas. The image shows a magnetic configuration with two bubble domains. (c) Reconstruction of the same state from  $1.3 \times 10^7$  photons per helicity. (d) Schematic cross section through the disk shown in (c), with the orientation of the magnetic domains depicted by arrows.<sup>#</sup>

with sub-pixel precision by searching for the maximum of the total number of counts in a circle with a 10 pixel radius and variable origin in a  $20 \times 20$  pixel area around the brightest pixel in the sum of all holograms. Furthermore, before the Fourier transform, two algorithms are applied to the difference hologram to improve the quality of the reconstructed image: (i) filtering of parasitic signals such as cosmic rays and dead pixels identified by their intensity deviating by more than 6 standard deviations from the average local intensity in a  $32 \times 32$  pixel environment, and (ii) zero padding of the hologram to double its original size. The magnetic disk is a small area in the transformed hologram, which is cropped using the topography image obtained by reconstructing the sum holograms from both helicities, see Fig. 2.5a. Finally, the complex phase is optimized for maximum contrast in the real part of the image. This real part yields the images of the magnetic domains (Figs. 2.5b and 2.5c), in our case showing that the magnetization is pointing predominantly downwards, apart from two circular areas, so-called bubble domains. The images shown in Figs. 2.5b and 2.5c are reconstructed from holograms taken with distinct integration times. We find that a total number of  $6 \times 10^7$  detected photons per helicity is required to obtain an image of the magnetic state, see Fig. 2.5b. These photons are inhomogeneously distributed across the camera chip, with the distribution being characteristic for the specimen and the mask geometry. With our particular mask design, the total number of  $6 \times 10^7$  photons corresponds to 2300 photons ( $1.5 \times 10^5$  camera counts) in the brightest pixel. Because the sensitivity of our camera becomes non-linear if more than  $3.5 \times 10^4$  counts are recorded in a single pixel, 4 camera readouts per helicity are required to obtain an image of the quality shown in Fig. 2.5b. The total acquisition time of a single image with our sample design and the presently available photon flux is less than 2 minutes plus the additional time for changing the helicity.<sup>#</sup>



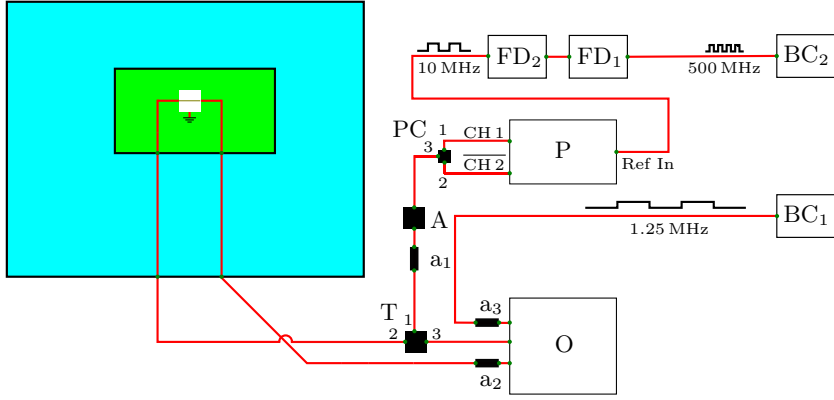


**Figure 2.6 | Electrical schematics for pump-probe FTH.** The blue rectangle symbolizes the vacuum chamber, and the green rectangle indicates the sample board. The sample itself is depicted as a white square with a thin yellow wire on top. The red lines denote high frequency cables with SMA connectors. The acronyms represent the following: *a* stands for attenuator, *T* for pick-off tee, *A* for amplifier, *O* for oscilloscope, *P* for pulse generator, *PC* for power combiner, *CH* for channel, *FD* for frequency divider, and *BC* for bunch clock. A more detailed discussion of the figure is provided in the text.

## 2.5. Pump-probe setup

The samples presented here are designed for microwave pump-x-ray probe holographic imaging at synchrotron light sources. Two steps are critical to enable such a pump-probe experiment: first, the repetition rate of the injected microwaves must match the repetition rate of the incident photon pulses exactly and, second, it is crucial to know the time at which a microwave should be injected in order to arrive simultaneously with the photons at the sample. In the following, we will discuss the electronic circuits with which we accomplish these tasks.

A schematic of the electrical circuit for the synchronized pulse injection is drawn in Fig. 2.6. We use a Picosecond Pulse Labs 12080 800 MHz pulse generator (*P* in Fig. 2.6) that has two individually programmable output channels, each with two SMA-type output connectors: one for the normal and one for the inverted signal. Each channel can create rectangular pulses with sub-100 ps rise time with up to 2 V bipolar amplitude and up to 800 MHz repetition rate. Both outputs provide adjustable time delays. The pulse generator has an internal 10 MHz clock, which can be replaced by an external clock signal (at Ref In). To ensure that the pulse generator injects pulses with the same repetition rate as that of the incident photon pulses (which is slightly less than 1.25 MHz in the single bunch mode of BESSY II), the 8-fold multiple of the synchrotron pulse repetition rate (which is slightly less than 10 MHz) is fed into the pulse generator as a 10 MHz clock signal. With respect to this external clock, a 1.25 MHz signal has the exact same repetition rate as the photon pulses.

To create such a 10 MHz signal from the synchrotron, we use the 400-fold single

bunch frequency (approximately 500 MHz), because such a signal is provided by the synchrotron (at bunch clock  $BC_2$ ) and because it is much easier to reduce the frequency of a signal than multiplying it. That is, we use frequency dividers ( $FD_1$  and  $FD_2$  in Fig. 2.6), where the first one ( $FD_1$ ) divides the frequency by 25, and the second one ( $FD_2$ ) divides by another factor 2. The reason for not using directly a division factor of 50 is that this would result in a rectangular pulse pattern with a duty cycle of 2 % ( $1/50$ ), whereas our setup with two frequency dividers provides the 50 % duty cycle signal expected by the pulse generator.

We can use this pulse generator to create bipolar rectangular pulses with variable amplitudes in both polarities. For this purpose, we use channel 1 (CH 1) of the pulse generator for the positive pulse and the inverted channel two ( $\overline{CH\ 2}$ ) for the negative pulse. The relative delay between the pulses is set to the duration of the first pulse, thus creating an uninterrupted succession of both pulse polarities, which is often useful because this pulse shape provides the strongest change of excitation at a given ohmic heat load. The signal from both outputs is combined using a power combiner (PC) that combines the input signals on connectors 1 and 2 in the output connector 3. The combined signal is amplified by 32 dB (power gain factor of 1600, voltage increase by a factor of 40) using a built-to-order Kuhne KU PA BB 5030A amplifier (A) with a band width of 10 MHz to 1500 MHz. To protect the amplifier against reflected signals, an attenuator of  $-3$  dB ( $a_1$ ) is mounted at its output. Any reflection will pass the attenuator twice and will thus be attenuated by  $-6$  dB.

Before being injected into the sample, part of the amplified signal is picked off to be monitored with a LeCroy WavePro 735ZI 3.5 GHz real time oscilloscope (O). This splitting of the signal is done using a built-to-order Kuhne KU DIV 0112 A-371 pick-off tee (T), which splits the input signal on connector 1 in two parts, one almost unperturbed (power reduced by  $-2$  dB) on output 2 and the other one attenuated by  $-20$  dB on output 3. The signal from output 3 is monitored on the oscilloscope, whereas the signal from output 2 is injected into the microcoil. Part of this pulse is transmitted and subsequently recorded with the oscilloscope (optionally attenuated at  $a_2$ ), another part is absorbed by heating the microcoil, and the rest is reflected and sent through the pick-off tee again with  $-20$  dB attenuation to the oscilloscope. The current transmitted through the microcoil can be calculated from the voltage of the transmitted signal recorded on the oscilloscope (if present, corrected by the damping of  $a_2$ ) divided by its  $50\ \Omega$  input impedance.

We now send bipolar pulses with a repetition rate synchronized to the incident photon pulses through the microcoil. The remaining challenge is to have both pulses simultaneously on the sample. For this purpose, we use the rising edge of the 1.25 MHz bunch clock signal ( $BC_1$ ) provided by the synchrotron as a reference time zero, i.e., we record this bunch clock signal on the oscilloscope (attenuated by  $-20$  dB (at  $a_3$ ) because its voltage is too large for the oscilloscope) and set its

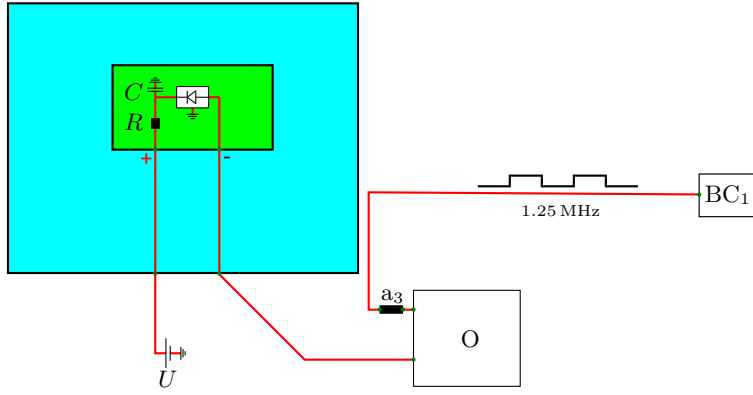


**Figure 2.7 | Electrical schematics for the time zero determination with an APD.** The blue rectangle symbolizes the vacuum chamber, and the green rectangle indicates the APD board. The APD itself is depicted as a white diode symbol on the APD board. On the positive contact side of the APD, a  $1\text{ M}\Omega$  resistor  $R$  and a  $1\text{ nF}$  capacitor  $C$  are integrated in the APD board. A source meter is used to supply a voltage of  $100\text{ V}$  on the positive input of the APD. The negative side is connected with cables of well-known length with the oscilloscope  $O$ . This oscilloscope is triggered by the  $1.25\text{ MHz}$  bunch clock signal  $BC_1$  provided by the synchrotron.

trigger to the respective channel. The temporal position of the photon pulse with respect to the same trigger is determined by mounting a Hamamatsu S9717-05K fast avalanche photo diode (APD) on the position at which the sample is during the measurement, and by using cables to transport the signal from the APD to the oscilloscope of precisely the same length as in the excitation scheme. The circuit used for this measurement is sketched in Fig. 2.7. One side of the APD is connected to the oscilloscope, which is triggered by the  $BC_1$  bunch clock signal. That is, this side is electrically on ground potential. The other side is lifted to  $100\text{ V}$ , and part of this potential drops on a  $1\text{ M}\Omega$  resistor placed in series before the APD. In this configuration, the diode is operated in reverse bias mode, i.e., the depletion zone is increased by the electric field gradient. The resistance of the diode is much larger than  $1\text{ M}\Omega$ , such that almost the whole  $100\text{ V}$  drop at the APD. A  $1\text{ nF}$  capacitor couples this side of the APD to ground; in the static case, however, this capacitor is insulating. As soon as a photon is absorbed in the diode, the situation changes significantly. The photons create free electrons that are accelerated in the external potential and create an avalanche of new charge carriers by collisions during their motion (hence the name APD). The capacitor acts as a sink for the (temporarily) generated charges. The holes are filled by a current from the oscilloscope, which is detected as a positive voltage peak. The avalanche stops because the voltage at the APD decreases immediately as the device becomes conducting (then most of the voltage drops at the  $1\text{ M}\Omega$  resistor). The signal decays in oscillations characteristic of the complicated RLC equivalent internal circuit of the diode.<sup>96</sup> The time of the photon event is reconstructed from the start of the pulse on the oscilloscope.

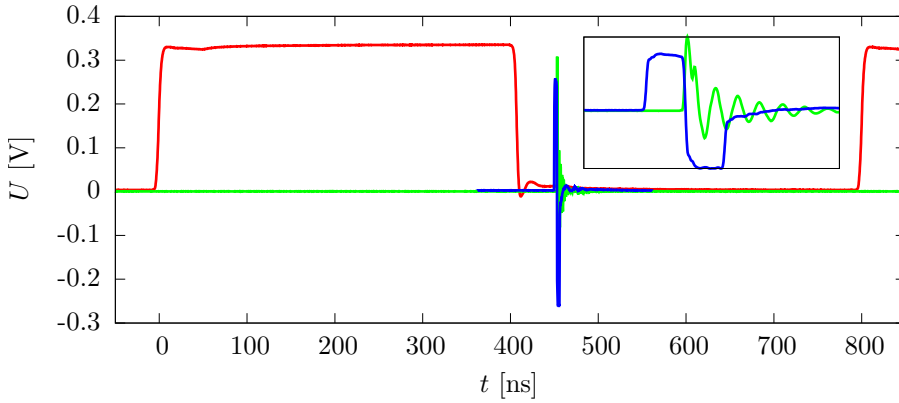


**Figure 2.8 | Signal measured with the oscilloscope.** The red line is the bunch clock  $BC_1$  that serves as a trigger for the oscilloscope. The 50 % level of the rising edge of this signal defines the time zero of the oscilloscope. The green line is the signal from the APD (multiplied by 5), and the blue line is the transmitted pulse (divided by 10). The latter two signals are plotted enlarged in the inset.

The signal recorded with the oscilloscope is plotted in Fig. 2.8. The red line depicts the 1.25 MHz bunch clock signal  $BC_1$ . The 50 % level of its raising edge defines the time zero of the oscilloscope. The photon pulse found on the APD (green line) starts at  $t = 452.7$  ns with respect to the oscilloscope trigger. After changing to the sample setup, the pulse send through the sample (blue line) arrives at the same time delay at the oscilloscope. The magnetic state is probed at the transition between positive and negative pulse.

## 2.6. Scanning transmission x-ray microscopy

Part of the results presented in this thesis have been obtained by using another x-ray imaging technique, namely scanning transmission x-ray microscopy (STXM). In STXM, the sample is scanned with high precision through a focused x-ray spot, and the total transmission is detected by a fast avalanche photo diode (APD), see Fig. 2.9. The readout of the diode is faster than the temporal separation  $\delta t$  of subsequent x-ray flashes (2 ns in the multi bunch mode at BESSY II). Typically, a configurable number of channels  $n$  is available for counting the transmitted photons. Provided the investigated sample is excited with an excitation of period  $\delta t n / m$  (with  $m, n$  coprime integers,  $m$  often called “magic number”), a movie of the response of the sample is directly obtained from the images collected in the  $n$  different channels. The frames of such a movie can be reshuffled in a pulse-chronological order, such that the dynamic response to the excitation is scanned in  $n$  temporal steps of  $\delta t / m$ . Ideally, the number of channels is coprime to the number of bunches in the synchrotron ring, such that the light from every bunch contributes equally to each channel and bunch fluctuations are averaged out. A

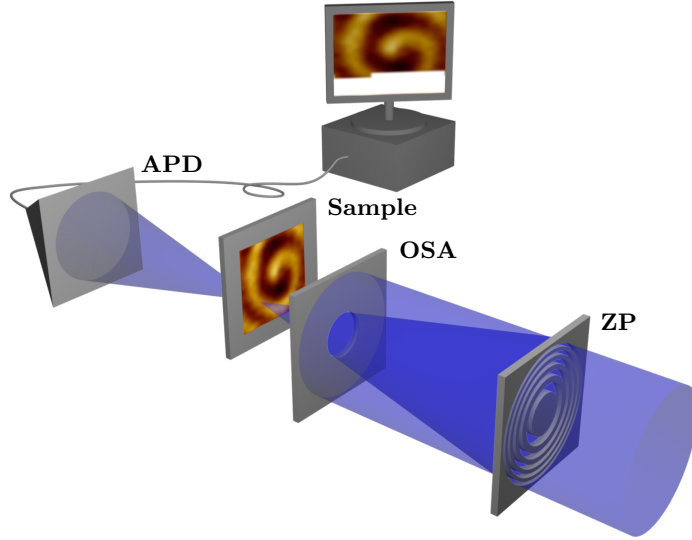


**Figure 2.9 | Schematic illustration of a scanning transmission x-ray microscope.** The incident beam is transmitted through a zone plate (ZP), which is made of alternating opaque and transparent rings to mimic a Bessel transmission function. The diffraction pattern of the transmitted beam is a point. Hence, the zone plate acts as a focusing lens. Due to the limited efficiency of the zone plate of typically 1 % to 10 %, the non-diffracted zero order light, as well as higher order diffractions, have to be blocked using an order selecting aperture (OSA). The sample is placed in the focus of the zone plate, and is scanned laterally to obtain an image pixel-by-pixel. The total transmission is recorded for every pixel using a super-fast avalanche photo diode (APD). The signal is analyzed by a computer.

full movie can be obtained in less than 15 min. In contrast to x-ray holography, STXM allows for zooming and real space translation of the field of view. That is, a large number of objects (magnetic disks in our case) can be investigated without changing samples. However, there are several drawbacks of this technique in view of pump-probe imaging of domain dynamics in PMA materials: (i) Spatial drift of the sample reduces the effective resolution and often renders the separation of the magnetic signal from topographic information (which is usually achieved by point-wise division of the transmission of positive and negative helicity x-rays) extremely difficult. The quality of the images obtained is typically worse than in x-ray holography. (ii) The APD is sensitive not only to the transmitted soft x-rays, but also to the GHz electromagnetic waves emitted by the excitation system. This so-called cross-talk can lead to a saturation of the detector when imaging during the excitation, in particular when using high frequency excitations as required for Skyrmion dynamics. (iii) The zone plate focusing the x-rays on the sample has to be very close to the sample surface (the distance is inversely proportional to the focus spot size), and at even closer distance, an order selecting aperture (OSA) has to be inserted to block all light apart from the first order focus (see Fig. 2.9). Due to the limited space available, strong static external magnetic fields

are difficult to provide. Furthermore, the magnet installed at the STXM used for our investigations was, for the duration of this thesis, not capable of providing pure out-of-plane fields (in fact, as measured with a Hall sensor, the field was almost at a  $45^\circ$  angle with respect to the sample normal). In-plane magnetic fields reduce the energy barrier for the nucleation of new domains, favoring this response to an excitation over domain wall propagation. As a consequence of the outlined problems, unambiguous pump-probe STXM images of domain dynamics in PMA materials, and in particular of Skyrmion dynamics, could not be obtained as part of this thesis. Still, STXM has proven extremely useful in the development of a new material suitable for dynamic imaging.

## 2.7. Conclusions

In conclusion, we presented a fabrication scheme for samples apt for pump-probe soft x-ray Fourier transform holography. The design has been optimized to acquire high resolution, high quality images in the low flux single bunch mode in a few minutes. With this acquisition speed, movies of magnetic dynamics with a sufficiently large number of frames can be recorded. Apart from the milling of the reference holes, which requires manual focus-tuning for every membrane, all fabrication steps can be automated. Hence, the process can be used in mass-production. Furthermore, our particular design facilitates the fully automatic reconstruction of the holograms, providing real-time access to the image information. Finally, we have provided an electric circuit to inject synchronized excitation pulses at a well-defined delay with respect to the x-ray photons at the sample position. We expect that our scheme will make time-resolved x-ray holographic imaging more accessible to the larger scientific community.<sup>#</sup>

# Chapter 3

## Material development and characterization

---

*We present magnetic domain states in a material configuration with high perpendicular magnetic anisotropy and particularly low magnetic pinning. This material, a [B-doped-Co]/Pt multilayer, exhibits a strong magnetic contrast in x-ray transmission experiments, making it apt for dynamic imaging with modern synchrotron techniques, providing high spatial and high temporal resolution simultaneously. By analyzing the static spin structures in nano-disks at variable external fields, we show that CoB/Pt multilayers exhibit low enough domain wall pinning to allow for the manipulation the domain pattern with weak stimuli and in particular for displacing domains and domain walls. We demonstrate in a proof-of-principle experiment using pump-probe x-ray holographic imaging that moderate magnetic fields can induce elastic and deterministic, and hence repeatable, small variations of the domain configuration in CoB/Pt multilayers. Such reproducibility is the key to perform high resolution imaging of the domain wall motion in order to gain insight to the details of the local magnetization dynamics.<sup>†</sup>*

---

### 3.1. Introduction

Materials with perpendicular magnetic anisotropy (PMA) are attracting significant scientific interest, motivated in particular by the technological relevance of this class of materials for applications in high bit-density hard disk storage devices,<sup>89</sup> current-driven domain wall shift registers with low critical current densities,<sup>97</sup> and programmable magnetic logic elements.<sup>98</sup> All these applications rely on the magnetic switching or controlled motion of magnetic domain walls at the nanometer length scale and picosecond time scale. The ongoing debate regarding the underlying physics of the domain dynamics in PMA systems, such as the origin, universality, magnitude, and even the sign<sup>99,100</sup> of the non-adiabatic spin transfer torque, as well as the eigenmodes of confined magnetic bubbles<sup>2</sup> (bubbles can be viewed as the out-of-plane analog to the magnetic vortex<sup>5,101</sup>), underline the need for direct imaging of the domain dynamics at the relevant sub-50 nm length

scale and sub-nanosecond time scale. Such high-resolution pump-probe dynamic imaging is well established for in-plane materials, in particular permalloy, with prominent experiments on, for instance, gyrating magnetic vortices<sup>58,102–104</sup> and domain wall motion.<sup>20,105</sup> For PMA materials, however, small inhomogeneities of the magnetic properties are amplified by the high perpendicular anisotropy to form considerable energy barriers for magnetic domain wall motion (pinning sites).<sup>89,106</sup> The influence of pinning is twofold and complementary on different length scales. While domain wall motion within a pinning potential is deterministic and elastic due to the well-defined restoring force of the potential, on length scales extending several pinning potential minima, stochastic thermal hopping over the energy barrier prevents elastic and in particular deterministic domain wall motion at small excitations and finite temperatures. That is, spin dynamics in high pinning materials is deterministic only at very small displacements (motion within the pinning potential) and in spin switching experiments at very high excitations (as strong pinning causes major hysteresis loop memory and reproducibility). In the latter case, changes are permanent (not elastic), and repeatability can be achieved only by a second pulse flipping back the spins and restoring the original configuration. To image domain wall motion, on the other hand, elasticity is needed on a length scale significantly larger than the spatial resolution, and thus shallow and sparsely distributed pinning sites are desirable. It has been demonstrated recently that pump-probe imaging of creep domain wall motion is possible, provided the domain wall can be reset to a well-defined starting position after every excitation, which, for instance, can be realized by using an artificial energy barrier.<sup>107</sup> However, in this experiment, the stochastic motion during the excitation effectively reduces the time resolution, leading to uncertainties in the nanosecond regime. For numerous applications and basic science studies, e.g., the observation of gyrating bubbles, it is desirable that the domain wall motion is deterministic on the sub-nanosecond time scale and elastic, i.e., that the system returns to the initial configuration when no external stimulus is present. The availability of a suitable, low-pinning PMA material system is thus pivotal in this context.<sup>†</sup>

Here we use x-ray imaging to determine the magnetic states. This is so far the only approach combining high spatial and high temporal resolution that allows for the imaging of magnetic domain dynamics in a pump-probe scheme. X-ray holographic imaging<sup>78</sup> in a transmission geometry is ideally suited as this technique is intrinsically drift-free and hence allows for the reliable detection of changes in the domain pattern even down to a few nanometers. However, x-ray-transmission-based dynamic imaging entails several constraints to the sample under investigation. First, the total thickness of the magnetic material has to be sufficient to provide reasonable magnetic contrast through the x-ray magnetic circular dichroism (XMCD).<sup>69</sup> Specifically, imaging in a transmission geometry currently requires several nanometers of magnetic material. Materials with PMA, which can be pre-



pared with the desired thickness on amorphous  $\text{Si}_3\text{N}_4$  membranes, are, for instance, multilayers of transition metals, such as Co/Pt or Co/Pd. These materials have been commonly used in a wide range of experiments<sup>89,98,108–112</sup> and are very well characterized.<sup>42,106,113–117</sup> Second, the pump-probe scheme relies on a deterministic and elastic response of the magnetic domains and domain walls to driving forces of up to GHz repetition rates. This requires a material with particularly low pinning to provide the high repeatability of the domain wall motion, which is also of key importance for applications.<sup>†</sup>

In this chapter we present a perpendicular magnetic material configuration for deterministic domain wall motion based on B-doped Co/Pt multilayers. In this material a significant reduction of the domain wall pinning has been found using quasi-static measurement techniques on films with sub-nanometer Co thickness.<sup>50,118</sup> For x-ray-transmission-based imaging, however, we need a minimum total thickness of a few nanometers of magnetic material. As the PMA in non-epitaxial Co/Pt arises from the Co/Pt interface interaction,<sup>43</sup> a natural way to retain the magnetic properties in a few nanometers thick configuration is to use multilayer stacks. Using x-ray holographic imaging of nano-patterned disks under statically applied external magnetic fields, we show that the pinning strength in our developed CoB/Pt multilayer configuration is sufficiently low and can enable repetitive pump-probe dynamic imaging. We demonstrate the repeatability in a pump-probe experiment, showing that we can use the material to image domain dynamics with sub-50 nm spatial resolution and sub-nanosecond time resolution.<sup>†</sup>

## 3.2. Sample growth and material characterization

Our B-doped magnetic multilayer is material CoB/Pt<sub>40</sub><sup>1</sup> grown on a  $\text{Si}_3\text{N}_4$  membrane where a holographic mask with an 800 nm diameter object hole has been prepared by focused ion beam milling in a 1.5  $\mu\text{m}$  thick gold film on the back side before deposition. The magnetic film was grown using DC magnetron sputtering at a chamber base pressure of  $3 \times 10^{-8}$  mbar. The Co<sub>68</sub>B<sub>32</sub> layers were grown at an Ar pressure of  $1 \times 10^{-2}$  mbar and a DC sputtering power of 20 W, while for the Pt layers an Ar pressure of  $3 \times 10^{-3}$  mbar at 60 W was used. The film was patterned after deposition into a 750 nm diameter disk centered to the object hole using electron beam lithography (EBL) and Ar ion milling. Finally, a 65 nm diameter reference hole was prepared adjacent to the object hole, yielding a resolution of 45(10) nm.<sup>119</sup> To compare the magnetic properties, we investigate nanostructures of a representative transition metal multilayer stack Co/Pd<sub>50</sub>. The material is grown on a  $\text{Si}_3\text{N}_4$  membrane and patterned into a 600 nm diameter disk by EBL and lift-off. The holographic mask is fabricated on a separate membrane to define

<sup>†</sup>The material names used here are abbreviations. The full material compositions are listed on page xvi.

a 2  $\mu\text{m}$  object hole and an adjacent 50 nm reference hole in a 900 nm thick gold film, yielding a resolution of approximately 35(10) nm. The mask is aligned to the magnetic disk using piezo stages.<sup>86</sup> This approach requires a special image reconstruction procedure to achieve optimal spatial resolution due to the finite distance between sample and mask (11  $\mu\text{m}$  in our case).<sup>81</sup> The holographic imaging was performed at the UE-52 SGM beamline at the BESSY II synchrotron in Berlin using circularly polarized photons with energy tuned to the Co  $L_3$  absorption edge (778 eV), employing XMCD to obtain magnetic contrast.<sup>†</sup>

Further experiments were performed to characterize both the conventional Co/Pt and Co/Pd multilayers as well as our optimized CoB/Pt material. The magnetic states of disk shaped elements were investigated as a function of disk diameter, material composition, sample fabrication techniques, and temperature treatment. Specifically, in addition to material Co/Pd<sub>50</sub>, disks of materials Co/Pt<sub>6</sub> and Co/Pd<sub>8</sub> were imaged. These materials were sputter-deposited at a chamber base pressure of  $2.8 \times 10^{-6}$  mbar and an Ar gas pressure of  $2 \times 10^{-3}$  mbar. Material CoB/Pt<sub>30</sub> was investigated as an alternative B-doped configuration in addition to material CoB/Pt<sub>40</sub>, and equally low magnetic pinning was found. The configuration CoB/Pt<sub>30</sub> has been chosen for subsequent time resolved experiments as it requires less efforts for the preparation (the sputtering chamber uses manual shuttling, which becomes time-consuming when using several tens of multilayers). Materials Co/Pd<sub>50</sub>, Co/Pt<sub>6</sub>, and Co/Pd<sub>8</sub> were patterned by lift-off techniques, whereas materials CoB/Pt<sub>30</sub> and CoB/Pt<sub>40</sub> were shaped by Ar milling. For dynamical imaging, 5.5  $\mu\text{m}$  wide electrical transmission lines made of Cr(5)/Au(50) were fabricated by lift-off techniques onto the samples with materials Co/Pt<sub>6</sub> and Co/Pd<sub>8</sub>, involving high temperature exposures of more than 180 °C for several minutes. In contrast, the transmission lines on the samples with the B-doped materials CoB/Pt<sub>30</sub> and CoB/Pt<sub>40</sub> were 300 nm wide Cr(5)/Au(300) wires, and the temperature was kept below 120 °C throughout the whole process. The imaging of the magnetic states has been carried out using STXM and x-ray holography. STXM measurements were performed at the MAXYMUS end station at BESSY II, using, as in holography, the XMCD contrast of circularly polarized photons at the Co  $L_3$  absorption edge.

From superconducting quantum interference device (SQUID) measurements on a continuous CoB/Pt multilayer film with the exact same composition as material CoB/Pt<sub>40</sub>, we obtain a saturation magnetization of  $M_s = 1.24(3) \times 10^6$  A/m (when normalized to the total thickness of the magnetic CoB), and a hard axis saturation field of  $\mu_0 H_k = 0.34(5)$  T corresponding to a total (effective) uniaxial magnetic anisotropy of  $K_{u,\text{eff}} = 2.1(3) \times 10^5$  J/m<sup>3</sup>. Here  $K_{u,\text{eff}} > 0$  defines a preferred out-of-plane alignment of magnetic moments. In a single layer configuration (Pt(4)/Co<sub>68</sub>B<sub>32</sub>(0.6)/Pt(2)), similar values of  $M_s = 1.03 \times 10^6$  A/m and  $K_{u,\text{eff}} = 3.2 \times 10^5$  J/m<sup>3</sup> have been found before.<sup>50,118</sup> To calculate the crys-

tal field uniaxial anisotropy constant  $K_u$ , we make use of the analytic relation  $\mathbf{H} = \frac{\partial F}{\mu_0 \partial \mathbf{M}}$  between the magnetic field  $\mathbf{H}$  and the magnetization  $\mathbf{M}$  through the free energy density  $F$ , which holds if the system is in thermodynamic equilibrium.<sup>120</sup> In the absence of any further knowledge of the magnetization reversal mechanism, the equilibrium magnetization can be approximated by the average of both hysteresis branches, with the difference giving a reasonable estimate for the  $2\sigma$  confidence interval. The free energy density is a potential, for which we can hence choose a constant offset such that the free energy density of the in-plane saturated state is  $F_{s,\text{ip}} = 0$ . Bringing the system from in-plane to out-of-plane saturation costs demagnetization energy and yields anisotropy energy. The free energy density of the out-of-plane saturated state is hence  $F_{s,\text{oop}} = \mu_0 M_s^2/2 - K_u$ . The remanent (demagnetized) state shows complex domains, which makes the corresponding free energy density  $F_0$  difficult to calculate. Here, however, we only use that the value  $F_0$  is unique and therefore equal for the in-plane and the out-of-plane loop. The energy differences  $F_{s,\text{oop}} - F_0$  and  $F_{s,\text{ip}} - F_0$  can be determined by calculating the saturation energies  $E_{s,\text{oop}}$  and  $E_{s,\text{ip}}$ , respectively, from the measured hysteresis loops.<sup>120</sup> Combining these considerations, we arrive at  $K_u = \mu_0 M_s^2/2 - E_{s,\text{oop}} + E_{s,\text{ip}}$ . For our material configuration, we obtain a value of  $K_u = 1.01(5) \times 10^6 \text{ J/m}^3$ , corresponding to a quality factor of  $Q = 1.05(8)$ . With these properties, our material is comparable to typical Co/Pt or Co/Pd multilayers,<sup>42,106,113–116</sup> and in contrast to other low-pinning materials such as permalloy, it belongs to the class of high-anisotropy materials.<sup>†</sup>

For the material CoB/Pt<sub>30</sub>, we obtain similar values of  $M_s = 1.19(3) \times 10^6 \text{ A/m}$ ,  $K_{u,\text{eff}} = 1.58(18) \times 10^5 \text{ J/m}^3$ ,  $K_u = 7.7(5) \times 10^5 \text{ J/m}^3$ , and  $Q = 0.87(6)$ . Furthermore, from a small angle x-ray scattering pattern of a continuous film of material CoB/Pt<sub>30</sub>, magnetized in a domain state of (roughly) parallel stripes, we determine the domain width  $\zeta$  with its statistical standard deviation  $\chi$  and the domain wall parameter  $\Delta_0$ , from which we derive the exchange stiffness  $A$  through the identity  $A = \Delta_0^2 K_{u,\text{eff}}$  (see chapter 1.3 for a theoretical background).<sup>121</sup> The azimuthally integrated scattering intensity  $I(q)$  is plotted on a logarithmic scale in Fig. 3.1 as a function of wave vector transfer  $q$  of the scattered photons. Three maxima can be identified, corresponding to the first, third, and fifth Bragg reflex of the stripe domain phase. The corresponding SAXS pattern, which is presented as an inset in Fig. 3.1, has been recorded in two steps. In the first image the central beam is blocked with a circular beam stop; due to the limited dynamic range of the camera, only the first and third order peaks are visible in this image. To detect the fifth order peak, a large diode in front of the camera was used to block the intense first order peak. Given the geometry of this diode, only a small part around one of the third and fifth order peaks has been illuminated. The radial integration is carried out in both images independently, and the resulting spectra are combined at the maximum of the third order peak.

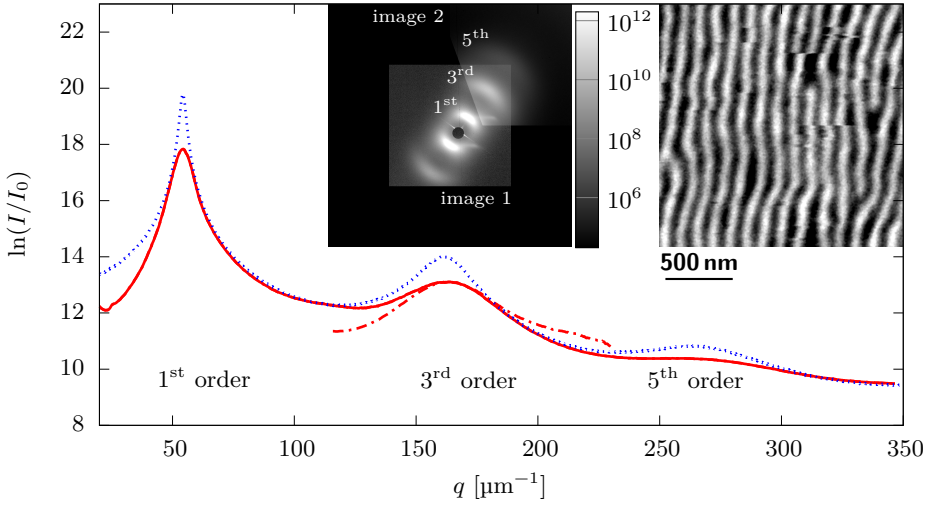


**Figure 3.1 | SAXS spectrum of material CoB/Pt<sub>30</sub> in the stripe domain phase.** The spectrum shows the azimuthally integrated scattered intensity  $I$  versus the wave vector transfer of the scattered photons  $q$  combined from two images with distinct dynamic range at the third order peak (on a logarithmic scale, solid red line). The dashed red lines show how the spectra from the single images continue to evolve. The measured spectrum is compared with the squared Fourier transform of a simulated stripe domain pattern (dotted blue line). The insets show the combination of both images embedded in the full camera chip on a logarithmic intensity scale (left) and a magnetic force micrograph of the stripe domain pattern (right).

The relative heights of the peaks, their positions, and the slope of the background are characteristic for the parameters  $\zeta$ ,  $\chi$ , and  $\Delta_0$ . We extract these parameters by comparing the measured spectrum with a squared Fourier transform of a computed random one-dimensional domain pattern  $M_z(x)$  with specified statistical parameters  $\zeta$ ,  $\chi$ , and  $\Delta_0$ . We find that the domain wall width mainly affects the slope of the background, whereas  $\chi$  has a large impact on the relative height of the peaks and on the distance between first and third order reflex. This clear signature of the parameters allows us to determine at least the domain width and its variation from the peak positions with high precision despite the overall poor agreement between the measurement and the simulation shown in Fig. 3.1. The extraction of the domain wall width parameter is less accurate. The discrepancy between the measurement and the model most likely originates from the 1D approximation of the model. In the 2D SAXS images a ring-shaped scattering pattern is visible. Even though this ring is much weaker than the Bragg spots of the stripe phase, they still indicate that the stripes are not perfectly straight but rather have some characteristic periodicity in the direction perpendicular to the stripes as well. At least two problems arise from this two-dimensionality. First, in the measurement of the fifth order peak, we select the stripe domain peak only, and mask the ring contribution. It seems therefore reasonable that the fifth order peak is weaker in the measured spectrum than in the simulations. And second, the

2D domain pattern is much more complex and three parameters are not sufficient to provide an accurate model. A 2D model, however, requires tremendous computing power and considerable code optimization to obtain results on acceptable time scales, and even if we would use a 2D model, the complexity would make it extremely difficult to extract the relevant quantities. That said, from our simple model, we obtain  $\zeta = 57.8(8) \text{ nm}$ ,  $\chi = 6.35(10) \text{ nm}$ ,  $\Delta_0 = 11(2) \text{ nm}$ , and hence  $A = 23(8) \times 10^{-12} \text{ J/m}$ . As expected, the exchange stiffness is slightly reduced compared to the value of pure Co due to the mixture with non-magnetic B.<sup>122</sup>

### 3.3. Static properties of Co/Pd and Co/Pt nanostructures

In Fig. 3.2 we present static magnetic images of a Co/Pd<sub>50</sub> disk at various uniformly applied external magnetic fields, and based on them we analyze the magnetic behavior of nanostructures from this material. Due to the inhomogeneity of the field and the hysteresis of the electro-magnet, the field values given in the following are approximate, with an error of 6 mT+10% of the actual value. We first image the domain configuration at zero applied field in Fig. 3.2a. Subsequently, a downward-oriented magnetic field of 100 mT is applied, see Fig. 3.2b. After apparent saturation at 200 mT (not shown), the field is reduced to zero again (Fig. 3.2c). Immediately afterwards, 100 mT are applied in the downward direction again, see Fig. 3.2d, where a magnetic bubble-like domain is isolated.<sup>123</sup> From the imbalance of black and white domains at zero field, we can deduce a considerable remanent magnetization of the sample. The observed domains show, both at remanence and at applied fields, a large variation in width and shape. Moreover, the shape of the domains is not commensurate with the disk geometry. The irregularity is present at the edges of the disk as well as in the center. Note that the spin configuration in Fig. 3.2c largely resembles that in Fig. 3.2a, only with inverted contrast signaling the reversal of the magnetic moments. This reversal of magnetic moments as well as the substantially different intermediate state in Fig. 3.2b excludes insufficient saturation as an explanation for the similarity (as argued in Ref. 113). Rather, our observations point to the presence of considerable pinning sites distributed all over the sample. The pinning is usually attributed to local variations in the anisotropy. It has been reported in Refs. 89 and 106 that this variation could be explained by the different orientation of crystal grains in the polycrystalline Co. The presence of strong pinning sites as found in our Co/Pd material is highly desirable for applications in data storage devices to stabilize the domain configuration against external perturbations, and the reproducibility of the remanent domain configuration could be used to investigate, for instance, the switching dynamics induced by very strong excitations. For the specific purpose

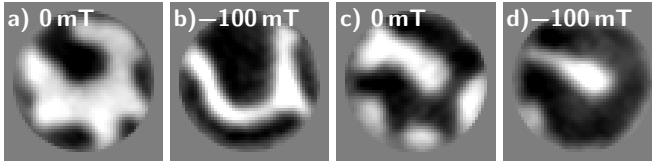


**Figure 3.2 | Magnetic domain states in Co/Pd.** Evolution of the magnetic domain pattern in a 600 nm diameter Co/Pd disk during application of a uniform static external out-of-plane field of varying strength. White indicates magnetization pointing up (positive field direction) and black indicates magnetization pointing down. Between (b) and (c), the sample was saturated with a magnetic field of  $-200$  mT.<sup>†</sup>

of pump-probe dynamic imaging of domain wall motion, however, a system with significantly weaker pinning centers and a reduced pinning density is required.<sup>†</sup>

To provide a statistically more significant data set for our conclusions on conventional Co/Pt and Co/Pd, we perform STXM imaging of several hundred disks of variable diameter and material composition (materials Co/Pd<sub>50</sub>, Co/Pt<sub>6</sub>, and Co/Pd<sub>8</sub>). All disks of material Co/Pd<sub>8</sub> are single domain, and the material has not been further investigated. A collection of remanent domain configurations in materials Co/Pd<sub>50</sub>, Co/Pt<sub>6</sub>, and, for comparison, material CoB/Pt<sub>30</sub>, is presented in Fig. 3.3. An overview of possible remanent domain patterns in Co/Pt (material Co/Pt<sub>6</sub>) is provided in Fig. 3.3a, showing the magnetic states of a set of disks with  $2\mu\text{m}$  and  $2.25\mu\text{m}$  diameter. A Au transmission line is running horizontally on top of some of the disks, covering them about half. In all of these disks, domains of irregular shape and varying width can be identified. Before the imaging, a rapid succession of 1000 pulses (pulse train), each with 2 ns duration and a current density of  $9(2) \times 10^{11}$  A/m<sup>2</sup>, followed by 1000 pulses of  $6(1) \times 10^{11}$  A/m<sup>2</sup> and reverse polarity, has been injected to the transmission line. The error for current density through the Au transmission line comes predominantly from the 20 % uncertainty of the thickness of the Au, i.e., it is of systematic nature. The orientation of the last pulse was such that its magnetic field favored the white domains in the bottom row and the black domains in the top row. Even though the pulses have been switched off in Fig. 3.3a, the white domains are still dominating the bottom row, while the disks in the top row show more black domains. A significant number of disks shows bubble domains, but only a few of them are round. Most disks that are further away from the transmission line are in the single domain state.

The state after another pair of pulse trains of the same shape as before is presented in Fig. 3.3b. The domain pattern was modified considerably in some disks, whereas in others it remains unchanged. We expect the stripe domains to orient preferably in the direction transverse to the wire, i.e., along the the in-plane component of the magnetic field of the transmission line, which is strongest below the wire. In contrast, there is a clear preference for a domain alignment parallel to the wire. Also the changes from Figs. 3.3a to 3.3b show a slight tendency in favor

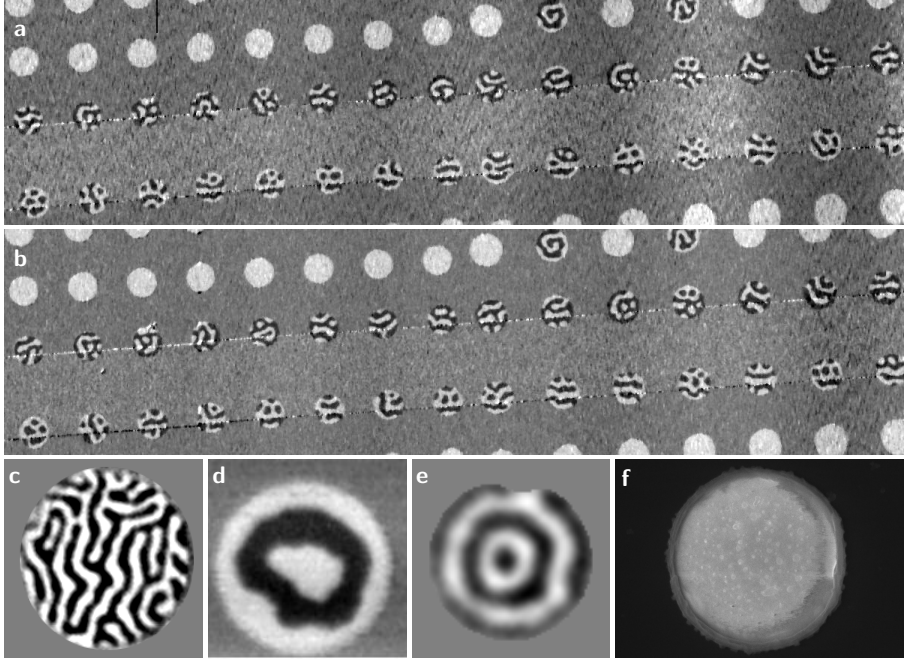


**Figure 3.3 | Remanent domain configurations in conventional Co/Pt and Co/Pd, and in CoB/Pt.** (a) STXM overview graph of Co/Pt<sub>6</sub> disks of 2  $\mu\text{m}$  and 2.25  $\mu\text{m}$  diameter. The two horizontal lines (one black and one white) are the edges of a Au transmission line running horizontally on top of the disks. The graph is a pixel-wise division of one image taken with positive by one taken with negative helicity photons, eliminating all non-magnetic signals. Residual features are characteristics of uncompensated drift between the two images. (b) The same sample area after sending a current pulse through the transmission line. (c) X-ray holography image of a quasi-continuous film of Co/Pd<sub>50</sub>. The disk-shaped element is larger than the 2  $\mu\text{m}$  diameter field of view. (d) STXM graph of a 2  $\mu\text{m}$  diameter Co/Pt<sub>6</sub> disk, showing a three-ring state (which can be seen as a higher order bubble<sup>5</sup>). (e) A very similar state (with 5 rings) in the 550 nm diameter CoB/Pt<sub>30</sub> disk investigated in chapter 4. (f) SEM image of a 2  $\mu\text{m}$  diameter Co/Pd<sub>50</sub> disk.

of a domain alignment parallel to the wire.

To investigate how significant edge the roughness is for pinning in material Co/Pd<sub>50</sub>, we image the domain pattern in a quasi-continuous film on the same sample presented in Fig. 3.2, as shown in Fig. 3.3c. In line with our previous observations in Fig. 3.2, the domains show a broad distribution of widths. Similarly, the three-ring state found in a 2  $\mu\text{m}$  diameter disk of material Co/Pt<sub>6</sub> (Fig. 3.3d), despite being roughly adapted to the circular shape of the disk, displays considerable irregularities. For instance, the bubble in the center is not round, and the black domain has a very rough domain wall in the bottom part. This behavior is in contrast to low-pinning CoB/Pt, where the domains are circular and of constant width, as shown for a 550 nm diameter disk in Fig. 3.3e. Only near the edges of the disk, significant domain roughness is observed. However, we have to keep in mind the different sizes of the disks shown in Figs. 3.3d and 3.3e. Thus, in Fig. 3.3e,

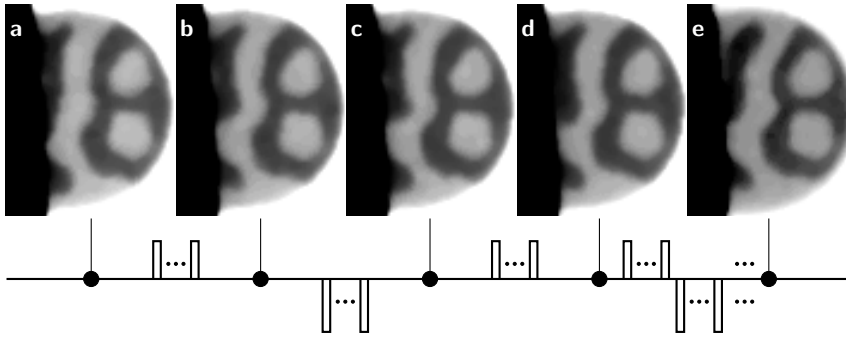


**Figure 3.4 | Quasi-static excitation of a Co/Pt disk.** The images show the static domain configuration in a  $2.25\text{ }\mu\text{m}$  diameter Co/Pt (material Co/Pt<sub>6</sub>) disk that is partially covered by a Au transmission line (black bar on the left of each image). In between the images, a rapid succession (pulse train) of 500 positive or negative pulses has been sent through the transmission line, schematically indicated by the time line in the bottom. Between (d) and (e), 13 pulse trains of each polarity were injected.

our spatial resolution is not sufficient to investigate and draw conclusions from the detailed shape of the domain walls. Our results indicate that the pinning observed in Co/Pt and Co/Pd here is not confined to the edge of the sample, and therefore not related to the fabrication process. In contrast, an SEM image of a  $2\text{ }\mu\text{m}$  diameter disk of material Co/Pd<sub>50</sub> (Fig. 3.3f) shows a large surface roughness of the magnetic material all over the disk. To what extent this roughness can be attributed to the patterning (and not to the material growth) remains to be investigated.

We take a closer look at a  $2.25\text{ }\mu\text{m}$  diameter Co/Pt<sub>6</sub> disk that is partially covered by a Au transmission line, see Fig. 3.4. The transmission line is used to excite the domain pattern with an Oersted field pulse. From our previous static study, we expect the changes to be permanent, i.e., that the magnetic state after a excitation will be an excited state and not the original configuration. Here we test if we can restore the original configuration with the help of another weaker excitation with reversed polarity, using the same bipolar pulse train scheme as above, but with 500 pulses per pulse train. In Fig. 3.4 we show a sequence of images with a specified excitation applied between two adjacent images. All images show slightly different domain patterns. Changes are stronger near the transmission line than farther away. There is no clear direction of the evolution of the domain configuration, i.e., all the observe configurations are energetically almost degenerate and there is little hope that the domain pattern evolves into a unique ground state that could serve as an initial configuration for pump-probe excitations.

Our observations are consistent with the conclusions drawn from Fig. 3.2. All of our Co/Pt and Co/Pd samples show considerable pinning both at the edges as well as far away from fabrication artifacts. The pinning manifests itself in irregular domains with rough domain walls and strongly varying widths. The considerable





**Figure 3.5 | Temperature effect in Co/Pt material Co/Pt<sub>6</sub>** (a) STXM graph of another area of the same sample shown in Fig. 3.3a. The black line is the left border of the transmission line. (b) The same sample area after sending current pulses through the wire. The magnetic contrast has vanished completely. (c) Another area of the same sample. Here, only the material underneath the curved transmission line shows out-of-plane magnetic contrast, even in the disk that is partially covered by it.

remanent magnetization demonstrates that stray fields are insufficient to drive this material to the lowest energy state after an excitation. (The zero net magnetization configuration should be lower in energy than the observed remanent states because it can be realized with the same total domain wall length and through a continuous deformation.) The domain configurations after an excitation are unpredictably different from the original patterns. Field pulses of the strength used here are able to induce small but unambiguous changes in the domain configuration, most prominently near the Au wire. This is the regime where we could expect to find reproducible dynamics, because the number of energetically degenerate configurations accessible from an excited state increases with the excitation amplitude. Reproducible dynamics can be expected only when such ambiguities are absent along the excitation path. However, despite the ideal conditions, we observe slightly different patterns after every pulse train. That is, even with the restoring pulse, it is not possible to recover a particular initial configuration deterministically. The reason for this is the dense distribution of pinning centers that can be surpassed by the combined action of pulse excitation and thermal hopping. The latter term introduces a stochastic element to the dynamics, preventing the repetition of the exact same experiment and, therefore, the dynamic imaging in a pump-probe scheme. Such a pump-probe experiment, for instance the one presented in chapter 4, rather requires a shallow but strong pinning potential. That is, it requires a potential that allows the motion of the quasiparticle domain on a detectable length scale while ensuring the relaxation to the initial configuration by being strong enough to avoid any thermally activated escape from the potential well.

We finally point to a peculiar phenomenon that has been observed in the sample shown in Fig. 3.3a. In Fig. 3.3a all disks that touch the transmission line are in a worm domain state (before sending any pulses through the wire), whereas at a few micrometer distance, most of them show single domain configurations. A few hundred micrometers away, however, we observe the exact opposite arrangement: below the transmission line, all disks are in the single domain state, whereas ad-

jacent to it, they show normal worm domains, see Fig. 3.5a. Here, the magnetic signal suddenly disappears after sending current pulses through the transmission line, see Fig. 3.5b. Even more peculiar, in one small area of the same sample, the disks show out-of-plane magnetic contrast only below the Au wire (again before sending pulses through), see Fig. 3.5c. Even disks that are partially covered by the transmission line show magnetic contrast only in the part that is under the Au. These are first hints to the sensitivity of the material towards heating (during fabrication and during the pulse transmission). During sample fabrication, all Co/Pt and Co/Pd disks were exposed to high temperatures, for instance to 180 °C for at least 60 s in the traditional lift-off process for the fabrication of the Au transmission lines employing polymethylmethacrylate (PMMA), and potentially to even higher temperatures during the thermal evaporation of the Cr/Au material for the transmission line. The effect of the heat carried by the evaporated Cr and Au atoms is evidenced by the different magnetic properties of the disks below and besides the transmission line, such as shown in Fig. 3.3b, which we attribute to the inhomogeneous annealing of the Co/Pt multilayer during the material deposition. Why this has led to the inverse effect of reduction of magnetic contrast in the elements adjacent to the wire cannot be answered by our experiments. Another demonstration of the effect of heating is the *in situ* loss of magnetic contrast in disks adjacent to the wire after the injection of long pulses. Here, the sample is not exposed to oxygen, and oxidation can be excluded to cause this effect.

To conclude this part, we have shown that the investigated Co/Pd and Co/Pt multilayers, when nanostructured by lift-off lithography, are not suitable for pump-probe imaging of Skyrmion dynamics because of their large density of relatively strong pinning sites. Furthermore, we have demonstrated that the magnetic properties of the multilayers are very sensitive to heat, requiring great care during the sample fabrication as well as during the application of the pulse excitation. Some improvements incorporated in the CoB/Pt disk investigated in chapter 4 include using Ar milling instead of lift-off, pre-exposure baking of the PMMA for only 15 s at 180 °C (even better, as discussed in chapter 2, baking the PMMA at only 120 °C for 60 s), reducing the lateral size of Si<sub>3</sub>N<sub>4</sub> membrane, on which the disks are fabricated, to a minimum size of a few square micrometer to facilitate the heat transport into the bulk Si substrate, and using pulse duty cycles of less than 1 %. With these improvements, Co/Pd and Co/Pt multilayers might be suitable for dynamic imaging as well, and investigations in this direction are motivated by the better magnetic contrast of these materials compared to CoB/Pt.

### 3.4. Static properties of CoB/Pt nanostructures

In Fig. 3.6 we present an out-of-plane hysteresis loop of a continuous CoB/Pt film together with a selection of images of a 750 nm diameter CoB/Pt multilayer disk

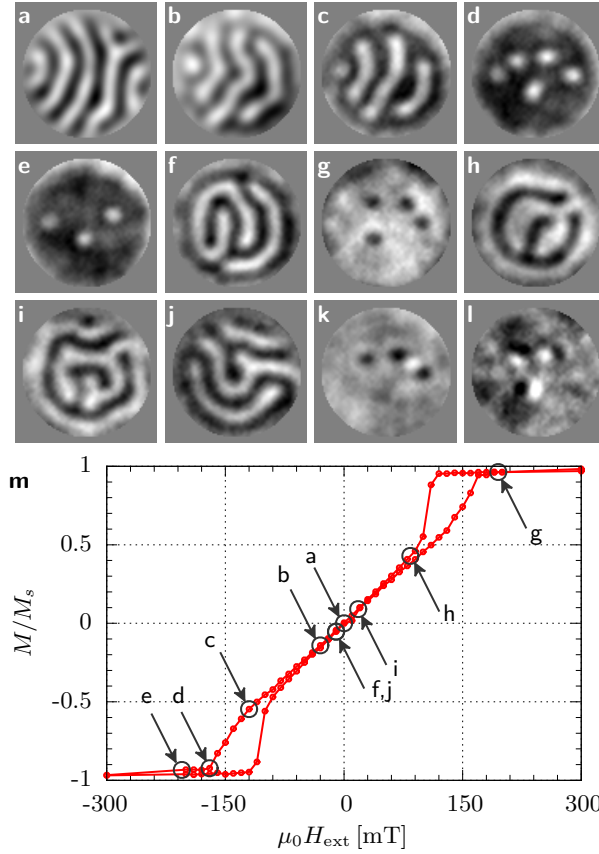


**Figure 3.6 | Static domain configurations of CoB/Pt.** (a–l) Selection of magnetization images of a 750 nm diameter CoB/Pt disk at various out-of-plane magnetic field steps, where white indicates magnetization pointing up (positive field direction) and black indicates magnetization pointing down. (a) shows the virgin state after deposition. Between (a) and (b) the sample experienced a field of 65 mT. Between (e) and (f), between (g) and (h), and between (i) and (j) the sample was saturated. (k) visualizes the difference of (d) and (e), and (l) depicts the sum of (d) and (g), highlighting the different positions of the bubbles in these images. (m) Out-of-plane hysteresis loop of a continuous CoB/Pt film, in which the field values corresponding to images (a–l) are illustrated.<sup>†</sup>

at relevant field values of a similar field cycle. In Fig. 3.6a we see the virgin state after deposition. This remanent state shows, to the limit of our spatial resolution, equally distributed black and white domains as well as smooth domain walls. The domains with an average width of 68(4) nm are clearly resolved. Between Figs. 3.6a and 3.6b, the disk experienced a field of 65 mT, causing a significant increase of the average domain width to 83(5) nm. This is the domain width of the minority domains in all subsequent images. Comparing Figs. 3.6b and 3.6c we notice that an applied field of up to 120 mT changes the domain configuration gradually by a continuous retraction of the unfavorable domains from the edge of the disk, leaving the domain arrangement and the widths of both black and white domains in the center approximately constant. When further increasing the

field, the domains contract to multiple bubbles, see Fig. 3.6d. The diameter of these bubbles equals, to the limit of our resolution, the widths of the minority domains that we find in any stripe-domain pattern along the hysteresis loop. In this part of the hysteresis loop, which corresponds to the only hysteretic part of the macroscopic  $M_z - H_{\text{ext}}$  loop, the magnetic field required to induce sizable changes in the domain configuration is of the order of a few tens of mT only. A further increase of the field reduces the number of bubbles, and one of the remaining bubbles moves to restore an energetically more favorable configuration, see Figs. 3.6e and 3.6k, the latter showing the differences between Figs. 3.6d and 3.6e to highlight the new position of one of the bubbles.<sup>†</sup>

After saturation and returning close to remanence (Fig. 3.6f), we find a highly symmetric, meander-like domain configuration with equally distributed black and white domains and smooth domain walls as before in Fig. 3.6a. When applying the external field in the opposite direction, we observe, similar to Figs. 3.6d and 3.6e, multibubble states before saturation of the disk, but now at entirely different positions, c.f. Fig. 3.6g. This is also visualized in the sum of Figs. 3.6d and 3.6g shown in Fig. 3.6l. After saturation, we observe in particular on the descending branch of the hysteresis loop (Fig. 3.6h), but also at remanence (Fig. 3.6i), once more highly symmetric states, which, however, are otherwise not correlated to the patterns we found before in Figs. 3.6a and 3.6f. The formation of symmetric patterns without correlation to previous field cycles is a general property of the sample, which is demonstrated also in another remanent state in Fig. 3.6j. Following the terminology used by Pierce *et al.*<sup>117</sup> to characterize the (microscopic) hysteresis and the related pinning in Co/Pt-type materials, the presented data (consistent with all the images that we acquired on the system) demonstrate that our patterned CoB/Pt material has neither major loop microscopic return point memory nor major loop microscopic complementary point memory.<sup>†</sup>

The increase of the initial as-grown domain width to an apparent intrinsic width of 83(5) nm after applying a small external field can be related to the formation of a metastable configuration during fabrication, which included the heating of the sample in the lithography process. In general, our observations reveal a low density of pinning sites so that there are very few considerable energy barriers separating energetically degenerate magnetic states. This is particularly clear from the consistently circular symmetry of the observed domain configurations commensurate with the circular geometry. From the absence of return point memory and complementary point memory, we conclude that the different energetically degenerate magnetic states that are commensurate with the symmetry of the geometry, such as those shown in Figs. 3.6f and 3.6i, are accessible from the saturated state without significant energy barriers (which would favor just one state). This means the energy landscape is rather flat, as any roughness in this energy landscape, which defines the pinning barriers, is overcome by the shape anisotropy energy, which

hence sets an upper limit for the average pinning strength. Since the shape anisotropy results from in-plane components of the stray field, this energy is small. The smooth domain walls and the constant width of the minority domains are further indications for a particularly low pinning strength and density in our material configuration. The fact that the observed bubbles are not located at predefined positions and that they can be moved by moderate field changes demonstrates additionally that even sparsely distributed strong pinning sites are absent in our material. Therefore, bubbles are not trapped in a considerable pinning potential well, which opens the possibility to observe some of the recently predicted dynamical behavior of magnetic bubbles arising from their topological properties.<sup>2†</sup>

### 3.5. Dynamic imaging in a CoB/Pt disk

To demonstrate the suitability of the material for pump-probe dynamic imaging of field-induced domain dynamics, a microcoil was fabricated lithographically around a disk of the CoB/Pt<sub>40</sub> material configuration. Through this microcoil, 4 ns long rectangularly shaped pulses were injected at a repetition rate of 1.25 MHz, generating an approximately uniform out-of-plane field of 25 mT. The pulse injection was synchronized with the probing x-rays to allow for imaging of the magnetic state at variable times after the start of the pulse. We set the system in a multibubble configuration by applying an *in situ* static magnetic field of 140 mT parallel to the excitation field. To demonstrate the repeatability, we present an image of the magnetic state during the pulse and one image long after the pulse (46 ns), where each image has been reconstructed from the accumulated average of several  $10^9$  pump-probe iterations. The total accumulation of the two images was subdivided into several sequences of alternating time delays to confirm that the observed differences are fully dynamical in nature and not due to a single, thermally activated event of domain wall motion.<sup>†</sup>

In Fig. 3.7 we present dynamic images of the magnetic domain configuration long after the pulse in Fig. 3.7b and on the plateau of the pulse in Fig. 3.7c. Both images show clearly different magnetic contrast. In both images, we can identify three domains (highlighted by black dotted lines in Figs. 3.7b and 3.7c) with magnetic moments pointing downwards, opposite to the upward-oriented external field and the otherwise upward magnetized sample. When imaging long after the pulse, we observe that these minority domains are enlarged and slightly elliptical. During the pulse (Fig. 3.7c), the minority domains shrink to a rounder shape, a dynamics that resembles a breathing mode of magnetic bubbles expected for homogeneous out of plane fields. To highlight the changes due to the field pulse, the border of the bubbles in the remanent state has been overlaid on both images with dotted lines. All three bubbles shrink when we apply this field pulse in the up-direction. The shrinking and expansion is highly anisotropic. Only the long axes of the elliptical

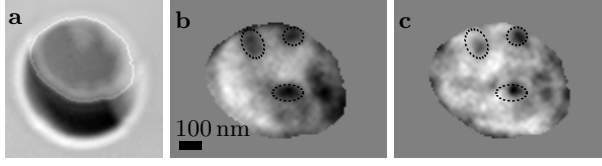


**Figure 3.7 | Proof-of-principle pump-probe dynamic imaging in CoB/Pt.** Excitation of a multibubble magnetic configuration in a 700 nm CoB/Pt multilayer disk. A static bias field of 140 mT is applied in the out-of-plane direction. (a) Topography of the sample, with the large circle defining the object hole in the opaque Au film. The area of magnetic material is highlighted by a lighter boundary and only the inner part is shown in (b) and (c). (b) Magnetic state long after (46 ns) a 25 mT homogeneous magnetic field pulse of 4 ns duration, where black indicates magnetization pointing down, white indicates magnetization pointing up (positive field direction). This state corresponds to the state without a field pulse. The black dotted lines mark the borders of bubble-like configurations of down-pointing magnetic moments. (c) Domain configuration of the disk on the plateau of the pulse. The border of the bubble domains off the pulse is sketched again with dotted lines to highlight the shrinking of the bubbles.<sup>†</sup>

domains vary considerably. The length of the short axes remains constant with varying field strength, which is in agreement with our observation of a constant width of minority domains in the static hysteresis loop.<sup>†</sup>

These proof-of-principle images of dynamic domain changes demonstrate that our material configuration is magnetically sufficiently soft to allow for inducing significant and clearly detectable changes using microcoil-generated nanosecond field pulses with several MHz repetition rate. The dynamic response of the system is deterministic and elastic, allowing us to obtain clear images from an accumulated average of several  $10^9$  pump-probe iterations per image.<sup>†</sup>

### 3.6. Conclusions

From the observed static domain states at variable external fields, we conclude that, in contrast to the investigated Co/Pt and Co/Pd multilayers, CoB/Pt multilayers exhibit a very weak influence of pinning on the magnetic states. This leads to the necessary viscous motion of domain walls in an external magneto-static potential and the resulting reproducibility for repetitive pump-probe imaging of magnetic domain dynamics. We demonstrate the suitability of this material in a dynamic pump-probe imaging experiment of multibubble soliton<sup>124</sup> states, where we were able to observe and repeat the expansion of bubbles to elliptical domains and the shrinking back to bubble states. For high anisotropy systems, our material configuration has the potential to become of equally wide spread use as permalloy is for low anisotropy systems, and thereby enabling a comparable range of fundamental experiments for this technologically important class of materials.<sup>†</sup>

# Chapter 4

## Topological mass of skyrmionic spin structures

---

*Skyrmions are winding vector fields characterized by a spherical topology, such as bubbles in ferromagnetic films with perpendicular anisotropy. Despite their quasi-particle properties, magnetic Skyrmions have been described as massless entities so far. Here, we demonstrate the presence of strong inertia in a magnetic bubble and its paramount role in determining its dynamics. This is achieved by nanoscale imaging of the GHz gyrotropic eigenmode of the bubble via time-resolved x-ray holography. We find a surprisingly large mass  $|M| > 8 \times 10^{-22}$  kg that is a direct consequence of the topological confinement of the Skyrmion and the energy associated with its size change. We expect that this topological mass, which fundamentally governs the dynamics by increasing the degrees of freedom, is found in all (meta-)stable skyrmionic systems.\**

---

### 4.1. Introduction

Skyrmions refer to vector fields with spherical topology and quasiparticle properties. Such real space topological solitons have been observed in Bose-Einstein condensates,<sup>11,12</sup> antiferromagnetic superconductors,<sup>13</sup> quantum field theories,<sup>15</sup> and electron spin configurations in condensed matter.<sup>2-5,7,9,10,125,126</sup> Magnetic Skyrmions are promising candidates for current driven memory devices<sup>126</sup> due to their high mobility at ultra low current densities.<sup>9</sup> So far, existing theoretical descriptions using quasiparticle models of magnetic Skyrmions describe them as simple massless particles<sup>26,127,128</sup> since previous quasi-static experimental investigations have not allowed for the determination of inertial effects. However, recent numerical simulations of Skyrmions in spin systems suggest that these quasiparticles exhibit inertia, which should be manifested in the existence of a GHz gyrotropic motion with two characteristic modes, one clockwise and one counter-clockwise.<sup>2,3</sup> Here we image the gyrotropic trajectory of a single skyrmionic magnetic quasiparticle and observe that position and momentum are independent parameters, which requires the availability of at least two independent modes. The

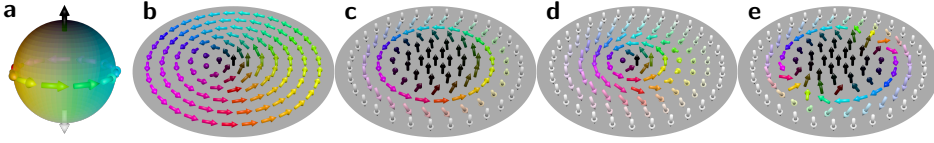


**Figure 4.1 | Illustration of the topology of magnetic spin structures with a disk-shaped domain space.** (a) A sphere  $S^2$  with its identity map vector field, which is the most general representation of the spin space (since spin is a vector in  $\mathbb{R}^3$  with constant modulus). The hue of the color represents the azimuthal angle  $\varphi$ , and the black and white color visualizes the polar angle  $\theta$  of the spherical coordinates. (b) A magnetic vortex, which is a vector field covering only the upper hemisphere, hence  $N = 1/2$ . (c) A magnetic bubble, which covers the sphere exactly once ( $N = 1$ ). The poles are mapped to extended areas (the inner and outer domains). Hence, all spins at the boundary of the domain space have to point in the same direction, which confines the inner domain and the domain wall. (d) A chiral Skyrmion, which has a different radial distribution than the bubble.<sup>130</sup> Topologically, however, both are the same, since the bubble can be obtained from the chiral Skyrmion by expanding its inner domain. (e) A bubble with a winding pair of vertical Bloch lines (topological defects) in the domain wall. Now, apart from the poles, each spin at the sphere is represented twice, and when continuously deformed, the vector field covers the sphere twice. Therefore, the topology is double spherical ( $N = 2$ ).\*

trajectory is in excellent agreement with the theoretical model, and from a fit we obtain an inertial mass  $|M| > 8 \times 10^{-22}$  kg that is much larger than masses found for other magnetic quasiparticles.<sup>20,21,107,129</sup> Such a large mass has fundamental impact on the dynamical behavior of magnetic Skyrmions since it leads to additional degrees of freedom. We attribute the presence of strong inertia to the full confinement common to all skyrmionic spin structures, an inherent property of their topology. We anticipate that the concept of topological mass can be applied to other skyrmionic systems, and we provide a sensitive experimental tool for investigating the role of topology on the GHz dynamics of magnetic systems at the nanoscale.\*

The special topology defining all skyrmionic vector fields is characterized by the possibility to continuously deform their domain space to a spherical shape, while retaining their image (*homotopy* of the vector field to the identity map of the sphere, illustrated in Fig. 4.1).<sup>15</sup> The number of times the sphere is covered during this continuous deformation is a topological invariant, the so-called Skyrmion number  $N$ . Figure 4.1 illustrates possible skyrmionic spin structures: a magnetic bubble and a chiral Skyrmion, alongside with a related, but topologically distinct, magnetic vortex, and an  $N = 2$  bubble. For integer  $N$  the boundary of the domain space is mapped to one of the poles of the sphere, and an area in the interior is mapped to the other pole. These two areas, called domains, are smoothly connected by a closed loop domain wall. Both the inner domain and the domain wall never touch any boundary of the domain space; they are confined in all dimensions by the outer domain. Most often, the combination of inner domain and domain wall exhibits particle-like properties, and the corresponding quasiparticles



are called Skyrmions. In magnetism, various interactions can lead to the formation of two-dimensional skyrmionic spin structures,<sup>130,131</sup> including bubbles, which result from the interplay of exchange, dipolar and anisotropy energy, and chiral Skyrmions, which arise as a consequence of an additional Dzyaloshinskii-Moriya interaction.<sup>131\*</sup>

The dynamics of Skyrmions is directly related to their topology. As shown by Thiele, the Skyrmion number enters the equation of motion of a rigid magnetic structure through the gyrocoupling vector.<sup>27</sup> This vector is proportional to  $N$  and couples to the velocity of the particle, driving it on a circular trajectory with well-defined chirality determined by the sign of  $N$ . Although this model is well suited to describe magnetic vortices, we show here that the detailed dynamics of Skyrmions can be explained only by extending the model to include an effective mass term. The presence of the inertial mass originates from the ability of the system to store energy internally during its motion;<sup>31</sup> in our system this is achieved through a deformation in shape, a feature which we expect to be common to all confined (meta-)stable structures. Such deformations are visible in simulations of bubbles<sup>2</sup> as well as of chiral Skyrmions.<sup>3</sup> Inertia of domain walls, confined in one dimension and extended in the other, has been known for a long time.<sup>46</sup> Domain wall inertia causes retardation, but does not change the trajectory of the wall dynamics.<sup>22</sup> In contrast, as shown in this thesis, fully confined Skyrmions exhibit an additional topological source of inertia that makes the effective mass very large compared to straight domain walls and induces fundamental changes to their trajectory. This shows that previous theoretical descriptions that ignore inertia are incomplete and inadequate to describe the full dynamics of Skyrmions.\*

## 4.2. Experimental results

The experiment has been performed using time-resolved pump-probe x-ray holography<sup>78,95</sup> to image the gyrotropic trajectory of a skyrmionic magnetic bubble in a sub-micrometer diameter magnetic disk (Fig. 4.2a and chapter 2) after a magnetic field gradient excitation. The magnetic imaging was performed at the UE52-SGM beamline at BESSY II in Berlin, Germany. The sample was prepared as described in chapter 2, with a magnetic layer of material CoB/Pt<sub>30</sub> patterned to a 550 nm disk with a notch at the top, a Au microcoil tightly around the disk, and two reference holes with diameters of 80 nm and 55 nm (see Fig. 2.4). A static out-of-plane field of  $-120$  mT has been applied, resulting in a ground state with two bubbles, see Fig. 4.2c. We will focus on the dynamics of one of these bubbles (the one marked by an arrow in Fig. 4.2c), subsequently called “the bubble”, because the other one does not move sufficiently for experimental observation. The excitation of this skyrmionic state has been achieved by injecting bipolar current pulses to a microcoil surrounding the disk, generating an out-of-plane field pulse. These

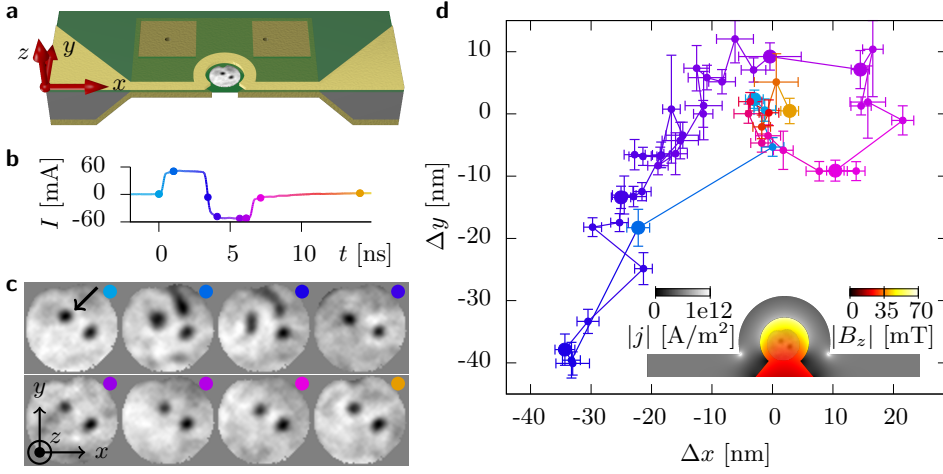


**Figure 4.2 | Excitation of a multi-bubble state by an external magnetic field pulse.** (a) Schematic cross section of the sample, the pump and the imaging structure on the Si<sub>3</sub>N<sub>4</sub> membrane (light green), which is supported by a Si frame (grey). The 550 nm diameter magnetic disk (black/white object in the center) is surrounded by an Au microcoil (bright yellow). The back side of the membrane is covered by an Au mask (dark yellow) with three holes, one with 800 nm diameter behind the magnetic CoB/Pt disk and two reference holes at a few  $\mu\text{m}$  distance. (b) Temporal evolution of the injected current generating the magnetic field pulse. The color of this plot represents the time delay, and is used consistently throughout this thesis. (c) Magnetic domain configuration of the disk at different time delays, as indicated by the colored point in each image. In the black areas the magnetization is antiparallel to the static field (i.e., pointing towards the reader), while in the white areas it points parallel. (d) Displacement ( $\Delta x, \Delta y$ ) of the center of magnetization of the bubble indicated by an arrow in (c) with the time encoded by the color of the points. Large diameter dots correspond to the images shown in (c). The inset shows a finite differences calculation of the current density in the microcoil and the corresponding  $z$ -component of the generated magnetic field inside the coil for a current of 52 mA.\*

bipolar rectangular microwave pulses with a current of 52 mA were injected to the microcoil at a repetition rate of 1.25 MHz synchronized to the probing x-rays (Fig. 4.2b). In our setup, a positive current generates a field which is antiparallel to the negative static bias field, thus favoring the growth of the bubble domains and the nucleation of new reverse domains. Details of the excitation setup can be found in chapter 2.5. The resulting field, estimated using finite elements calculations, was roughly homogeneous in the out-of-plane direction (inset Fig. 4.2d), with a strength of  $B_z = -35$  mT at the position of the bubble at maximum negative current, and small in-plane components  $B_x = -1.5$  mT and  $B_y = 6.5$  mT. The residual field gradient was  $\partial_x B_z = 8.7$   $\mu$ T/nm and  $\partial_y B_z = -45$   $\mu$ T/nm, pushing the bubble towards the center of the disk. The magnetic domain configuration was imaged at variable time delays  $t$  with a temporal resolution of 50 ps (standard deviation) determined by the duration of the synchrotron x-ray pulses and their temporal jitter with respect to our electronics.<sup>132</sup> For each time delay, the pump-probe experiment was repeated about  $10^9$  times, corresponding to a total number of  $6.4(5) \times 10^7$  recorded photons of each helicity (positive and negative) per image. Images were recorded in a random non-chronological order.\*

Selected images acquired at distinct times after the start of the pulse are presented in Fig. 4.2c. In the reconstructed real space magnetic image, the area of the disk is cropped using the topographic information in the holograms as shown in Fig. 2.5. To generate the required field gradient to displace bubbles, we applied a positive field pulse to nucleate a third domain at the top of the disk, and we used the strong (and ultrafast) gradient of the stray field created by this domain to displace the bubble sufficiently for experimental observation. Field gradients of this magnitude (expected to be of the order of  $\text{T}/\mu\text{m}$ )<sup>2</sup> are otherwise experimentally inaccessible, in particular with rise times of only a few hundred picoseconds. We observe that the third domain retracts and annihilates at the edge of the disk after reversal of the field pulse. The bubble subsequently returns to its equilibrium position. A digital video of the bubble motion can be found attached to this thesis. This movie shows a succession of images corresponding to the data points in Fig. 4.2, sorted chronologically by their time delay and presented at a constant frame rate (i.e., the time between two images of the movie does not correspond to the time delay between these images). The time delay of each image is indicated by a sketch of the pulse shape in the top of each image.\*

For a quantitative determination of the position, the bubble is defined as a region of connected pixels with common below-average intensity (i.e., pixels which appear black in the image). The center of the bubble is obtained by calculating the first statistical moment (center of “mass”) of all pixels of the bubble. This statistical method determines the center with much higher accuracy than the actual spatial resolution (which is about 40 nm for the reconstruction of the smaller reference in our case). We estimate the precision (i) by evaluating the reconstructions from

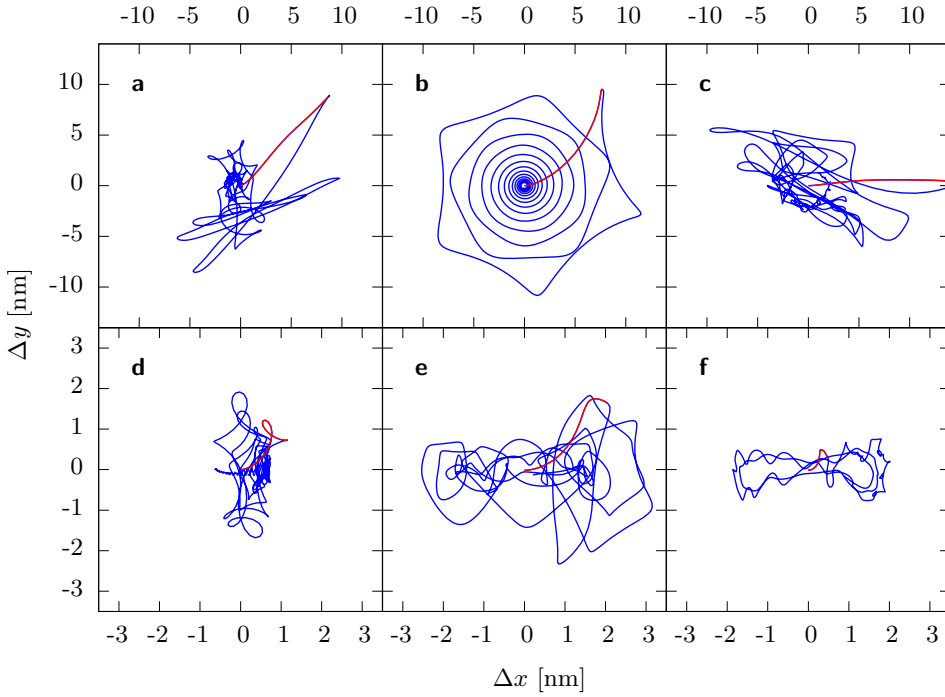


**Figure 4.3 | Simulated trajectories of bubbles with variable Skyrmion numbers.** Trajectories  $(\Delta x, \Delta y)$  of the center of magnetization of the bubbles are shown for  $|N| = 0$  in (a) for  $|N| = 1$  in (b) for  $|N| = 2$  in (c) for  $|N| = 3$  in (d) for  $|N| = 4$  in (e) and for  $|N| = 5$  in (f). The simulations have been performed for negative  $N$ . For positive  $N$ , the trajectories are spatially inverted. Only the  $|N| = 1$  bubble moves on a spiraling trajectory around the equilibrium position. The total simulation time is 15 ns. The excitation is applied for the first 0.2 ns, and the respective part of the trajectories is plotted with red lines.\*

both references independently and assuming that the difference corresponds to one standard deviation, and (ii) by adding a conservative estimate of the average spread of the data of 1.4 nm (which was derived by assuming a linear trajectory in the time interval  $t \in [3.44 \text{ ns}, 5.67 \text{ ns}]$  and by calculating the standard deviation of the data from a linear fit). This results in an average spatial accuracy of 2.3 nm for the determination of the center of the bubble.\*

The full trajectory of the bubble, plotted in Fig. 4.2d, forms a loop with clearly distinct excitation and relaxation paths. In particular, after  $t = 4.5 \text{ ns}$ , the bubble moves on a spiraling trajectory, an unequivocal signature of the influence of the gyrocoupling vector and hence of a non-zero Skyrmion number. In materials with preferred out-of-plane spin alignment, all domains that do not touch the sample boundary are configurations with integer  $N$ . By micromagnetic simulations, we show that the dynamics of a Skyrmion, in particular its trajectory, is characteristic for its topology and its Skyrmion number  $N$ . For this purpose, we have simulated the trajectories of bubbles with variable  $|N|$ , which allows us to identify the measured trajectory with the simulated  $|N| = 1$  bubble.\*

We have simulated the dynamic excitation and relaxation of  $|N| = 0, 1, 2, 3, 4$  and 5 bubbles, using the parameters of Moutafis *et al.*<sup>2</sup> and the MICROMAGNUM simulation software.<sup>133</sup> Larger  $N$  (so called *hard bubbles*) are highly unlikely to be found in our material due to its small quality factor of  $Q = 0.86(6)$ .<sup>18</sup> Also, we start with energetically relaxed initial configurations, that is, we do not include any non-topological defects, such as non-winding vertical Bloch lines. While these defects can exist, they are very rare,<sup>18</sup> and are expected to annihilate during the first excitation. The Skyrmion number  $N$  of the magnetization configuration  $\mathbf{m} = \mathbf{m}(x, y)$ , where  $\mathbf{m}$  is a unit vector along the local magnetization, is calculated for all simulation steps.\*

A spiraling trajectory as observed in the measurements is only seen in the simulation of the  $|N| = 1$  bubble. For all other topologies, the trajectories appear very irregular: they cross themselves several times, and go through the potential minimum or spiral away from the equilibrium position in some instances. Therefore, we conclude that the observed trajectory in Fig. 4.2 corresponds to an  $|N| = 1$  bubble. (Even though, in contrast to the simulation in Fig. 4.3b, the measured trajectory in Fig. 4.4 is smooth and without spikes. We will return to this point in section 4.3). Since we know the direction of the applied field, we also know the polarity of the bubble and thus its Skyrmion number  $N = +1$ .\*

Our experiment constitutes the first direct experimental observation of GHz dynamics of a skyrmionic spin structure, which was made feasible due to our extremely high spatial resolution of better than 3 nm for tracking the bubble. This outstanding resolution for time-resolved experiments can be reached with x-ray holography because the imaging process is intrinsically insensitive to drift.<sup>78,95\*</sup>

### 4.3. Data analysis

The observed gyrotropic trajectory is in excellent agreement with the recently proposed theoretical model assigning to the  $N = \pm 1$  bubble an inertial mass. The theory predicts a second order differential equation of motion for the center of mass  $\mathbf{R}$  of the magnetization<sup>31</sup>

$$-M\ddot{\mathbf{R}} + \mathbf{G} \times \dot{\mathbf{R}} + D\dot{\mathbf{R}} - \partial_{\mathbf{R}}U = 0. \quad (4.1)$$

As in chapter 1.1, we approximate the magnetostatic potential by  $\partial_{\mathbf{R}}U = K\mathbf{R}$ . The general solution of this equation, which we derive in Appendix B, is a superposition of two damped spiraling motions, one clockwise (CW) and one counter-clockwise (CCW), with eigenfrequencies  $\omega_{1,2}$ , damping time constants  $\tau_{1,2}$ , and complex amplitudes  $\bar{A}_{1,2}$ , around an equilibrium position  $\bar{R}_0$ :

$$\bar{R}(t) = \bar{A}_1 \exp(i\omega_1 t - t/\tau_1) + \bar{A}_2 \exp(i\omega_2 t - t/\tau_2) + \bar{R}_0(t), \quad (4.2)$$

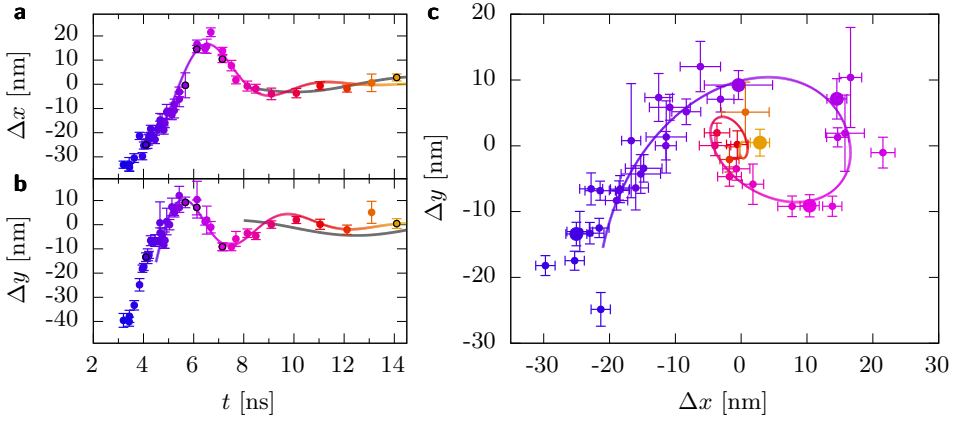


**Figure 4.4** | Analytic description of the gyrotropic motion of the bubble. (a-b) Displacements  $\Delta x$  and  $\Delta y$  of the  $x$  and  $y$  coordinate of the center of magnetization of the bubble versus time. (c) Trajectory of the bubble. Lines in (a-c) represent a fit of the analytical model to the experimentally observed bubble gyration (points). The color encodes the time after the start of the bipolar pulse (see Fig. 4.2b). Highlighted symbols correspond to the images shown in Fig. 4.2c. The gray lines in (a) and (b) show the best fit with a single frequency model to the data after  $t = 8$  ns, which is not able to describe the data. Error bars represent standard deviation.\*

Here, the vector  $\mathbf{R} = (X, Y)$  is conveniently parametrized by the complex number  $\bar{R} = X + iY$ . The equilibrium position  $\bar{R}_0$  is time-dependent due to an effective dynamical magnetic field gradient during the pulse. The two amplitudes of the gyrotropic modes are defined by the initial position and velocity. The theoretical model given by equation (4.2) describes accurately the gyrotropic part of the observed trajectory  $\mathbf{R}(t) = (X(t), Y(t))$ . This is visualized in Fig. 4.4, showing the projections  $X(t)$ ,  $Y(t)$  and  $Y(X)$  in a, b and c, respectively. A good fit to the data is only possible with a globally simultaneous, coherent superposition of two gyrotropic modes: a CW higher frequency mode, and a CCW lower frequency mode. This confirms the presence of an inertial mass, since, without the mass term, the sense of gyration would be fixed by  $G$  (which is a constant of motion), and only one mode could be excited at a time.\*

All parameters of Eq. (4.2) are determined from a fit to the experimental data. In this fit, data points with  $t < 6$  ns are weighted by half to compensate for the fact that there are significantly more data points in that region than at larger time delays. We include only data from the gyrotropic part of the trajectory (data points with  $t > 4.5$  ns). As outlined in the Supplemental Material of Ref. 31, the ratio of the damping strengths equals the ratio of the respective frequencies, that is,  $\tau_2 = \tau_1 \omega_1 / \omega_2$ . The equilibrium position  $\bar{R}_0$  is shifted by a field gradient. The applied field pulse, of which only the negative part coincides with the fit interval, has a weak gradient, and more significantly, the negative  $B_z$  during the pulse causes a modification of the sample magnetization, in particular a shrinking of the second bubble. The modification of the stray field due to this shrinking leads to

an effective field gradient of known direction  $\partial_x B_z^{(b)}/\partial_y B_z^{(b)} = -1.5$ ,  $\partial_x B_z^{(b)} > 0$ , as determined from the observed positions of the two bubbles, but unknown strength. For simplicity, we assume instantaneous modification of the second bubble by the field pulse, and we approximate the pulse by a step function with a step at  $t_1 = 6.45$  ns, which equals the time where the real pulse decays to half its maximum value after being switched off. We therefore have two distinct constant values  $\bar{R}_1 := \bar{R}_0(t < t_1)$  and  $\bar{R}_2 := \bar{R}_0(t \geq t_1)$ , the latter corresponding to the static equilibrium position, which is determined from the average of all positions after  $t > 9.5$  ns. The value for  $\bar{R}_1$  is obtained from a fit to the data, and we constrain the parameters  $A_1$  and  $A_2$  for the two fit regions  $t < t_1$  and  $t \geq t_1$  to ensure the continuity of the total function in its value and its first derivative. \*

We obtain the best fit with frequencies of  $\omega_1 = 1.00(13)$  GHz (CCW mode) and  $\omega_2 = -1.35(16)$  GHz (CW mode) and with  $\bar{R}_1 = X_1 + iY_1$  with  $X_1 = 5.1(8)$  nm and  $Y_1 = -10.2(15)$  nm. The frequencies of both modes are in the GHz regime, which is in line with numerical simulations.<sup>2</sup> The same characteristic spectrum of one CW and one CCW mode, with very similar frequencies, has been predicted by numerical simulations for chiral Skyrmion crystals, underlining the fundamental topological origin of the gyrotropic motion and of the presence of inertia.<sup>3</sup> From the fit we can determine the inertial mass  $M = G/(\omega_1 + \omega_2)$  of the bubble and the potential stiffness  $K = -M\omega_1\omega_2$  by assuming a bubble with  $N = 1$  (we define frequencies positive if they correspond to counter-clockwise motion, which is opposite to the definition used in Ref. 31). Due to the large uncertainties in the frequencies, and in particular of the frequency sum  $\Sigma\omega = (\omega_1 + \omega_2) = -0.4(2)$  GHz, we cannot determine a meaningful upper limit for the inertia of the bubble. However, we can derive a highly certain lower limit (confidence level of  $5\sigma$  or 99.99994 %) for the inertial mass by  $M_{LL} = G/[\Sigma\omega - 5\sigma(\Sigma\omega)]$ , where  $\sigma(\Sigma\omega)$  denotes the standard deviation of  $\Sigma\omega$  (note the negative sign of  $\Sigma\omega$ ). The lower limit for the areal mass density  $\rho_{LL}$  is given by  $\rho_{LL} = M_{LL}/(2\pi\mathcal{T}_{Co}\langle R \rangle)$ , where  $\langle R \rangle = 50(10)$  nm is the average radius of the bubble and  $\mathcal{T}_{Co} = 12.0(1)$  nm is the total CoB thickness, arriving at  $\rho_{LL} = 2.0(4) \times 10^{-7}$  kg/m<sup>2</sup>. From the product of the frequencies we obtain the stiffness  $K = 3.5(16) \times 10^{-3}$  N/m of the local magnetostatic potential.\*

We note that, in contrast to the simulation in Fig. 4.3b, the measured trajectory in Fig. 4.4 is smooth and without spikes, even though they are described by the same model. This is due to the fact that, in the measurement, the higher frequency mode has a larger amplitude than the lower frequency mode at all times of the measured gyration. Due to the stronger damping of the higher frequency mode, the ratio of the amplitudes of the modes eventually reverses. The theoretical fit shows a transition to a hypocycloidal trajectory at  $t = 16.2$  ns, accompanied by a change of the global sense of rotation from CW to CCW. The global amplitude at that stage is however expected to be smaller than 0.5 nm, which is below our

spatial resolution and therefore cannot be observed.\*

In a final step, we estimate the dipole moment  $d = 2.1(4) \times 10^{16} \text{ Am}^2$  of the bubble given by the product of the bubble area  $7(3) \times 10^{-15} \text{ m}^2$  with the total CoB thickness  $t_{\text{Co}}$ , the saturation magnetization  $M_s = 1.19(3) \times 10^6 \text{ A/m}$ , and a factor 2 to account for the fact that the difference between the magnetization of the inner and of the outer area of the bubble is  $2M_s$ . To shift a magnetic dipole in a parabolic potential by the distance  $\bar{R}_1$ , a field gradient of  $\partial_{\bar{r}} B_z = K \bar{R}_1 / d$  is required. Our fit values indicate the presence of a strong gradient  $\partial_x B_z^{(\bar{R}_1)} = 90(50) \mu\text{T/nm}$  and  $\partial_y B_z^{(\bar{R}_1)} = -170(100) \mu\text{T/nm}$  during the negative part of the pulse. We can write this field gradient as a superposition of the gradient of the applied pulse excitation and an extra gradient. We attribute the presence of this extra gradient to the shrinking of the second bubble during the negative field pulse and to a small additional contribution from the re-alignment of the in-plane components of the spins near the surfaces all over the disk. These in-plane components of the spins near the surfaces are expected in our material due to its relatively small perpendicular anisotropy constant expressed by its quality factor of  $Q = 0.86(6)$ .\*

## 4.4. Discussion

The lower limit for the mass of the bubble corresponds to an areal mass density of  $2.0(4) \times 10^{-7} \text{ kg/m}^2$ . Such large inertia has been reported so far only for cross-tie domain walls.<sup>134</sup> It is at least two orders of magnitude larger than any value previously reported for straight domain walls,<sup>20,21,107,129</sup> and (within the error bars) a factor of five larger than the corrected Döring mass density for straight Bloch domain walls in our material (see chapter 1.3 and Appendix A for the calculation of the Döring mass density of straight walls in our material). In particular, in materials with high damping, such as ours, domain wall inertia has been previously found to be negligible,<sup>107,129</sup> demonstrating that the distinct spin structure is the origin of the large inertia. The amplification of inertia in confined spin structures by up to two orders of magnitude is known from Bloch lines and has been attributed to the local exchange energy.<sup>18\*</sup>

We attribute the surprisingly large mass of magnetic Skyrmions to their full confinement, leading to an additional energy reservoir associated with a change of its size (breathing mode). Such a breathing mode is inherent to all structures that are fully confined in thermodynamic equilibrium, such as Skyrmions (although also found in some topologically trivial ( $N = 0$ ) structures such as dissipative solitons),<sup>135</sup> where energy can be stored by a change in areal size. The particularly large mass found in magnetic Skyrmions is related to the strong dipolar energy of the breathing mode. The non-local breathing mode energy is not included in the Döring mass and has been neglected in previous theoretical models,<sup>31</sup> but contributes significantly to the mass found here. The previously found large mass



of cross-tie walls can be attributed to their local skyrmionic spin structure.<sup>10,136\*</sup>

The very large topological mass of magnetic Skyrmions has implications far beyond the simple retardation of the response to an excitation reported for domain walls so far, since it increases the number of degrees of freedom for the motion of these topological quasiparticles. Thus, in contrast to what has been argued before,<sup>26,127,128</sup> inertia must be included in quasiparticle models of Skyrmions to reproduce and understand their dynamics, which is a key prerequisite to using skyrmionic spin structures in applications.\*

## 4.5. Conclusions

In summary, we present the first direct observation of GHz dynamics of Skyrmions and of picosecond viscous motion of domains in high anisotropy materials, using ultrahigh time- and space-resolved x-ray holography. We find that the gyrotropic motion of the Skyrmion consists of two distinct eigenmodes, implying the presence of inertia. The inertial mass, estimated to be larger than  $8 \times 10^{-22}$  kg, is significantly larger than predicted by existing models for inertia in magnetism. The additional contribution is of topological origin and is therefore a common property of skyrmionic systems. We have shown that magnetic nanoscale bubbles without topological defects are an ideal system to study the dynamics of Skyrmions at the technologically relevant sub-nanosecond timescale. They provide, in combination with high-resolution x-ray holographic imaging, a tool for further fundamental investigations of topologically influenced dynamics, such as the motion of single Skyrmions in nanoscale devices, which have been recently proposed for novel devices.<sup>126\*</sup>



# Chapter 5

## Open questions

---

*In this thesis, we report to our knowledge the first experimental demonstration of the GHz gyrotropic motion of a magnetic Skyrmion, from which we deduce the equation of motion that determines the emergent dynamics of skyrmionic spin structures. Even though tremendous improvements in the material as well as the imaging technique were made, they still have great potential for improvements. Furthermore, we have observed a number of effects and others seem likely from a theoretical point of view, but more detailed studies are required to draw conclusions. In this chapter, we summarize the most immediate open questions and present some ideas for approaches to address these issues.*

---

### 5.1. Field-induced domain wall motion in a multi-domain configuration

In the search for bubble dynamics, we have observed the magnetic field induced propagation of domains in an overall worm domain state. A selection of images acquired in one such instance is presented in Fig. 5.1. The sample and the setup are identical to that used in chapter 4. The dynamics are observed at a static external field of  $-84(5)$  mT in response to a unipolar dynamic field pulse with a peak current of  $-60$  mA and a duration of 5 ns. Such a microwave pulse generates

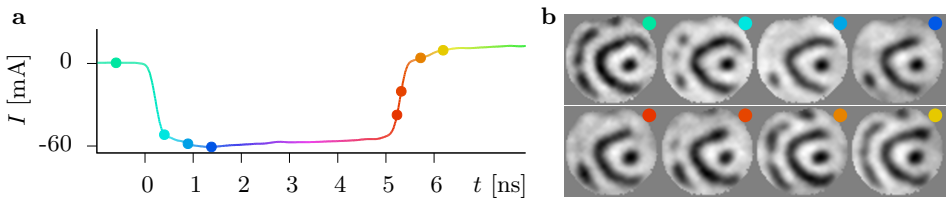


**Figure 5.1 | Repetitive worm domain propagation upon a unipolar magnetic field pulse.** The experimental setup is identical to Fig. 4.2. (a) Plot of the pulse injected to the microcoil to generate a magnetic field pulse. The large circles correspond to the times the images in (b) were acquired at. (b) Magnetic images of the domain pattern at various times as indicated in (a). Black indicates magnetization pointing up (towards the reader) and white indicates magnetization pointing down.

a magnetic field pulse of  $B_z \approx -40$  mT favoring the white (down) domains in Fig. 5.1. We see that, in response to the field pulse, the black domain at the left edge of the disk first splits into multiple fragments that eventually disappear. Only afterwards, 0.4 ns after the start of the pulse, is the domain pattern in the right part of the disk responding visibly to the strong change of the external magnetic field. Here, the black worm domain is retracting continuously from the edge and shrinks in length without fragmentation. At  $t = 1.4$  ns, the domain configuration has relaxed to the external field of the plateau of the field pulse. Between 0.4 ns and 1.4 ns, the domain wall at the end of the black worm domain has traveled a distance of 90(5) nm. The average speed of the domain wall, of 90 m/s or  $0.45v_W$  (with the maximum steady state velocity  $v_W = \frac{\gamma K_\perp \Delta_0}{\mu_0^2 M_s}$ ), can be considered high. It would be very interesting to investigate this dynamics with a larger number of frames during the domain wall motion and, if possible, as a function of field pulse strength and initial domain configuration (the latter defining the local effective field). In particular, propagating worm domains would be the ideal environment to study the recently discovered effect of a change in the domain wall velocity when the total domain wall length varies by the motion.<sup>137</sup>

## 5.2. Composite Skyrmions: Inertia of vortex pairs and vortex-antivortex pairs

In chapter 4, we have argued that the large mass of cross-tie domain walls originates from their local skyrmionic structure. Such domain walls are comprised of vortex-antivortex-vortex triples,<sup>136</sup> where one of the vortices and the antivortex can be seen as a unit forming a Skyrmion with  $N = \pm 1$  (provided the polarities are opposite).<sup>10</sup> Such a vortex-antivortex pair, which has been studied, for instance, by Komineas,<sup>10</sup> is schematically depicted in Fig. 5.2. In this figure, which is a 3D representation of the simulated state of Ref. 10, the skyrmionic nature of the structure is emphasized: in contrast to magnetic bubbles, the two poles of the sphere that characterizes the Skyrmion topology are represented by in-plane spins, here the ones pointing in  $y$ -direction. The boundary of the structure is uniformly magnetized in  $+y$ -direction, while the area between the vortex and the antivortex cores is magnetized in  $-y$ -direction. In the domain wall between these two regions, the spins are rotating in the  $x$ - $z$ -plane, that is, the cores of the vortex and the antivortex are part of this domain wall.

Pairs of vortices or vortices with antivortices have been studied in a large variety of experiments,<sup>10,136,138</sup> however inertial effects have never been observed. In these experiments, it was always the out-of-plane component of the spins that has served as a measure of the coordinates of the features, and the center of the unified structure has always been measured by the mean between the coordinates of the

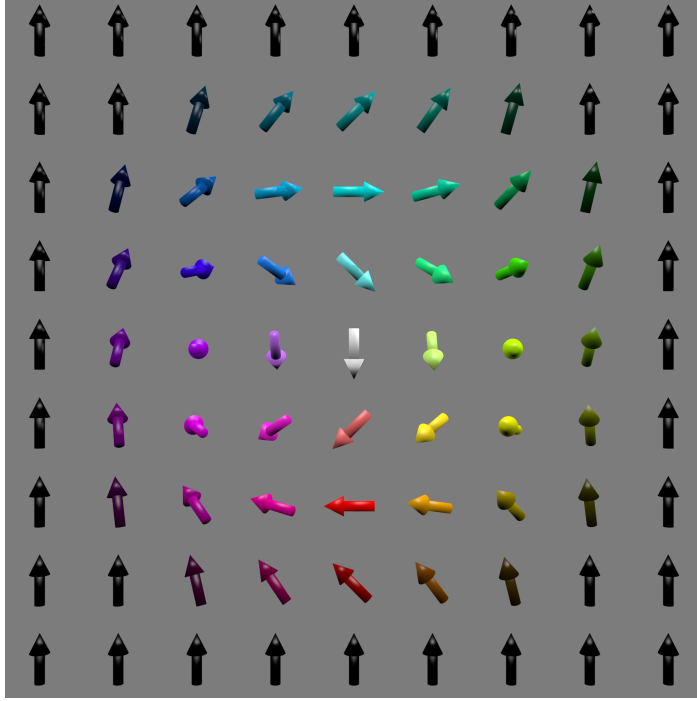


**Figure 5.2 | Skyrmionic nature of a vortex-antivortex pair.** The picture shows a sketch of the simulated vortex-antivortex state presented in Ref. 10. The colors represent the points on the sphere onto which the spins are mapped during the homotopic deformation defining the skyrmionic topology, as introduced in Fig. 4.1. The Skyrmion center is defined by the white spin, i.e., by the area between the vortex and the antivortex cores.

two (anti-) vortex cores. Viewed as a skyrmionic structure, however, the “correct” measure of the center of the structure is the first moment of the  $y$ -component of the magnetization. Such a study of magnetic vortices has been carried out neither using simulations nor experimentally. A mass term in coupled vortices would therefore constitute a novel and highly relevant aspect in the description and understanding of their dynamics.

### 5.3. Quantitative model for the inertia of Skyrmions

In the simulations of the dynamics of magnetic bubbles we have found that the mass density of the bubble is almost constant as a function of its radius. This dependency is plotted in Fig. 5.3, where we have modified the size of the bubble by using a static out-of-plane bias field. Thus far, our theoretical model predicts the presence of inertia in skyrmionic configurations, and we claim that this mass would be sizable. However, our model does not predict quantitative values for the inertia of a specific Skyrmion. Such a theory is highly desirable, and it might be a good starting point to try to explain the functional dependency of the mass density on the Skyrmion radius that we see in the simulations.

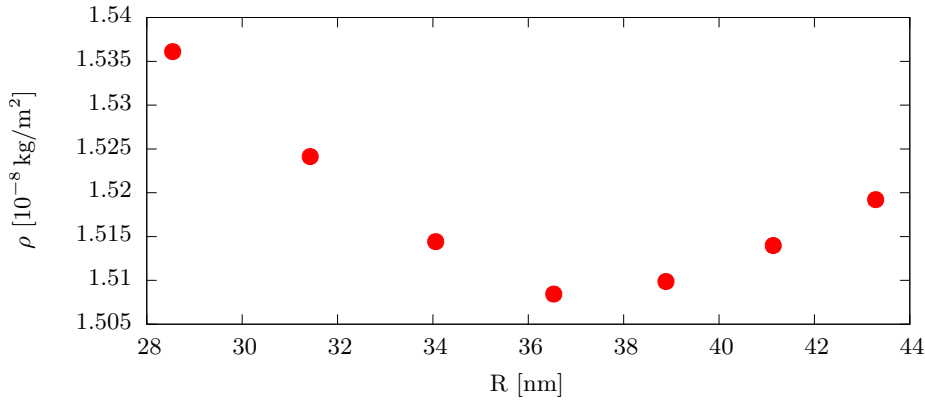


**Figure 5.3 | Evolution of the inertial mass density of a bubble Skyrmion as a function of its radius.** The mass density was derived from the frequencies of a simulated gyrotropic motion, where the simulations were carried out as described in chapter 4.3. The radius of the bubble at rest  $R$  was varied using a global static out-of-plane bias magnetic field. Smaller or larger radii are unstable with the used simulation parameters and geometry.

## 5.4. Current-induced Skyrmion motion

In the introduction to this thesis, we have argued that magnetic Skyrmions are particularly interesting since they can be displaced with ultra low current densities. However, all the investigations performed in the course of this work were based on magnetic field induced dynamics of skyrmionic spin structures. While we expect our findings to be universal and applicable to current-induced excitations of magnetic Skyrmions, challenging problems and fascinating results may be expected from the different way currents interact with spins and from the extra topological contributions arising from the Berry phases of the conduction electrons. Specifically, we envision that the knowledge about the resonant frequencies of the Skyrmions can facilitate their translation at even lower current densities than reported so far by using the effect of resonant amplification of domain wall motion.<sup>139</sup> In this scheme, the spin structure can essentially be seen as a quasi-particle in a potential well of finite height, the pinning potential. A resonant excitation leads to a continuous absorption of energy by the particle. Eventually, the particle has sufficient energy to overcome the pinning barrier, and a very small force can move it in any direction. In a Skyrmion racetrack memory,<sup>126</sup> a permanently applied tiny AC current with a frequency spectrum that covers the full range of possible resonance frequencies might thus reduce the critical current density for the motion of an isolated Skyrmion, even if the ultra low critical current density found in Skyrmion lattices should turn out to be a phenomenon that emerges from the collective motion of many coupled particles.

The investigation of current-induced bubble motion is technologically challenging since it requires the contacting of the magnetic element. In the recipe developed

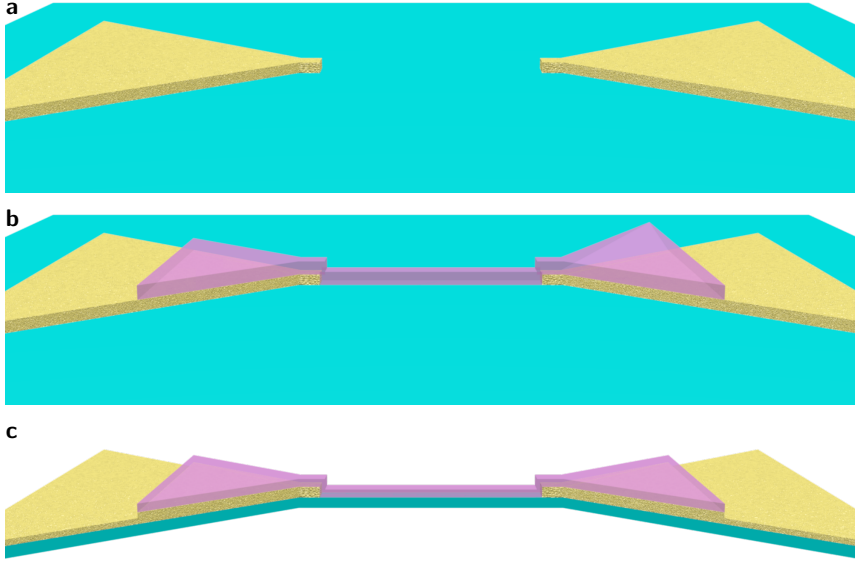


**Figure 5.4 | Fabrication steps for contacted magnetic elements.** (a) Deposition of Au contacts (yellow) on the continuous magnetic film (cyan). (b) Definition of a HSQ etch mask for the wire with some overlap on the Au contacts. (c) Ar etching to remove the magnetic material everywhere apart from where it is protected by the HSQ etch mask or by the Au contacts. These Au contacts are thick enough to ensure that a few nm of Au are still left after the etching, providing large conducting areas that can be contacted in a subsequent step.

in chapter 2, we used a silicon oxide etch mask (exposed HSQ resist) to fabricate the magnetic nanostructures with Ar milling. Such a mask is very difficult to remove after milling, which was not problematic for the investigation of magnetic field induced dynamics since it does not affect the magnetic field nor the x-ray transmission through the sample. However, to electrically contact the nanostructure, the contacts must be placed below the insulating silicon oxide etch mask. First tests have been performed to fabricate the contacts before the structuring of the magnetic film. The envisioned sample fabrication steps are schematically depicted in Fig. 5.4. Gold contact pads are fabricated directly onto the continuous magnetic film. Afterwards, HSQ resist is exposed to define the magnetic nanostructure and to protect the contact pads during the subsequent Ar milling step. The contact pads are thicker than the milling depth of the Ar etch step, thus providing a sufficiently large conducting area that is accessible for further lithographic connection with bond pads. We suggest that this approach can be successfully applied to fabricate samples suitable for current-induced spin dynamics.

## 5.5. Further material optimization

Even though the dynamics induced by spin-polarized currents seems more relevant for applications, a large variety of fundamental questions may still be addressed by the investigation of the dynamics induced by magnetic field pulses. In particular, the CoB/Pt material used for the experiments presented in this thesis is still not ideal. In fact, it is very difficult to prepare a sample in which a magnetic bubble can be placed in a pinning potential that is strong enough to ensure that the system relaxes always to the same configuration and at the same time shallow enough to permit the observation of a sizable motion of the bubble within the potential. This is mainly because the fabrication of such a sample still has some non-deterministic components since the existence of such a pinning potential relies on local disorder. In view of applications, but also for a systematic study of the gyration of a skyrmionic spin structure, it would be desirable to further reduce the magnetic pinning within the material and to introduce the potential energy for the restoring force controllably by nanostructuring the magnetic element. Suitable materials for such investigations might be those with Dzyaloshinskii-Moriya interaction, in which highly regular lattices of chiral Skyrmions have been observed (such as MnSi,<sup>6</sup>  $\text{Fe}_x\text{Co}_{1-x}\text{Si}$ ,<sup>7</sup> FeGe,<sup>131</sup> and ultrathin Fe on Ir<sup>140</sup>), but also the extremely optimized bubble materials used in the research and in the applications of bubble media in the second half of the 20th century, in particular YIG.<sup>18,32</sup> The most significant hindrance for using such materials is that they all require epitaxial growth, which could not so far be realized on amorphous SiN membrane substrates. To enable the investigation of the dynamics in such materials using x-ray holography, the fabrication of suitable single crystal substrates of at most a few micrometer thickness must become well under control. Further thinning in the area of the object and reference holes is then feasible using a focused ion beam. The investigation of YIG is particularly interesting because of the low Gilbert damping in this material, promising the observation of a gyration with a large number of cycles before full damping.

## 5.6. Conclusions

To summarize, although the present work constitutes an important contribution to the understanding of the dynamics of topological structures, in particular in magnetism, a number of new questions have arisen that merit a closer attention. A selection has been listed above. The tools provided in this thesis are expected to pave the way for addressing some of these exciting challenges. The results can be expected to provide new insights into the behavior of Skyrmions in magnetism and to contribute to their possible application in commercial devices.



# Chapter 6

## Conclusions and outlook

---

In this thesis, we have investigated the magnetic field induced GHz dynamics of magnetic Skyrmions. The investigation of the GHz Skyrmion dynamics was made possible by two milestone developments during this thesis, which are, to a large extend, generic and applicable to other pump-probe dynamical studies with x-ray holography, in particular to magnetic imaging experiments in high-anisotropy materials.

In a first important step, we have optimized the magnetic material and its structuring with regards to magnetic pinning to enable the billion-fold reproduction of the same excitation of a Skyrmion under identical initial conditions. We have shown that CoB/Pt materials are well suited for such studies because they exhibit sufficiently extended areas in which the local energy barriers of magnetic pinning sites are well below the thermal energy  $k_B T$ . In such areas, thermally activated (stochastic) events during the motion of domain walls are effectively eliminated. We note that the absence of strong energy barriers does not lead to thermal fluctuations of the spin structures because relaxed spin configurations are stabilized by magnetostatic forces. On the structuring side, we have seen that Ar milling should be used instead of standard lift-off processes to define the magnetic nanostructures and we have optimized the process to work at temperatures below 120 °C to avoid inducing permanent structural and magnetic changes in the sample that might lead to a loss of out-of-plane magnetic signal.

Our second important achievement was the design and optimization of a suitable x-ray holographic experimental setup (including the integrated sample design) to provide the performance required for the acquisition of several hundred images in the low-intensity single bunch mode. In this context, we have developed a sample fabrication process that can be automated and that is therefore suitable for the production of samples with acceptably low human workload. We have shown that these samples permit the acquisition of x-ray holograms without using a beamstop, facilitating the fully automatic reconstruction of magnetic images with very high quality.

Using these novel developments in the material and our pump-probe extension of x-ray holography, we have imaged the trajectory of a magnetic Skyrmion in the

GHz regime, where we have observed a spiraling motion as predicted by Thiele.<sup>27</sup> However, the sense of rotation and the detailed trajectory could not be explained by the first order differential equation of motion suggested in that work. We have shown that a second order term must be included in the equation to properly describe the experimental observations. The coefficient of this second order term can be seen as an inertial mass, and we have found that the mass density of a magnetic Skyrmion is significantly larger than in any other magnetic system investigated thus far. We attribute the presence of inertia in Skyrmions to the energy associated with a deformation of the Skyrmion shape. We have argued that all (meta-)stable Skyrmions (not only in magnetism) are confined structures with a well-defined shape in the ground state. It is natural to assume that the deformation of the Skyrmion shape always requires energy, and that therefore all Skyrmions are massive particles. In our model, the particularly large mass found in magnetic Skyrmions is attributed to the strong dipolar energy that is a function of the area of the Skyrmion and not only of its circumference.

Our observations are a first step towards an understanding of the high-frequency dynamics that emerge from the topological identity of magnetic Skyrmions. Further studies are required — and, with our technological developments, now addressable — to obtain a comprehensive knowledge about phenomena at this technologically relevant nanosecond timescale. Namely, our quasiparticle model is a major step towards making systems of many Skyrmions computationally accessible, because it promises to reduce the number of cells required to approximate a Skyrmion from more than 500 in the micromagnetic approach to just one. To enable such a simplified computation, however, it is desirable to (i) determine the pair interaction Lagrangian for magnetic Skyrmions (as, for instance, suggested in Ref. 128) and (ii) to predict their mass quantitatively. The latter calls for a study of the Skyrmion mass as a function of its radius (tunable by the external field), of the material properties, and, to confirm the quasiparticle model, of the local magnetic environment and the excitation used (for an accurate quasiparticle description, the Skyrmion mass should depend neither on dynamically changing properties such as the presence of other Skyrmions nor on the means of excitation, e.g., spin-polarized currents or magnetic fields). At least part of such a study should be carried out using imaging, since this is the only tool that can probe the behavior of an individual Skyrmion in the presence of several others.

Skyrmions are facing tremendous interest these days,<sup>125,126,141</sup> which is to a significant extent motivated by the perspective to use these objects in novel (e.g., racetrack type) data storage devices. Due to the small size of these objects (down to the atomic scale<sup>140</sup>), their remarkable stability<sup>6</sup> in particular in thin films with Dzyaloshinskii-Moriya interaction,<sup>140</sup> and due to their ultra low sensitivity to pinning found recently,<sup>9,142</sup> such an application seems particularly realistic in the case of Skyrmions.<sup>126</sup> The next milestone development on the way towards

Skyrmion racetrack memories,<sup>126</sup> in particular after the recently found scheme of controlled Skyrmion creation and annihilation,<sup>141</sup> would be the controlled displacement of single Skyrmions by spin-polarized currents. As we have argued in chapter 5, the knowledge about the resonance frequencies of Skyrmions should facilitate the Skyrmion motion at reasonably low current densities.<sup>139</sup> Direct imaging measurements would show details about the 2D motion of the Skyrmion as well as about deformations. Such information is relevant for the optimization of the magnetic materials as well as of the excitation scheme, and with our pump-probe imaging technique, it is readily accessible.



# Appendices

---

## A. Transverse anisotropy and Döring mass density of perpendicular magnetic multilayers

Multilayers with perpendicular magnetic anisotropy (PMA) are widely used in research as well as in applications. From a theoretical point of view, however, multilayers are very difficult systems to model because of the structural discontinuities along the out-of-plane direction (here taken as the  $z$ -direction) and their effects on the other relevant observables. Many published studies neglect these discontinuities and use simplified models that consider the film to be homogeneous with average or effective magnetic parameters. Such approximations are reasonably accurate for local quantities such as the crystal anisotropy or the exchange coupling, whereas the calculation of non-local quantities such as the magnetostatic energy might be wrong by orders of magnitude. Here, we present rigorous calculations of the magnetostatic energy of a multilayer system with a domain wall, from which we obtain the most relevant parameters for magnetic domain wall motion: the transverse anisotropy constant  $K_{\perp}$  and the Döring mass density  $m_D$  as a function of the thickness of a single magnetic layer  $\mathcal{T}$ , the multilayer periodicity  $\mathcal{P}$ , the number of repeats  $\mathcal{N}$ , the static domain wall width  $\Delta_0$ , and the effective out-of-plane anisotropy constant  $K_{u,\text{eff}}$  (in units of  $\mu_0 M_s^2$  where  $M_s$  is the saturation magnetization).

Both the perpendicular anisotropy constant and the Döring mass density are parameters of the one dimensional (1D) model, and the following calculations are therefore based on this model, which assumes a single domain wall with the magnetization profile

$$M_x(x) = M_s \cosh^{-1}(x/\Delta) \sin(\psi) \quad (\text{A.1})$$

$$M_y(x) = M_s \cosh^{-1}(x/\Delta) \cos(\psi) \quad (\text{A.2})$$

$$M_z(x) = M_s \tanh(x/\Delta). \quad (\text{A.3})$$

Here,  $\mathbf{M} = (M_x, M_y, M_z)$  is the local magnetization,  $M_s = |\mathbf{M}|$  is the saturation magnetization,  $\Delta = \Delta(\psi)$  is the domain wall width parameter, and  $\psi$  is the

transverse (domain wall) angle. The magnetization is homogeneous along the wall, i.e., it does not depend on  $y$  and  $z$ . The energy density of such a domain wall per unit area can be described as a transverse domain wall anisotropy energy  $\sigma_{K,DW}$  with leading order anisotropy constant  $K_\perp$ :

$$\sigma_{K,DW}(\psi) = C + K_\perp \int dx \sin^2 \theta \sin^2 \psi + \mathcal{O}(\sin^4 \psi) \quad (\text{A.4})$$

$$= C + 2\Delta_0 K_\perp \sin^2 \psi + \mathcal{O}(\sin^4 \psi), \quad (\text{A.5})$$

where  $C$  does not depend on  $\psi$ . Here, we will calculate the effective transverse anisotropy constant that is associated with the magnetostatic energy of a domain wall, that is, we will calculate the magnetostatic energy per unit domain wall area  $\sigma_d$  and expand this energy in a Taylor series of  $s := \sin^2 \psi$ ,

$$\sigma_d(\psi) = \sigma_d(s=0) + s \left. \frac{d\sigma_d}{ds} \right|_{s=0} + \mathcal{O}(s^2). \quad (\text{A.6})$$

At this stage, it is worth noting that

$$\left. \frac{d\sigma_d}{ds} \right|_{s=0} = \left. \frac{\partial \sigma_d}{\partial s} \right|_{s=0} + \left. \frac{\partial \sigma_d}{\partial \Delta} \right|_{\Delta=\Delta_0} \left. \frac{d\Delta}{ds} \right|_{s=0} = \left. \frac{\partial \sigma_d}{\partial s} \right|_{s=0}, \quad (\text{A.7})$$

because the slope of the energy with respect to  $\Delta$  vanishes at equilibrium  $\Delta = \Delta_0$ . We therefore can obtain  $K_\perp$  from  $\sigma_{K,DW} = \sigma_d$ :

$$K_\perp = \left. \frac{\partial \sigma_d}{\partial s} \right|_{s=0} \frac{1}{(2\Delta_0)}. \quad (\text{A.8})$$

For small transverse angles  $\psi$ , higher order terms can be neglected. In particular, the domain wall mass is defined in this small angle approximation, which is assumed here as well.

In the following, we consider a thin film multilayer system that is infinite in the in-plane directions  $x$  and  $y$ . In reality, our results are applicable to any system in which this lateral extend is much larger than the domain wall width, which is valid for almost all PMA systems studied today. As in the 1D model, we will assume the presence of a single domain wall in the  $y$ - $z$ -plane at  $x = 0$ . However, now we have the additional  $z$ -dependency of the multilayer, which we describe as a sum over single layers expressed via the layer function  $l(z)$ , which is one if  $0 \leq z \leq \mathcal{T}$  and zero otherwise:

$$M_x(x, z) = M_x(x) \sum_{j=0}^{\mathcal{N}-1} l(z - j\mathcal{P}) \quad (\text{A.9})$$

$$M_y(x, z) = M_y(x) \sum_{j=0}^{\mathcal{N}-1} l(z - j\mathcal{P}) \quad (\text{A.10})$$

$$M_z(x, z) = M_z(x) \sum_{j=0}^{\mathcal{N}-1} l(z - j\mathcal{P}) \quad (\text{A.11})$$

with

$$l(z) = \theta(\mathcal{T}/2 - |z - \mathcal{T}/2|). \quad (\text{A.12})$$

The magnetostatic energy of a magnetization configuration  $\mathbf{M}(\mathbf{r})$  per unit domain wall area reads

$$\sigma_d(\psi) = \frac{\mu_0}{8\pi\mathcal{W}\mathcal{N}\mathcal{T}} \iint d^3\mathbf{r} d^3\mathbf{r}' \rho(\mathbf{r}) \rho(\mathbf{r}') \frac{1}{|\mathbf{r} - \mathbf{r}'|}, \quad (\text{A.13})$$

where  $\rho$  is the volume density of magnetic charges,  $\mathcal{W}$  is the width of the structure ( $y$ -direction) and  $\mathcal{N}\mathcal{T}$  is its total thickness of the magnetic material ( $z$ -direction). Magnetic charges arise from the divergence of the magnetization inside the volume (volume charges) and from the components of the magnetization perpendicular to the surfaces of the structure (surface charges). To wit,

$$\rho(\mathbf{r}) = \sum_{j=0}^{\mathcal{N}-1} \rho_1(x, z - j\mathcal{P}), \quad (\text{A.14})$$

$$\rho_1(x, z) = \rho_S(x) [-\delta(z) + \delta(z - \mathcal{T})] + \rho_V(x) l(z), \quad (\text{A.15})$$

$$\rho_S(x) = M_z(x) = M_s \tanh(x/\Delta), \quad (\text{A.16})$$

$$\rho_V(x) = -\text{div } \mathbf{M} = \frac{M_s}{\Delta} \sin(\psi) \frac{\tanh(x/\Delta)}{\cosh(x/\Delta)}. \quad (\text{A.17})$$

The interactions of the surface stray fields with the volume charges vanish when averaged over  $z$  for symmetry reasons, and we can therefore calculate the magnetostatic energy density of the volume charges  $\sigma_{d,V}$  and the magnetostatic energy density of the surface charges  $\sigma_{d,S}$  independently. The sum of these terms yields  $\sigma_d$ . We note, however, that only the volume charges have an explicit  $s$ -dependence. According to Eq. (A.8), the energy due to the volume charges is therefore the only term that needs to be considered in the following.

Before we solve the integrals for the energy of the volume charges explicitly, we will first simplify the general form of the stray field integral Eq. (A.13). The kernel of the double sum in the integral

$$\sigma_d = \frac{\mu_0}{8\pi\mathcal{W}\mathcal{N}\mathcal{T}} \iint d^3\mathbf{r} d^3\mathbf{r}' \sum_{i,j=0}^{\mathcal{N}-1} \rho_1(x, z - i\mathcal{P}) \rho_1(x', z' - j\mathcal{P}) \frac{1}{|\mathbf{r} - \mathbf{r}'|} \quad (\text{A.18})$$

$$= \frac{\mu_0}{8\pi\mathcal{W}\mathcal{N}\mathcal{T}} \iint d^3\mathbf{r} d^3\mathbf{r}' \rho_1(x, z) \rho_1(x', z') \sum_{i,j=0}^{\mathcal{N}-1} \frac{1}{|\mathbf{r} + i\mathcal{P}\mathbf{e}_z - \mathbf{r}' - j\mathcal{P}\mathbf{e}_z|} \quad (\text{A.19})$$

depends on  $i$  and  $j$  only in the form  $i - j$ . That is, we can reorder the double sum

to just one over this difference  $(i - j) = (-\mathcal{N} + 1), \dots, \mathcal{N} - 1$  (which we will index again by  $j$ ) and a factor  $\mathcal{N} - |j|$  that counts how often the term  $j$  is represented in the original sum:

$$\sigma_d = \frac{\mu_0}{8\pi\mathcal{W}\mathcal{N}\mathcal{T}} \iint d^3\mathbf{r} d^3\mathbf{r}' \rho_1(x, z) \rho_1(x', z') \sum_{j=-\mathcal{N}+1}^{\mathcal{N}-1} \frac{(\mathcal{N} - |j|)}{|\mathbf{r} - \mathbf{r}' + j\mathcal{P}\mathbf{e}_z|}. \quad (\text{A.20})$$

Furthermore, we can easily solve the integration with respect to  $y$  and  $y'$ , because the charge densities do not depend on these coordinates, giving

$$\sigma_d = \frac{\mu_0}{8\pi\mathcal{N}\mathcal{T}} \iiint dx dx' dz dz' \rho_1(x, z) \rho_1(x', z') \quad (\text{A.21})$$

$$\times \sum_{j=-\mathcal{N}+1}^{\mathcal{N}-1} (\mathcal{N} - |j|) h_{\mathcal{W}}(x - x', z - z' + j\mathcal{P}), \quad (\text{A.22})$$

$$h_{\mathcal{W}}(x, z) = \frac{1}{\mathcal{W}} \iint dy dy' \left[ \frac{1}{\sqrt{(y - y')^2 + x^2 + z^2}} \right] \quad (\text{A.23})$$

$$= 2 \log(2\mathcal{W}) - \log(x^2 + z^2) + \mathcal{O}(\mathcal{W}^{-1}). \quad (\text{A.24})$$

The steps to solve the integral Eq. (A.23) are discussed in detail in section A.1. The term  $2 \log(2\mathcal{W})$  does not depend on  $x$ , and without the presence of another  $x$ -dependent term, the integral of  $\rho_1(x)$  over  $x$  vanishes because the magnetic charges are antisymmetric in  $x$ . That is, in the limit  $\mathcal{W} \rightarrow \infty$ , the general form of the stray field energy of a domain wall reads

$$\sigma_d = \frac{\mu_0}{8\pi\mathcal{N}\mathcal{T}} \sum_{j=-\mathcal{N}+1}^{\mathcal{N}-1} (\mathcal{N} - |j|) \iiint dx dx' dz dz' \quad (\text{A.25})$$

$$\times \rho_1(x, z) \rho_1(x', z') h(x - x', z - z' + j\mathcal{P}), \quad (\text{A.26})$$

$$h(x, z) = -\log(x^2 + z^2). \quad (\text{A.27})$$

As outlined in section A.1, the double integral over  $x$  and  $x'$  can be reduced to a single integral in Fourier space (here, the hat denotes a Fourier transform with respect to the  $x$ -coordinate):

$$\sigma_d = \frac{\mu_0 \sqrt{2\pi}}{8\pi\mathcal{N}\mathcal{T}} \sum_{j=-\mathcal{N}+1}^{\mathcal{N}-1} (\mathcal{N} - |j|) \iint dz dz' \quad (\text{A.28})$$

$$\times \int dk \hat{\rho}_1(k, z) (\hat{\rho}_1(k, z'))^* \hat{h}(k, z - z' + j\mathcal{P}),$$

$$\hat{h}(k, z) = \sqrt{2\pi} \frac{1}{|k|} e^{-|zk|}. \quad (\text{A.29})$$

To solve these integrals, we have to specify what  $\rho_1(x, z)$  is. We will continue the discussion with the explicit form of the volume charges.



The volume charge density, given in Eq. (A.17), is proportional to  $\sqrt{s}$ . The volume stray field energy is therefore linear in  $s$ . The first order partial derivative of the stray field energy density of the volume charges with respect to  $s$ ,  $\sigma_{d,V}^{(1)}$ , thus reads

$$\sigma_{d,V}^{(1)} = \frac{\mu_0 M_s^2 \sqrt{2\pi}}{8\pi \mathcal{N} \mathcal{T}} \sum_{j=-\mathcal{N}+1}^{\mathcal{N}-1} (\mathcal{N} - |j|) \int_0^{\mathcal{T}} dz \int_0^{\mathcal{T}} dz' \quad (\text{A.30})$$

$$\times \int dk |\hat{\varsigma}_1(k)|^2 \hat{h}(k, z - z' + j\mathcal{P}),$$

$$\varsigma_1(x) = \frac{1}{\Delta_0} \frac{\tanh(x/\Delta_0)}{\cosh(x/\Delta_0)}, \quad (\text{A.31})$$

$$\hat{\varsigma}_1(k) = ik\Delta_0 \sqrt{\frac{\pi}{2}} \frac{1}{\cosh\left(\frac{\pi\Delta_0 k}{2}\right)}. \quad (\text{A.32})$$

Here, we have included the  $z$ -dependent part of the magnetic charge density in the integration limits. We first perform the  $z$  and  $z'$  integration to obtain:

$$\int_0^{\mathcal{T}} dz \int_0^{\mathcal{T}} dz' \hat{h}(k, z - z' + j\mathcal{P}) \quad (\text{A.33})$$

$$= \frac{\sqrt{2\pi}}{|k|} \int_0^{\mathcal{T}} dz \int_0^{\mathcal{T}} dz' e^{-|z-z'+j\mathcal{P}||k|} \quad (\text{A.34})$$

$$= \frac{\sqrt{2\pi}}{|k|} \int_0^{\mathcal{T}} dz \int_{z+j\mathcal{P}-\mathcal{T}}^{z+j\mathcal{P}} dz' e^{-|z'||k|} \quad (\text{A.35})$$

$$= -\frac{\sqrt{2\pi}}{k^2} \int_0^{\mathcal{T}} dz \begin{cases} e^{(z+j\mathcal{P}-\mathcal{T})|k|} - e^{(z+j\mathcal{P})|k|} & z + j\mathcal{P} \leq 0 \\ -e^{-(z+j\mathcal{P}-\mathcal{T})|k|} + e^{-(z+j\mathcal{P})|k|} & z + j\mathcal{P} - \mathcal{T} \geq 0 \\ e^{(z+j\mathcal{P}-\mathcal{T})|k|} + e^{-(z+j\mathcal{P})|k|} - 2 & \text{else} \end{cases} \quad (\text{A.36})$$

$$= -\frac{\sqrt{2\pi}}{k^2} \int_0^{\mathcal{T}} dz \begin{cases} e^{(z+j\mathcal{P}-\mathcal{T})|k|} - e^{(z+j\mathcal{P})|k|} & j < 0 \\ -e^{-(z+j\mathcal{P}-\mathcal{T})|k|} + e^{-(z+j\mathcal{P})|k|} & j > 0 \\ e^{(z-\mathcal{T})|k|} + e^{-z|k|} - 2 & j = 0 \end{cases} \quad (\text{A.37})$$

$$= -\frac{\sqrt{2\pi}}{k^2} \begin{cases} |k|^{-1} (2e^{j\mathcal{P}|k|} - e^{(j\mathcal{P}-\mathcal{T})|k|} - e^{(\mathcal{T}+j\mathcal{P})|k|}) & j < 0 \\ |k|^{-1} (2e^{-j\mathcal{P}|k|} - e^{-(j\mathcal{P}-\mathcal{T})|k|} - e^{-(\mathcal{T}+j\mathcal{P})|k|}) & j > 0 \\ 2\frac{1-e^{-\mathcal{T}|k|}}{|k|} - 2\mathcal{T} & j = 0 \end{cases} \quad (\text{A.38})$$

$$= -\frac{\sqrt{2\pi}}{k^2} \begin{cases} |k|^{-1} (2e^{-|j|\mathcal{P}|k|} - e^{-(|j|\mathcal{P}-\mathcal{T})|k|} - e^{-(\mathcal{T}+|j|\mathcal{P})|k|}) & j \neq 0 \\ 2\frac{1-e^{-\mathcal{T}|k|}}{|k|} - 2\mathcal{T} & j = 0 \end{cases} \quad (\text{A.39})$$

With this expression, Eq. (A.30) reads

$$\sigma_{d,V}^{(1)} = -\frac{\mu_0 M_s^2}{8\pi\mathcal{T}} \Delta_0^2 \frac{\pi}{2} (2\pi) 2 \int_0^\infty dk \frac{1}{\cosh^2\left(\frac{\pi\Delta_0 k}{2}\right)} \quad (\text{A.40})$$

$$\times \left( -2\mathcal{T} + 2 \frac{1 - e^{-\mathcal{T}k}}{k} + 2 \sum_{j=1}^{\mathcal{N}-1} \frac{\mathcal{N}-j}{\mathcal{N}k} \left( 2e^{-j\mathcal{P}k} - e^{-(j\mathcal{P}-\mathcal{T})k} - e^{-(j\mathcal{P}+\mathcal{T})k} \right) \right).$$

We substitute  $q := 2\pi\Delta_0 k$ ,  $a = \frac{\mathcal{P}}{2\pi\Delta_0}$ , and  $b = \frac{\mathcal{T}}{2\pi\Delta_0}$  to obtain

$$\sigma_{d,V}^{(1)} = \frac{\mu_0 M_s^2}{4\sqrt{2\pi}b} \Delta_0 \int_0^\infty dq \frac{1}{\cosh^2(q/4)} \quad (\text{A.41})$$

$$\times \left( b - \frac{1 - e^{-bq}}{q} - \sum_{j=1}^{\mathcal{N}-1} \frac{\mathcal{N}-j}{\mathcal{N}q} \left( 2e^{-jaq} - e^{-(ja-b)q} - e^{-(ja+b)q} \right) \right)$$

This is a sum of the basic integrals

$$\int_0^\infty dq \frac{1}{\cosh^2(q/4)} = 4, \quad (\text{A.42})$$

$$\int_0^\infty dq \frac{1 - e^{-xq}}{q \cosh^2(q/4)} =: F(x) \quad (\text{A.43})$$

with

$$F(x) = 8\zeta^{(1,0)}(-1, x+1) - 8\zeta^{(1,0)}\left(-1, x + \frac{3}{2}\right) + 12\log(A) + 4\log(2x+1) \quad (\text{A.44})$$

$$- 4x(2x+1) \left( \gamma_1\left(x + \frac{1}{2}\right) - \gamma_1\left(x + \frac{3}{2}\right) \right) - 8x \log\left( \frac{\Gamma\left(x + \frac{1}{2}\right) \Gamma(x+1)}{\Gamma\left(x + \frac{3}{2}\right)^2} \right)$$

$$- 1 - \frac{1}{3}13\log(2),$$

where  $\zeta^{(1,0)}$  is the partial derivative of the Hurwitz Zeta function with respect to its first argument,  $\gamma_1(x)$  is the first generalized Stieltjes coefficient,  $\Gamma$  is the Gamma function, and  $A$  is the Glaisher constant. The final result reads

$$\sigma_{d,V}^{(1)} = C_V \left( 4b - F(b) + \sum_{j=1}^{\mathcal{N}-1} \frac{\mathcal{N}-j}{\mathcal{N}} (2F(aj) - F(aj-b) - F(aj+b)) \right), \quad (\text{A.45})$$

$$C_V = \frac{\Delta_0 \mu_0 M_s^2}{4b}. \quad (\text{A.46})$$

For  $x < 1$ , the function  $F(x)$  can be well approximated by (relative deviation

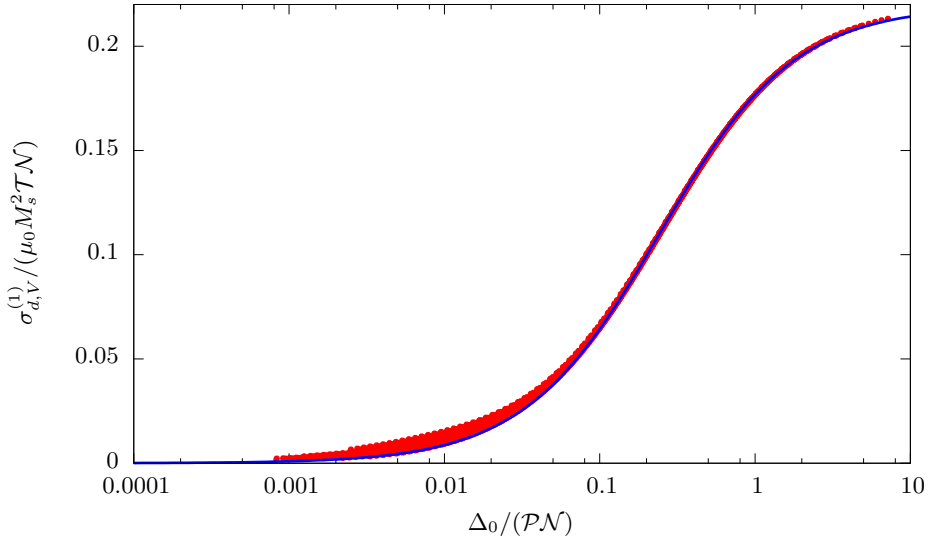


**Figure A.1 | First order coefficient  $\sigma_{d,V}^{(1)}$  of the areal density of the magnetostatic energy of the volume charges of a domain wall in a multilayer system.** The calculated parameter  $\sigma_{d,V}^{(1)}$  is plotted with red points as a function of domain wall width  $\Delta_0$ , single layer thickness  $\mathcal{T}$ , layer periodicity  $\mathcal{P}$ , and total number of layers  $\mathcal{N}$ . If normalized to the total thickness of the magnetic material  $\mathcal{T}\mathcal{N}$  and to the magnetostatic energy  $\mu_0 M_s^2$ , the energy  $\sigma_{d,V}^{(1)}$  is a function  $\Delta_0$  normalized to the total multilayer thickness  $\mathcal{P}\mathcal{N}$  alone. The blue solid line is a fit to the calculated data, and this fit describes the calculated energies for a single layer  $\mathcal{N} = 1$  precisely.

$< 1 \%$ )

$$F(x) \approx 4x - 4.86x^2 + 4.21x^3 - 1.56x^4 \quad (\text{A.47})$$

The resulting parameter  $\sigma_{d,V}^{(1)}$  is plotted in Fig. A.1 as a function of  $M_s$ ,  $\Delta_0$ ,  $\mathcal{T}$ ,  $\mathcal{P}$ , and  $\mathcal{N}$ . We find that this hyper-dimensional function can be very well approximated by a simple single-dimensional dependency:

$$\sigma_{d,V}^{(1)}(M_s, \Delta_0, \mathcal{T}, \mathcal{P}, \mathcal{N}) = \mu_0 M_s^2 \mathcal{T} \mathcal{N} \Xi(\Delta_0 / (\mathcal{P} \mathcal{N})), \quad (\text{A.48})$$

where we find that the single-parameter function  $\Xi$  can be well approximated by a hyperbolic tangent function. Only for  $\Delta_0 / (\mathcal{P} \mathcal{N}) \ll 0.1$ , a small deviation from this single parameter dependency becomes visible. That is, for most multilayer systems investigated today, the energy density associated with the volume charges of a domain wall can be calculated analytically through

$$\sigma_{d,V}^{(1)} = 0.11 \mu_0 M_s^2 \mathcal{T} \mathcal{N} (1 + \tanh(0.5 \log(4.15 \Delta_0 / (\mathcal{P} \mathcal{N}))))). \quad (\text{A.49})$$

For the material investigated in this thesis, we have  $\mathcal{N} = 30$ ,  $\mathcal{T} = 0.4 \text{ nm}$ ,  $\mathcal{P} = 1.1 \text{ nm}$ , and  $\Delta_0 = 11 \text{ nm}$  and thus  $\sigma_{d,V}^{(1)} = 0.139 \Delta_0 \mu_0 M_s^2$ . From this, we obtain  $K_{\perp} = 0.09(1) \mu_0 M_s^2$ , where the error bar includes the uncertainty of the

value of  $\Delta_0$  and takes into account that, potentially, some (less than 10) of the  $\mathcal{N} = 30$  magnetic layers are tilted in-plane to form flux closure domains. This value for the perpendicular anisotropy constant corresponds to a Döring mass density of  $m_D = 3.5(8) \times 10^{-8} \text{ kg/m}^2$ .

## A.1. Calculations

This section contains a selection of useful identities that we have used in the main text, but which require lengthy calculations. We start with a typical double integral over a pair interaction kernel, which we can reduce to a single integral in Fourier space (assuming real-valued functions):

$$\int dx dx' f(x) h(x') g(x - x') = \int dx f(x) \int dx' g(x - x') h(x') \quad (\text{A.50})$$

$$= \int dx f(x) (h * g)(x) \quad (\text{A.51})$$

$$= \int dx f(x) \frac{1}{\sqrt{2\pi}} \int dk \hat{h}(k) \hat{g}(k) e^{-ikx} \quad (\text{A.52})$$

$$= \int dk \hat{h}(k) \hat{g}(k) \frac{1}{\sqrt{2\pi}} \int dx f(x) e^{-ikx} \quad (\text{A.53})$$

$$= \int dk \hat{h}(k) \hat{g}(k) \left( \hat{f}(k) \right)^* \quad (\text{A.54})$$

Note that we are using the following definition of the Fourier transform:

$$\hat{f}(k) = \frac{1}{\sqrt{2\pi}} \int dx f(x) e^{ikx} \quad (\text{A.55})$$

$$f(x) = \frac{1}{\sqrt{2\pi}} \int dk \hat{f}(k) e^{-ikx} \quad (\text{A.56})$$

Next, we will calculate the integral

$$\frac{1}{\mathcal{W}} \int_0^{\mathcal{W}} dy \int_0^{\mathcal{W}} dy' \frac{1}{\sqrt{(y - y')^2 + a}} \quad (\text{A.57})$$

for large  $\mathcal{W}$ . The integration with respect to  $y'$  yields

$$\int_0^{\mathcal{W}} dy' \frac{1}{\sqrt{(y - y')^2 + a}} \quad (\text{A.58})$$

$$= -\log \left( \sqrt{(y - y')^2 + a} + y - y' \right) \Big|_{y'=0}^{\mathcal{W}} \quad (\text{A.59})$$

$$= -\log \left( \sqrt{(y - \mathcal{W})^2 + a} + y - \mathcal{W} \right) + \log \left( \sqrt{y^2 + a} + y \right). \quad (\text{A.60})$$

The normalized integration of each of these sum terms with respect to  $y$  then reads

$$\frac{1}{\mathcal{W}} \int_0^{\mathcal{W}} dy \log \left( \sqrt{(y - \mathcal{W})^2 + a} + y - \mathcal{W} \right) \quad (\text{A.61})$$

$$= \frac{1}{\mathcal{W}} \left[ (y - \mathcal{W}) \log(\sqrt{a + (y - \mathcal{W})^2} + y - \mathcal{W}) - \sqrt{a + (y - \mathcal{W})^2} \right]_{y=0}^{\mathcal{W}} \quad (\text{A.62})$$

$$= -\sqrt{a/\mathcal{W}^2} + \log((\sqrt{a/\mathcal{W}^2 + 1} - 1)\mathcal{W}) + \sqrt{a/\mathcal{W}^2 + 1} \quad (\text{A.63})$$

$$= \log(a/(2\mathcal{W})) + \mathcal{O}(\mathcal{W}^{-1}) = -\log(2\mathcal{W}) + \log(a) + \mathcal{O}(\mathcal{W}^{-1}) \quad (\text{A.64})$$

and

$$\frac{1}{\mathcal{W}} \int_0^{\mathcal{W}} dy \log \left( \sqrt{y^2 + a^2} + y \right) \quad (\text{A.65})$$

$$= \frac{1}{\mathcal{W}} \left[ y \log(\sqrt{a + y^2} + y) - \sqrt{a + y^2} \right]_{y=0}^{\mathcal{W}} \quad (\text{A.66})$$

$$= \log(\sqrt{a + \mathcal{W}^2} + \mathcal{W}) - \sqrt{a/\mathcal{W}^2 + 1} + \sqrt{a/\mathcal{W}^2} \quad (\text{A.67})$$

$$= \log((2 + a/(2\mathcal{W}^2))\mathcal{W}) + \mathcal{O}(\mathcal{W}^{-1}) \quad (\text{A.68})$$

$$= \log(2\mathcal{W}) + \mathcal{O}(\mathcal{W}^{-1}). \quad (\text{A.69})$$

Hence,

$$\frac{1}{\mathcal{W}} \int_0^{\mathcal{W}} dy \int_0^{\mathcal{W}} dy' \frac{1}{\sqrt{(y - y')^2 + a^2}} = 2 \log(2\mathcal{W}) - \log(a) + \mathcal{O}(\mathcal{W}^{-1}). \quad (\text{A.70})$$

## B. Solution of the bubble equation of motion

The equation of motion for a single bubble in a parabolic potential reads

$$-M\ddot{\mathbf{R}} + \mathbf{G} \times \dot{\mathbf{R}} + D\dot{\mathbf{R}} - K\mathbf{R} = 0. \quad (\text{B.1})$$

By using  $\mathbf{R} = (X, Y, Z = 0)$  and the convenient 2D parametrization  $\bar{R} = X + iY$ , we obtain

$$-M\ddot{\bar{R}} + (D + iG)\dot{\bar{R}} - K\bar{R} = 0, \quad (\text{B.2})$$

which is a simple harmonic oscillator with solution

$$\bar{R}(t) = A \exp(i\bar{\omega}_1 t) + B \exp(i\bar{\omega}_2 t) \quad (\text{B.3})$$

with

$$\bar{\omega}_{1,2} = i\bar{\eta} \pm \sqrt{\omega_0^2 - \bar{\eta}^2}, \quad (\text{B.4})$$

$$\bar{\eta} = -\frac{1}{2M}(D + iG), \quad (\text{B.5})$$

$$\omega_0 = \sqrt{K/M}. \quad (\text{B.6})$$

The complex frequencies  $\bar{\omega}_{1,2} = \omega_{1,2} + i/\tau$  are measured in the experiment. To extract the mass parameter, we use the sum of the real frequencies:

$$\omega_1 + \omega_2 = \text{Re}(\bar{\omega}_1 + \bar{\omega}_2) \quad (\text{B.7})$$

$$= \text{Re}(G/M - iD/M) \quad (\text{B.8})$$

$$= G/M. \quad (\text{B.9})$$

# Bibliography

---

- [1] M. Z. Hasan and C. L. Kane. Colloquium: Topological insulators. *Reviews of Modern Physics* **82**, 3045 (2010). doi:10.1103/RevModPhys.82.3045.
- [2] C. Moutafis, S. Komineas, and J. A. C. Bland. Dynamics and switching processes for magnetic bubbles in nanoelements. *Physical Review B* **79**, 224429 (2009). doi:10.1103/PhysRevB.79.224429.
- [3] M. Mochizuki. Spin-wave modes and their intense excitation effects in skyrmion crystals. *Physical Review Letters* **108**, 017601 (2012). doi:10.1103/PhysRevLett.108.017601.
- [4] U. K. Rößler, A. N. Bogdanov, and C. Pfleiderer. Spontaneous skyrmion ground states in magnetic metals. *Nature* **442**, 797 (2006). doi:10.1038/nature05056.
- [5] C. Moutafis *et al.* Magnetic bubbles in FePt nanodots with perpendicular anisotropy. *Physical Review B* **76**, 104426 (2007). doi:10.1103/PhysRevB.76.104426.
- [6] S. Mühlbauer *et al.* Skyrmion lattice in a chiral magnet. *Science* **323**, 915 (2009). doi:10.1126/science.1166767.
- [7] X. Z. Yu *et al.* Real-space observation of a two-dimensional skyrmion crystal. *Nature* **465**, 901 (2010). doi:10.1038/nature09124.
- [8] A. Neubauer *et al.* Topological hall effect in the a phase of MnSi. *Physical Review Letters* **102**, 186602 (2009). doi:10.1103/PhysRevLett.102.186602.
- [9] T. Schulz *et al.* Emergent electrodynamics of skyrmions in a chiral magnet. *Nature Physics* **8**, 301 (2012). doi:10.1038/nphys2231.
- [10] S. Komineas. Rotating vortex dipoles in ferromagnets. *Physical Review Letters* **99**, 117202 (2007). doi:10.1103/PhysRevLett.99.117202.
- [11] R. A. Battye, N. R. Cooper, and P. M. Sutcliffe. Stable skyrmions in two-component bose-einstein condensates. *Physical Review Letters* **88**, 080401 (2002). doi:10.1103/PhysRevLett.88.080401.

- 
- [12] J.-Y. Choi, W. J. Kwon, and Y.-i. Shin. Observation of topologically stable 2D skyrmions in an antiferromagnetic spinor bose-einstein condensate. *Physical Review Letters* **108**, 035301 (2012). doi:10.1103/PhysRevLett.108.035301.
- [13] A. Knigavko, and B. Rosenstein. Magnetic skyrmion lattices in heavy fermion superconductor  $\text{UPt}_3$ . *Physical Review Letters* **82**, 1261 (1999). doi:10.1103/PhysRevLett.82.1261.
- [14] T. H. R. Skyrme. A non-linear field theory. *Proceedings of the Royal Society of London. Series A. Mathematical and Physical Sciences* **260**, 127 (1961). doi:10.1098/rspa.1961.0018.
- [15] T. Skyrme. A unified field theory of mesons and baryons. *Nuclear Physics* **31**, 556 (1962). doi:10.1016/0029-5582(62)90775-7.
- [16] B. Piette, B. Schroers, and W. Zakrzewski. Dynamics of baby skyrmions. *Nuclear Physics B* **439**, 205 (1995). doi:10.1016/0550-3213(95)00011-G.
- [17] A. A. Belavin, and A. M. Polyakov. Metastable states of two-dimensional isotropic ferromagnets. *JETP Letters* **22**, 245 (1975).
- [18] A. P. Malozemoff, and J. C. Slonczewski. *Magnetic Domain Walls in Bubble Materials* (Academic Press, New York, 1979).
- [19] O. Tchernyshyov and G.-W. Chern. Fractional vortices and composite domain walls in flat nanomagnets. *Physical Review Letters* **95**, 197204 (2005). doi:10.1103/PhysRevLett.95.197204.
- [20] J. Rhensius *et al.* Imaging of domain wall inertia in permalloy half-ring nanowires by time-resolved photoemission electron microscopy. *Physical Review Letters* **104**, 067201 (2010). doi:10.1103/PhysRevLett.104.067201.
- [21] D. Bedau *et al.* Detection of current-induced resonance of geometrically confined domain walls. *Physical Review Letters* **99**, 146601 (2007). doi:10.1103/PhysRevLett.99.146601.
- [22] L. Thomas, R. Moriya, C. Rettner, and S. S. Parkin. Dynamics of magnetic domain walls under their own inertia. *Science* **330**, 1810 (2010). doi:10.1126/science.1197468.
- [23] J. Slonczewski. Current-driven excitation of magnetic multilayers. *Journal of Magnetism and Magnetic Materials* **159**, L1 (1996). doi:10.1016/0304-8853(96)00062-5.
- [24] L. Berger. Exchange interaction between ferromagnetic domain wall and electric current in very thin metallic films. *Journal of Applied Physics* **55**, 1954 (1984). doi:10.1063/1.333530.



- 
- [25] S. S. P. Parkin, M. Hayashi, and L. Thomas. Magnetic domain-wall racetrack memory. *Science* **320**, 190 (2008). doi:10.1126/science.1145799.
- [26] J. Iwasaki, M. Mochizuki, and N. Nagaosa. Universal current-velocity relation of skyrmion motion in chiral magnets. *Nature Communications* **4**, 1463 (2013). doi:10.1038/ncomms2442.
- [27] A. A. Thiele. Steady-state motion of magnetic domains. *Physical Review Letters* **30**, 230 (1973). doi:10.1103/PhysRevLett.30.230.
- [28] N. Papanicolaou and T. Tomaras. Dynamics of magnetic vortices. *Nuclear Physics B* **360**, 425 (1991). doi:10.1016/0550-3213(91)90410-Y.
- [29] A. Thiaville, Y. Nakatani, J. Miltat, and Y. Suzuki. Micromagnetic understanding of current-driven domain wall motion in patterned nanowires. *EPL (Europhysics Letters)* **69**, 990 (2005). doi:10.1209/epl/i2004-10452-6.
- [30] B. Krüger. *Current-Driven Magnetization Dynamics : Analytical Modeling and Numerical Simulation*. Dissertation, University of Hamburg, Hamburg (2012). [http://ediss.sub.uni-hamburg.de/frontdoor.php?source\\_opus=5887](http://ediss.sub.uni-hamburg.de/frontdoor.php?source_opus=5887).
- [31] I. Makhfudz, B. Krüger, and O. Tchernyshyov. Inertia and chiral edge modes of a skyrmion magnetic bubble. *Physical Review Letters* **109**, 217201 (2012). doi:10.1103/PhysRevLett.109.217201.
- [32] A. H. Bobeck and E. Della Torre. *Magnetic Bubbles*. (North-Holland Publishing Company, Amsterdam, 1975).
- [33] J. Davies, R. Clover, B. Lieberman, and D. Rose. Reliability considerations in the design of one-megabit bubble memory chips. *IEEE Transactions on Magnetics* **16**, 1106 (1980). doi:10.1109/TMAG.1980.1060875.
- [34] M. N. Baibich *et al.* Giant magnetoresistance of (001)Fe/(001)Cr magnetic superlattices. *Physical Review Letters* **61**, 2472 (1988). doi:10.1103/PhysRevLett.61.2472.
- [35] G. Binasch, P. Grünberg, F. Saurenbach, and W. Zinn. Enhanced magnetoresistance in layered magnetic structures with antiferromagnetic interlayer exchange. *Physical Review B* **39**, 4828 (1989). doi:10.1103/PhysRevB.39.4828.
- [36] F. Masuoka, M. Momodomi, Y. Iwata, and R. Shirota. New ultra high density EPROM and flash EEPROM with NAND structure cell. In *Electron Devices Meeting, 1987 International* **33**, 552 (1987).
- [37] O. Boulle, G. Malinowski, and M. Kläui. Current-induced domain wall motion in nanoscale ferromagnetic elements. *Materials Science and Engineering: R: Reports* **72**, 159 (2011). doi:10.1016/j.mser.2011.04.001.

- 
- [38] C. Kooy and U. Enz. Experimental and theoretical study of the domain configuration in thin layers of BaFe<sub>12</sub>O<sub>19</sub>. *Philips Res. Repts.* **15**, 7 (1960).
- [39] C. Kittel. Physical theory of ferromagnetic domains. *Reviews of Modern Physics* **21**, 541 (1949). doi:10.1103/RevModPhys.21.541.
- [40] J. Stöhr and H. C. Siegmann. *Magnetism - From Fundamentals to Nanoscale Dynamics* (Springer-Verlag, Berlin, Heidelberg, 2006).
- [41] J. Stöhr. Exploring the microscopic origin of magnetic anisotropies with x-ray magnetic circular dichroism (XMCD) spectroscopy. *Journal of Magnetism and Magnetic Materials* **200**, 470 (1999). doi:10.1016/S0304-8853(99)00407-2.
- [42] S. Hashimoto, Y. Ochiai, and K. Aso. Perpendicular magnetic anisotropy and magnetostriction of sputtered Co/Pd and Co/Pt multilayered films. *Journal of Applied Physics* **66**, 4909 (1989). doi:10.1063/1.343760.
- [43] B. N. Engel, C. D. England, R. A. Van Leeuwen, M. H. Wiedmann, and C. M. Falco. Interface magnetic anisotropy in epitaxial superlattices. *Physical Review Letters* **67**, 1910 (1991). doi:10.1103/PhysRevLett.67.1910.
- [44] S. Hashimoto, Y. Ochiai, and K. Aso. Perpendicular magnetic anisotropy in sputtered CoPd alloy films. *Japanese Journal of Applied Physics* **28**, 1596 (1989). doi:10.1143/JJAP.28.1596.
- [45] A. Hubert and R. Schäfer. *Magnetic Domains - The Analysis of Magnetic Microstructures* (Springer-Verlag, Berlin, Heidelberg, New York, 1998).
- [46] W. Döring. Über die Trägheit der Wände zwischen Weißchen Bezirken. *Z. Naturforsch. A* **3**, 373 (1948).
- [47] T. McGuire, and R. Potter. Anisotropic magnetoresistance in ferromagnetic 3d alloys. *IEEE Transactions on Magnetics* **11**, 1018 (1975). doi:10.1109/TMAG.1975.1058782.
- [48] T. McGuire, J. Aboaf, and E. Klokholm. Negative anisotropic magnetoresistance in 3d metals and alloys containing iridium. *IEEE Transactions on Magnetics* **20**, 972 (1984). doi:10.1109/TMAG.1984.1063188.
- [49] N. Nagaosa, J. Sinova, S. Onoda, A. H. MacDonald, and N. P. Ong. Anomalous hall effect. *Reviews of Modern Physics* **82**, 1539 (2010). doi:10.1103/RevModPhys.82.1539.
- [50] R. Lavrijsen *et al.* Enhanced field-driven domain-wall motion in Pt/Co<sub>68</sub>B<sub>32</sub>/Pt strips. *Applied Physics Letters* **98**, 132502 (2011). doi:10.1063/1.3571548.

- 
- [51] J. Heinen *et al.* Extraction of the spin torque non-adiabaticity from thermally activated domain wall hopping. *Applied Physics Letters* **99**, 242501 (2011). doi:10.1063/1.3663215.
- [52] B. Dieny. Giant magnetoresistance in spin-valve multilayers. *Journal of Magnetism and Magnetic Materials* **136**, 335 (1994). doi:10.1016/0304-8853(94)00356-4.
- [53] S. S. P. Parkin *et al.* Giant tunnelling magnetoresistance at room temperature with MgO (100) tunnel barriers. *Nature Materials* **3**, 862 (2004). doi:10.1038/nmat1256.
- [54] X. Jiang *et al.* Enhanced stochasticity of domain wall motion in magnetic racetracks due to dynamic pinning. *Nature Communications* **1**, 25 (2010). doi:10.1038/ncomms1024.
- [55] X. Jiang, L. Thomas, R. Moriya, and S. S. P. Parkin. Discrete domain wall positioning due to pinning in current driven motion along nanowires. *Nano Letters* **11**, 96 (2011). doi:10.1021/nl102890h.
- [56] Y. Onose, Y. Okamura, S. Seki, S. Ishiwata, and Y. Tokura. Observation of magnetic excitations of skyrmion crystal in a helimagnetic insulator  $\text{Cu}_2\text{OSeO}_3$ . *Physical Review Letters* **109**, 037603 (2012). doi:10.1103/PhysRevLett.109.037603.
- [57] J.-S. Kim *et al.* Current-induced vortex dynamics and pinning potentials probed by homodyne detection. *Physical Review B* **82**, 104427 (2010). doi:10.1103/PhysRevB.82.104427.
- [58] B. Van Waeyenberge *et al.* Magnetic vortex core reversal by excitation with short bursts of an alternating field. *Nature* **444**, 461 (2006). doi:10.1038/nature05240.
- [59] H. Kronmüller, and S. Parkin (eds.) *Handbook of Magnetism and Advanced Magnetic Materials*, vol. 3: Novel techniques for characterizing and preparing samples (Wiley, 2007).
- [60] H. Hopster, and H. P. Oepen (eds.) *Magnetic Microscopy of Nanostructures* (Springer, Berlin, Heidelberg, New York, 2005).
- [61] Y. Acremann *et al.* Imaging precessional motion of the magnetization vector. *Science* **290**, 492 (2000). doi:10.1126/science.290.5491.492.
- [62] D. Chumakov *et al.* Nanosecond time-scale switching of permalloy thin film elements studied by wide-field time-resolved Kerr microscopy. *Physical Review B* **71**, 014410 (2005). doi:10.1103/PhysRevB.71.014410.

- [63] S. Heinze *et al.* Real-space imaging of two-dimensional antiferromagnetism on the atomic scale. *Science* **288**, 1805 (2000). doi:10.1126/science.288.5472.1805.
- [64] A. Schwarz, and R. Wiesendanger. Magnetic sensitive force microscopy. *Nano Today* **3**, 28 (2008). doi:10.1016/S1748-0132(08)70013-6.
- [65] J. N. Chapman. The investigation of magnetic domain structures in thin foils by electron microscopy. *Journal of Physics D: Applied Physics* **17**, 623 (1984). doi:10.1088/0022-3727/17/4/003.
- [66] A. Krasnyuk *et al.* Time-resolved photoemission electron microscopy of magnetic field and magnetisation changes. *Applied Physics A* **76**, 863 (2003). doi:10.1007/s00339-002-1965-8.
- [67] S. A. Nepijko, A. Graff, G. Schönhense, and C. M. Schneider. Quantitative determination of magnetic fields from iron particles of oblong form encapsulated by carbon nanotubes using electron holography. *Applied Physics A* **94**, 543 (2009). doi:10.1007/s00339-008-4947-7.
- [68] S. A. Nepijko, and G. Schönhense. Electron holography for electric and magnetic field measurements and its application for nanophysics. In *Advances in Imaging and Electron Physics* **169**, 173 (Elsevier, 2011). <http://linkinghub.elsevier.com/retrieve/pii/B9780123859815000057>.
- [69] G. Schütz *et al.* Absorption of circularly polarized x rays in iron. *Physical Review Letters* **58**, 737 (1987). doi:10.1103/PhysRevLett.58.737.
- [70] P. Fischer *et al.* Magnetic imaging with full-field soft x-ray microscopies. *Journal of Electron Spectroscopy and Related Phenomena* (2013). doi:10.1016/j.elspec.2013.03.012.
- [71] A. L. D. Kilcoyne *et al.* Interferometer-controlled scanning transmission x-ray microscopes at the advanced light source. *Journal of Synchrotron Radiation* **10**, 125 (2003). doi:10.1107/S0909049502017739.
- [72] J. Rhensius *et al.* Control of spin configuration in half-metallic  $\text{La}_{0.7}\text{Sr}_{0.3}\text{MnO}_3$  nano-structures. *Applied Physics Letters* **99**, 062508 (2011). doi:10.1063/1.3623480.
- [73] D. Nolle, M. Weigand, G. Schütz, and E. Goering. High contrast magnetic and nonmagnetic sample current microscopy for bulk and transparent samples using soft x-rays. *Microscopy and Microanalysis* **17**, 834 (2011). doi:10.1017/S1431927611000560.

- 
- [74] C. A. F. Vaz, C. Moutafis, C. Quitmann, and J. Raabe. Luminescence-based magnetic imaging with scanning x-ray transmission microscopy. *Applied Physics Letters* **101**, 083114 (2012). doi:10.1063/1.4747697.
- [75] C. Vaz, C. Moutafis, M. Buzzi, and J. Raabe. X-ray excited optical luminescence of metal oxide single crystals. *Journal of Electron Spectroscopy and Related Phenomena* (2013). doi:10.1016/j.elspec.2012.12.012.
- [76] H. Stoll *et al.* High-resolution imaging of fast magnetization dynamics in magnetic nanostructures. *Applied Physics Letters* **84**, 3328 (2004). doi:10.1063/1.1723698.
- [77] Y. Acremann *et al.* Time-resolved imaging of spin transfer switching: Beyond the macrospin concept. *Physical Review Letters* **96**, 217202 (2006). doi:10.1103/PhysRevLett.96.217202.
- [78] S. Eisebitt *et al.* Lensless imaging of magnetic nanostructures by x-ray spectro-holography. *Nature* **432**, 885 (2004). doi:10.1038/nature03139.
- [79] T. Wang *et al.* Femtosecond single-shot imaging of nanoscale ferromagnetic order in Co/Pd multilayers using resonant x-ray holography. *Physical Review Letters* **108**, 267403 (2012). doi:10.1103/PhysRevLett.108.267403.
- [80] C. M. Günther *et al.* Sequential femtosecond x-ray imaging. *Nature Photonics* **5**, 99 (2011). doi:10.1038/nphoton.2010.287.
- [81] E. Guehrs *et al.* Wavefield back-propagation in high-resolution x-ray holography with a movable field of view. *Optics Express* **18**, 18922 (2010). doi:10.1364/OE.18.018922.
- [82] J. Geilhufe *et al.* Imaging 3 dimensional structures by Fourier transform holography. (*in preparation*)
- [83] E. Guehrs, C. M. Günther, R. Könnecke, B. Pfau, and S. Eisebitt. Holographic soft x-ray omni-microscopy of biological specimens. *Optics Express* **17**, 6710 (2009). doi:10.1364/OE.17.006710.
- [84] F. Büttner *et al.* Topological mass of skyrmionic spin structures. (*submitted*)
- [85] T. Hauet *et al.* Direct observation of field and temperature induced domain replication in dipolar coupled perpendicular anisotropy films. *Physical Review B* **77**, 184421 (2008). doi:10.1103/PhysRevB.77.184421.
- [86] D. Stickler *et al.* Soft x-ray holographic microscopy. *Applied Physics Letters* **96**, 042501 (2010). doi:10.1063/1.3291942.

- 
- [87] W. F. Schlotter *et al.* Extended field of view soft x-ray Fourier transform holography: toward imaging ultrafast evolution in a single shot. *Optics letters* **32**, 3110 (2007).
- [88] B. Pfau *et al.* Femtosecond pulse x-ray imaging with a large field of view. *New Journal of Physics* **12**, 095006 (2010). doi:10.1088/1367-2630/12/9/095006.
- [89] B. Pfau *et al.* Origin of magnetic switching field distribution in bit patterned media based on pre-patterned substrates. *Applied Physics Letters* **99**, 062502 (2011). doi:10.1063/1.3623488.
- [90] C. M. Günther *et al.* Microscopic reversal behavior of magnetically capped nanospheres. *Physical Review B* **81**, 064411 (2010). doi:10.1103/PhysRevB.81.064411.
- [91] Silson Ltd.. <http://www.silson.com/>.
- [92] K. Suzuki, J. Matsui, and T. Torikai. SiN membrane masks for x-ray lithography. *Journal of Vacuum Science and Technology* **20**, 191 (1982). doi:10.1116/1.571355.
- [93] Showa Denko K. K.. <http://www.sdk.co.jp/>.
- [94] S. Yasin, D. Hasko, and H. Ahmed. Comparison of MIBK/IPA and water/IPA as PMMA developers for electron beam nanolithography. *Micro-electronic Engineering* **61**, 745 (2002). doi:10.1016/S0167-9317(02)00468-9.
- [95] F. Büttner *et al.* Magnetic states in low-pinning high-anisotropy material nanostructures suitable for dynamic imaging. *Physical Review B* **87**, 134422 (2013). doi:10.1103/PhysRevB.87.134422.
- [96] D. Dai *et al.* Equivalent circuit model of a Ge/Si avalanche photodiode. In *Group IV Photonics, 2009. GFP'09. 6th IEEE International Conference on*, 13 (2009). [http://ieeexplore.ieee.org/xpls/abs\\_all.jsp?arnumber=5338304](http://ieeexplore.ieee.org/xpls/abs_all.jsp?arnumber=5338304).
- [97] Y. Zhang *et al.* Perpendicular-magnetic-anisotropy CoFeB racetrack memory. *Journal of Applied Physics* **111**, 093925 (2012). doi:10.1063/1.4716460.
- [98] S. Breitreutz *et al.* Controlled reversal of Co/Pt dots for nanomagnetic logic applications. *Journal of Applied Physics* **111**, 07A715 (2012). doi:10.1063/1.3675171.
- [99] J. Heinen *et al.* Determination of the spin torque non-adiabaticity in perpendicularly magnetized nanowires. *Journal of Physics: Condensed Matter* **24**, 024220 (2012). doi:10.1088/0953-8984/24/2/024220.

- 
- [100] J. Xiao, A. Zangwill, and M. D. Stiles. Spin-transfer torque for continuously variable magnetization. *Physical Review B* **73**, 054428 (2006). doi:10.1103/PhysRevB.73.054428.
- [101] C. Moutafis, S. Komineas, C. A. F. Vaz, J. A. C. Bland, and P. Eames. Vortices in ferromagnetic elements with perpendicular anisotropy. *Physical Review B* **74**, 214406 (2006). doi:10.1103/PhysRevB.74.214406.
- [102] K. Tanabe *et al.* Spin-motive force due to a gyrating magnetic vortex. *Nature Communications* **3**, 845 (2012). doi:10.1038/ncomms1824.
- [103] M. Kammerer *et al.* Magnetic vortex core reversal by excitation of spin waves. *Nature Communications* **2**, 279 (2011). doi:10.1038/ncomms1277.
- [104] A. Bisig *et al.* Direct imaging of current induced magnetic vortex gyration in an asymmetric potential well. *Applied Physics Letters* **96**, 152506 (2010). doi:10.1063/1.3373590.
- [105] L. Heyne *et al.* Relationship between nonadiabaticity and damping in permalloy studied by current induced spin structure transformations. *Physical Review Letters* **100**, 066603 (2008). doi:10.1103/PhysRevLett.100.066603.
- [106] T. Thomson, G. Hu, and B. D. Terris. Intrinsic distribution of magnetic anisotropy in thin films probed by patterned nanostructures. *Physical Review Letters* **96**, 257204 (2006). doi:10.1103/PhysRevLett.96.257204.
- [107] J. Vogel *et al.* Direct observation of massless domain wall dynamics in nanostripes with perpendicular magnetic anisotropy. *Physical Review Letters* **108**, 247202 (2012). doi:10.1103/PhysRevLett.108.247202.
- [108] A. J. Schellekens, A. v. d. Brink, J. H. Franken, H. J. M. Swagten, and B. Koopmans. Electric-field control of domain wall motion in perpendicularly magnetized materials. *Nature Communications* **3**, 847 (2012). doi:10.1038/ncomms1848.
- [109] M. S. Pierce *et al.* Quasistatic x-ray speckle metrology of microscopic magnetic return-point memory. *Physical Review Letters* **90**, 175502 (2003). doi:10.1103/PhysRevLett.90.175502.
- [110] G. Malinowski *et al.* Control of speed and efficiency of ultrafast demagnetization by direct transfer of spin angular momentum. *Nature Physics* **4**, 855 (2008). doi:10.1038/nphys1092.
- [111] J. Heinen *et al.* Current-induced domain wall motion in Co/Pt nanowires: Separating spin torque and oersted-field effects. *Applied Physics Letters* **96**, 202510 (2010). doi:10.1063/1.3405712.

- 
- [112] C. M. Günther *et al.* Steplike versus continuous domain propagation in Co/Pd multilayer films. *Applied Physics Letters* **93**, 072505 (2008). doi:10.1063/1.2968305.
- [113] J. E. Davies *et al.* Magnetization reversal of Co/Pt multilayers: Microscopic origin of high-field magnetic irreversibility. *Physical Review B* **70**, 224434 (2004). doi:10.1103/PhysRevB.70.224434.
- [114] D. G. Stinson, and S.-C. Shin. Magnetization and anisotropy of Co/Pd multilayer thin films. *Journal of Applied Physics* **67**, 4459 (1990). doi:10.1063/1.344904.
- [115] Z. Liu *et al.* Thickness dependent magnetization dynamics of perpendicular anisotropy Co/Pd multilayer films. *Journal of Magnetism and Magnetic Materials* **323**, 1623 (2011). doi:10.1016/j.jmmm.2011.01.025.
- [116] D. Smith *et al.* Magnetization reversal and magnetic anisotropy in patterned Co/Pd multilayer thin films. *Journal of Applied Physics* **103**, 023920 (2008). doi:10.1063/1.2837049.
- [117] M. S. Pierce *et al.* Disorder-induced magnetic memory: Experiments and theories. *Physical Review B* **75**, 144406 (2007). doi:10.1103/PhysRevB.75.144406.
- [118] R. Lavrijsen *et al.* Reduced domain wall pinning in ultrathin Pt/Co<sub>100-x</sub>B<sub>x</sub>/Pt with perpendicular magnetic anisotropy. *Applied Physics Letters* **96**, 022501 (2010). doi:10.1063/1.3280373.
- [119] W. F. Schlotter. *Lensless Fourier Transform Holography with Soft X-Rays*. Dissertation, Stanford University (2007). <http://www.stanford.edu/%7Ewschlott/thesis/SchlottterDissertationFinal.pdf>.
- [120] F. Büttner *et al.* Thickness dependence of the magnetic properties of ripple-patterned Fe/MgO(001) films. *Physical Review B* **84**, 064427 (2011). doi:10.1103/PhysRevB.84.064427.
- [121] O. Hellwig, G. P. Denbeaux, J. B. Kortright, and E. E. Fullerton. X-ray studies of aligned magnetic stripe domains in perpendicular multilayers. *Physica B: Condensed Matter* **336**, 136 (2003). doi:10.1016/S0921-4526(03)00282-5.
- [122] C. A. F. Vaz, J. A. C. Bland, and G. Lauhoff. Magnetism in ultrathin film structures. *Reports on Progress in Physics* **71**, 056501 (2008). doi:10.1088/0034-4885/71/5/056501.
- [123] C. Moutafis *et al.* Skyrmions in perpendicular magnetic anisotropy dots: Imaging and simulations. In *2011 International Conference on Electromagnetics in Advanced Applications (ICEAA)*, 1121 (IEEE, 2011).



- 
- [124] S. T. Chui and V. N. Ryzhov. Soliton and 2D domains in ultrathin magnetic films. *Physical Review Letters* **78**, 2224 (1997). doi:10.1103/PhysRevLett.78.2224.
- [125] P. Milde *et al.* Unwinding of a skyrmion lattice by magnetic monopoles. *Science* **340**, 1076 (2013). doi:10.1126/science.1234657.
- [126] A. Fert, V. Cros, and J. Sampaio. Skyrmions on the track. *Nature Nanotechnology* **8**, 152 (2013). doi:10.1038/nnano.2013.29.
- [127] J. Zang, M. Mostovoy, J. H. Han, and N. Nagaosa. Dynamics of skyrmion crystals in metallic thin films. *Physical Review Letters* **107**, 136804 (2011). doi:10.1103/PhysRevLett.107.136804.
- [128] S.-Z. Lin, C. Reichhardt, C. D. Batista, and A. Saxena. Particle model for skyrmions in chiral magnets: dynamics, pinning and creep. *arXiv:1302.6205* (2013).
- [129] R. W. Shaw, J. W. Moody, and R. M. Sandfort. Dynamic properties of high-mobility garnet films in the presence of in-plane magnetic fields. *Journal of Applied Physics* **45**, 2672 (1974). doi:10.1063/1.1663649.
- [130] N. S. Kiselev, A. N. Bogdanov, R. Schäfer, and U. K. Rößler. Comment on “Giant skyrmions stabilized by dipole-dipole interactions in thin ferromagnetic films”. *Physical Review Letters* **107**, 179701 (2011). doi:10.1103/PhysRevLett.107.179701.
- [131] X. Yu *et al.* Magnetic stripes and skyrmions with helicity reversals. *Proceedings of the National Academy of Sciences* **109**, 8856 (2012). doi:10.1073/pnas.1118496109.
- [132] K. Holldack. Private communication.
- [133] MicroMagnum. <http://micromagnum.informatik.uni-hamburg.de/>.
- [134] O. Bostanjoglo, and T. Rosin. Resonance oscillations of magnetic domain walls and bloch lines observed by stroboscopic electron microscopy. *physica status solidi (a)* **57**, 561 (1980). doi:10.1002/pssa.2210570212.
- [135] S. M. Mohseni *et al.* Spin Torque-Generated magnetic droplet solitons. *Science* **339**, 1295 (2013). doi:10.1126/science.1230155.
- [136] K. Kuepper, M. Buess, J. Raabe, C. Quitmann, and J. Fassbender. Dynamic vortex-antivortex interaction in a single cross-tie wall. *Physical Review Letters* **99**, 167202 (2007). doi:10.1103/PhysRevLett.99.167202.
- [137] N. Vernier *et al.* Modified current induced domain wall motion in GaMnAs nanowire. *arXiv:1303.6174v1* (2013).

- [138] H. Jung *et al.* Tunable negligible-loss energy transfer between dipolar-coupled magnetic disks by stimulated vortex gyration. *Scientific Reports* **1** 59 (2011). doi:10.1038/srep00059.
- [139] L. Thomas *et al.* Resonant amplification of magnetic domain-wall motion by a train of current pulses. *Science* **315**, 1553 (2007). doi:10.1126/science.1137662.
- [140] S. Heinze *et al.* Spontaneous atomic-scale magnetic skyrmion lattice in two dimensions. *Nature Physics* **7**, 713 (2011). doi:10.1038/nphys2045.
- [141] N. Romming *et al.* Writing and deleting single magnetic skyrmions. *Science* **341**, 636 (2013). doi:10.1126/science.1240573.
- [142] F. Jonietz *et al.* Spin transfer torques in MnSi at ultralow current densities. *Science* **330**, 1648 (2010). doi:10.1126/science.1195709.

# Acknowledgments

---

The results presented in this thesis have been achieved through the collaborative work of a large team. More than 30 people from 10 institutions have made these achievements possible. I am most grateful for this enormous support.

My foremost thanks go to my supervisors Prof. Mathias Kläui and Prof. Stefan Eisebitt for offering me the unique opportunity of pursuing my PhD in two groups with outstanding access to know-how, equipment, and facilities. Moreover, I was given the chance to complete my tasks at external institutions, such as at the Laboratory for Micro- and Nanotechnology (LMN) at the Paul Scherrer Institut in Switzerland or at the Nanostructuring Center in Kaiserslautern and I am indebted for such opportunities. Finally, I would like to acknowledge their constant availability for discussions and help, and the numerous opportunities given to me to present my results to the international community and the training and the feedback for these presentations.

As stated above, this project was made possible by the help of numerous people. In particular, I would like to thank Christoforos Moutafis for scientific discussions throughout the project, support on all beamtimes, and feedback for written and oral presentations. I would like to thank André Bisig for continuous and altruistic support, in particular with the high frequency electronics, and for scientific discussions. I am deeply indebted to Carlos Vaz for teaching me how to write texts in scientific English, and for proof-reading all my publications, including this dissertation, with incredible speed and precision. I would like to thank Jan Geilhufe and Michael Schneider for continuous support for this project which went well beyond the participation at beamtimes and for their motivation even at night and at weekends. Without such selfless support, this project would not have been such a success.

I would like to thank Benjamin Krüger for help with fitting the data, for performing the micromagnetic simulations, and for good teamwork when deriving the analytical model for the Döring mass density.

The results of this thesis were mostly obtained during beamtimes, each at least two weeks of continuous operation. Such experiments cannot be realized without a large number of people motivated to spend their evenings, nights, and weekends at a synchrotron. In addition to the people mentioned before, I would like to thank Christian M. Günther, Clemens von Korff Schmising, Jyoti Mohanty, Bastian Pfau,

Stefan Schaffert, Michael Foerster, Tomek Schulz, Simone Finizio, and Roberto Lo Conte for such support and for scientific discussions during the experiments.

Furthermore, I would like to thank Michael Schneider, Christian M. Günther, Carlos Vaz, Jeroen Franken, Reinoud Lavrijsen, and Bert Läger for helping to fabricate more than 200 samples plus 250 holographic substrates required to obtain the one sample that has proven suitable for the observation of the gyration of a magnetic bubble. In addition, I would like to thank Jan Rhensius, Vitaliy Guzenko, Anja Weber, Eugen Deckart, Arnold Lücke for training with the nano-fabrication tools facilities and Laura J. Heyderman and Jens Gobrecht for granting me access to the clean room of the LMN.

Finally, I would like to thank my family and Gesine for love, mental support, and for taking care of my duties at home when I was busy.

# Curriculum Vitae

---

## Personal details

Name:	Felix Büttner
Address:	Hermann-Weyl-Stieg 49, 37077 Göttingen
Date and place of birth:	07.04.1986 in Göttingen
Citizenship:	German
Marital status:	unmarried, no children

## Education and Research

### Ph.D. in Physics

Topic:	“Dynamic imaging of magnetic bubbles using x-ray holography”
07/2011 - 11/2013	Research in a joint project between the University of Mainz and the TU Berlin
08/2011 - 07/2012	Research at the Paul Scherrer Institut (Switzerland)
11/2011	Acceptance to the MAINZ Graduate School
07/2011	Relocation to the University of Mainz along with the first supervisor
06/2010 - 06/2011	Research in a joint project between the École Polytechnique Fédérale de Lausanne and the TU Berlin
06/2010	Acceptance to the EPFL Doctoral School

### Diplom in Physics

10/2005 - 02/2010	University of Göttingen (Germany) Diplom thesis: “Schichtdickenabhängigkeit der magnetischen Eigenschaften von strukturierten einkristallinen Eisenfilmen”
08/2007 - 02/2008	Erasmus fellowship, University of Jyväskylä (Finland)
10/2003 - 03/2006	TU Kaiserslautern: courses during school time

### School

06/2005	Abitur, Felix-Klein-Gymnasium Göttingen
---------	---

## Teaching

- 10/2012 - 07/2013 Supervisor for advanced lab courses for physicists
- 03/2010 Lecturer: review course of thermodynamics and statistical mechanics
- 04/2009 - 09/2009 Supervisor for lab courses: physics for beginners
- 04/2007 - 09/2007 Supervisor for lab courses: physics for beginners and for theoretical exercises: quantum mechanics
- 10/2006 - 03/2007 Supervisor for theoretical exercises: mathematics for physicists

## Awards

- 01/2013 Best Poster Award at the Joint MMM / Intermag conference, Chicago (IL, USA)
- 05/2012 Best Poster Award at the Intermag conference, Vancouver (BC, Canada)

# List of publications

---

1. A. Tkach, M. Fries, M. B. Yazdi, M. Foerster, **F. Büttner**, and M. Kläui. Magnetoelectric engineering of epitaxial  $\text{Fe}_3\text{O}_4$  thin film properties on (110) PMN-PT piezosubstrates. (*in preparation*)
2. **F. Büttner**, C. Moutafis, M. Schneider, B. Krüger, C. M. Günther, J. Geilhufe, C. v. Korff Schmising, J. Mohanty, B. Pfau, S. Schaffert, A. Bisig, M. Foerster, T. Schulz, C. A. F. Vaz, J. H. Franken, H. J. M. Swagten, M. Kläui, and S. Eisebitt. Topological mass of skyrmionic spin structures. (*submitted*)
3. J.-S. Kim, M.-A. Mawass, A. Bisig, B. Krüger, R. Reeve, T. Schulz, **F. Büttner**, M. Weigand, H. Stoll, J. Yoon, C.-Y. You, S. Eisebitt, H. J. M. Swagten, B. Koopmans, and M. Kläui. Synchronous precessional motion of multiple domain walls in a ferromagnetic nanowire by perpendicular field pulses. (*submitted*)
4. **F. Büttner**, M. Schneider, C. M. Günther, C. A. F. Vaz, B. Lägél, D. Berger, S. Selve, M. Kläui, and S. Eisebitt. Automatable sample fabrication process for pump-probe x-ray holographic imaging. *Optics Express* (*accepted*)
5. J. Geilhufe, B. Pfau, M. Schneider, C. M. Günther, S. Werner, S. Schaffert, E. Guehrs, **F. Büttner**, S. Frömmel, M. Kläui, and S. Eisebitt. Monolithic Focussed Reference Beam X-ray Holography *Nature Communications* (*accepted*)
6. L. Müller, S. Schleitzer, C. Gutt, B. Pfau, S. Schaffert, J. Geilhufe, C. v. Korff Schmising, M. Schneider, C. M. Günther, **F. Büttner**, F. Capotondi, E. Pedersoli, S. Düsterer, H. Redlin, A. Al-Shemmary, R. Treusch, J. Bach, R. Frömter, B. Vodungbo, J. Gautier, P. Zeitoun, H. Popescu, V. Lopez-Flores, N. Beaulieu, F. Sirotti, N. Jaouen, G. Malinowski, B. Tudu, K. Li, J. Lüning, H. P. Oepen, M. Kiskinova, S. Eisebitt, and G. Grübel, Ultrafast Dynamics of Magnetic Domain Structures Probed by Coherent Free-Electron Laser Light. *Synchrotron Radiation News* **26**, 27 (2013).
7. A. Bisig, M. Stärk, M.-A. Mawass, C. Moutafis, J. Rhensius, J. Heidler, **F. Büttner**, M. Noske, M. Weigand, S. Eisebitt, T. Tyliczszak, B. v. Waeyen-

- berge, H. Stoll, G. Schütz, and M. Kläui. Correlated velocity and domain wall spin structure oscillations. *Nature Communications* **4**, 2328 (2013).
8. L. Müller, C. Gutt, B. Pfau, S. Schaffert, J. Geilhufe, **F. Büttner**, J. Mohanty, S. Flewett, R. Treusch, S. Düsterer, H. Redlin, A. Al-Shemmary, M. Hille, A. Kobs, R. Frömter, H. P. Oepen, B. Ziaja, N. Medvedev, S.-K. Son, R. Thiele, R. Santra, B. Vodungbo, J. Lüning, S. Eisebitt, and G. Grübel. Breakdown of the X-Ray Resonant Magnetic Scattering Signal during Intense Pulses of Extreme Ultraviolet Free-Electron-Laser Radiation. *Physical Review Letters* **110**, 234801 (2013).
9. **F. Büttner**, C. Moutafis, A. Bisig, P. Wohlhüter, C. M. Günther, J. Mohanty, J. Geilhufe, M. Schneider, C. v. Korff Schmising, S. Schaffert, B. Pfau, M. Hantschmann, M. Riemeier, M. Emmel, S. Finizio, G. Jakob, M. Weigand, J. Rhensius, J. H. Franken, R. Lavrijsen, H. J. M. Swagten, H. Stoll, S. Eisebitt, and M. Kläui. Magnetic states in low-pinning high-anisotropy material nanostructures suitable for dynamic imaging. *Physical Review B* **87**, 134422 (2013).
10. L. Müller, C. Gutt, S. Streit-Nierobisch, M. Walther, S. Schaffert, B. Pfau, J. Geilhufe, **F. Büttner**, S. Flewett, C. M. Günther, S. Eisebitt, A. Kobs, M. Hille, D. Stickler, R. Frömter, H. P. Oepen, J. Lüning, and G. Grübel. Endstation for ultrafast magnetic scattering experiments at the free-electron laser in Hamburg. *Review of Scientific Instruments* **84**, 013906 (2013).
11. S. Flewett, C. M. Günther, C. v. Korff Schmising, B. Pfau, J. Mohanty, **F. Büttner**, M. Riemeier, M. Hantschmann, M. Kläui, and S. Eisebitt. Holographically aided iterative phase retrieval. *Optics Express* **20**, 29210 (2012).
12. B. Pfau, S. Schaffert, L. Müller, C. Gutt, A. Al-Shemmary, **F. Büttner**, R. Delaunay, S. Düsterer, S. Flewett, R. Frömter, J. Geilhufe, E. Guehrs, C. M. Günther, R. Hawaldar, M. Hille, N. Jaouen, A. Kobs, K. Li, J. Mohanty, H. Redlin, W. F. Schlotter, D. Stickler, R. Treusch, B. Vodungbo, M. Kläui, H. P. Oepen, J. Lüning, G. Grübel, and S. Eisebitt. Ultrafast optical demagnetization manipulates nanoscale spin structure in domain walls. *Nature Communications* **3**, 1100 (2012).
13. C. Moutafis, J. Rhensius, A. Bisig, **F. Büttner**, C. Barton, C. Morrison, T. Thomson, C. Tieg, S. Schaffert, B. Pfau, C. M. Günther, S. Eisebitt, and M. Kläui. Skyrmions in perpendicular magnetic anisotropy dots: Imaging and simulations. *2011 International Conference on Electromagnetics in Advanced Applications (ICEAA)* 1121 (2011).



- 
14. **F. Büttner**, K. Zhang, S. Seyffarth, T. Liese, H.-U. Krebs, C. A. F. Vaz, and H. Hofsäss. Thickness dependence of the magnetic properties of ripple-patterned *Physical Review B* **84**, 064427 (2011).